

2025

Advanced quantum structures for infrared detectors

<https://hdl.handle.net/2144/49769>

Downloaded from DSpace Repository, DSpace Institution's institutional repository

BOSTON UNIVERSITY
COLLEGE OF ENGINEERING

Dissertation

**ADVANCED QUANTUM STRUCTURES FOR INFRARED
DETECTORS**

by

JOHN GLENNON

B.S., Northeastern University, 2017

Submitted in partial fulfillment of the
requirements for the degree of
Doctor of Philosophy

2025

© 2025 by
JOHN GLENNON
All rights reserved

Portions of this dissertation are adapted from previously published journal articles and conference proceedings. Permission to reuse these works was obtained according to the publishers' policies.

- Chapter 5: Glennon, J., Bertazzi, F., Tibaldi, A., & Bellotti, E. Extraction of Mobility from Quantum Transport Calculations of Type-II Superlattices. *Physical Review Applied*, 19(4), 044045. (17 April 2023). <http://dx.doi.org/10.1103/PhysRevApplied.19.044045>

- Chapter 6 (results for InAs/GaSb superlattice): Glennon, J., & Bellotti, E. Quantum transport simulation of a mid-wave infrared Ga-based type-II superlattice for curved focal-plane arrays. Proc. SPIE 12687. *Infrared Sensors, Devices, and Applications XIII*. 126870F (10 October 2023). <http://dx.doi.org/10.1117/12.2682192>

Approved by

First Reader

Enrico Bellotti, PhD
Professor of Electrical and Computer Engineering
Professor of Materials Science and Engineering

Second Reader

Roberto Paiella, PhD
Professor of Electrical and Computer Engineering
Professor of Materials Science and Engineering

Third Reader

Sahar Sharifzadeh, PhD
Associate Professor of Electrical and Computer Engineering
Associate Professor of Materials Science and Engineering
Associate Professor of Chemistry

Fourth Reader

Francesco Bertazzi, PhD
Professor of Electronics and Telecommunications
Politecnico di Torino

ACKNOWLEDGMENTS

This dissertation is the culmination of five years of hard work during a period of significant change in my life. This PhD was marked by a global pandemic, my engagement to my wonderful fiancé, and ultimately our purchase of a home together. The support I received from the people in my life during this time cannot be overstated and could fill the pages of this dissertation. While a poor substitute, I will do my best to give credit where it is due here.

I would still be lost in quantum transport and device physics theory if it were not for the intellectual support of several individuals. Dr. Alexandros Kyrtos was my first mentor in the Computational Electronics Lab and helped prepare me to be a contributor. Dr. Philip Klipstein provided significant guidance on the physics of type-II superlattices. Dr. Binh-Minh Nguyen and Dr. Mark O'Masta provided many helpful discussions related to Ga-free type-II superlattices and curved focal-plane arrays. Prof. Francesco Bertazzi and Prof. Alberto Tibaldi of Politecnico di Torino developed the code used in this work and were invaluable resources to me in building expertise using it. Additionally, I would like to acknowledge my committee members and thank them for their guidance during the completion of this dissertation: Professors Roberto Paiella and Sahar Sharifzadeh of Boston University and Professor Francesco Bertazzi of Politecnico di Torino. I must extend a special thank you to my PI Professor Enrico Bellotti. I appreciate that he believed in me enough, a Mechanical Engineering undergrad, to entrust me with a project related to quantum transport because it was most interesting to me. I would not have been able to complete my investigations without his guidance and support. Lastly, I had numerous fruitful conversations with the other students in the Computational Electronics Lab, with special thanks to Dr. Masahiko Matsubara, Dr. Mike Zhu, and Dr. Matteo Alasio.

In addition to intellectual support, I have received great emotional support from the

people most important to me. For starters, my friends from my undergraduate institution, Northeastern University, have been a mainstay in my life. I feel so fortunate to have such a large group of friends who have stayed living in the Boston area. My sister and brother-in-law Leah and Ricky Long have served as a much-needed sanity check in times of uncertainty. My parents, William and Mary Ellen Glennon, have supported my intellectual pursuits from the very beginning, including editing my essays for grade school and suffering through documentaries on theoretical physics on TV. It was of critical importance to them that my sister and I pursue a career in which we can be passionate. My dad often “joked” that his career in public accounting had been a huge mistake. I may have failed long before this PhD program without their intellectual, emotional, and financial support. My fiancé has been my steadfast partner throughout this whole PhD. She was an emotional ballast to me during my lowest points and the first to celebrate my achievements. If it were not for her exceptional performance in her career at Mass General Brigham, we would not have been able to live in Boston on my PhD stipend. I owe an incredible debt to her that I will spend the rest of my life repaying.

The work on the extraction of mobility from NEGF calculations for type-II superlattices as well as the work on Ga-free curved focal-plane arrays was supported by the Defense Advanced Research Projects Agency program Focal Arrays for Curved Infrared Imagers, initially managed by Dr. Whitney Mason and later by Trish Veeder. The work on Ga-based curved focal-plane arrays as well as the work on finding optimized Ga-free type-II superlattice structures on various substrate lattice constants was supported by the U.S. Army Research Laboratorys Center for Semiconductor Modeling. Finally, the computational resources were provided by the Department of Defense High Performance Computing Systems, the 2019 Army Research Office Defense University Research Instrumentation Program Award, and the DoD HPC Modernization program.

ADVANCED QUANTUM STRUCTURES FOR INFRARED DETECTORS

JOHN GLENNON

Boston University, College of Engineering, 2025

Major Professor: Enrico Bellotti, PhD

Professor of Electrical and Computer Engineering
Professor of Materials Science and Engineering

ABSTRACT

Type-II superlattices (T2SLs) have emerged as promising alternatives to the more established bulk material systems for infrared (IR) photodetection. This is due to predicted fundamental advantages, such as the tunability of the band gap and theoretically reduced Auger recombination rates. However, the superiority of these materials has not been experimentally realized, prompting the need for further investigation. A bottleneck in the development of improved superlattice (SL) structures and devices is the cost in time and resources required to prototype and characterize these materials as well as incomplete knowledge of the material properties and physical phenomena that characterize these structures. Therefore, the field would greatly benefit from simulation methodologies that enable the development of advanced T2SL materials. In this work, the field of IR photodetection is reviewed highlighting the most common T2SLs structures currently being experimentally implemented. A quantum transport model that includes the necessary physical mechanisms to model carrier transport in these structures will be presented. The results of an investigation on the extraction of vertical carrier mobility, a property important for carrier collection, from quantum transport simulations is presented for an example T2SL. It is demonstrated that carrier transport in these structures can be highly coherent. In this case, the apparent mo-

bility is suppressed due to ballistic resistance, requiring care when predicting the intrinsic mobility of these materials. The best method of mobility extraction is one that considers the dependence of the resistance on device length. This method was applied to predict the quantum efficiency (QE) in curved focal-plane arrays composed of n-type mid-wave InAs/InAsSb and InAs/GaSb structures subjected to the effects of superlattice disorder and external strain imposed by the curving procedure. It is demonstrated that the external strain has a minimal impact on the QE relative to disorder in both structures suggesting the device design could be viable. Additionally, it was found that large magnitudes of positive axisymmetric strain could result in enhanced hole transport. Finally, a comprehensive investigation is presented that probed for optimized n-type long-wave InAsSb/InAsSb SL structures, a material known to result in low QE devices, for various substrate lattice constants. Several structures were found demonstrating hole mobilities with greater resilience to SL disorder providing potential candidates for future prototyping.

CONTENTS

Acknowledgements	iv
Abstract	vi
List of Tables	xii
List of Figures	xiii
List of Symbols and Abbreviations	xxv
1 Introduction	1
1.1 Motivation	1
1.2 Outline	3
2 Infrared Photodetection	5
2.1 Bulk HgCdTe	6
2.2 Quantum Well Infrared Photodetectors	7
2.3 Type-II Superlattices	8
2.3.1 Type-II Superlattice Structures	9
2.3.2 Type-II Superlattice Material Properties	15
2.3.3 Quantum Efficiency of T2SL IR Devices	21
3 Non-equilibrium Green's Functions Formalism	23
3.1 Introduction	23
3.2 Band Structure Model	24
3.2.1 Effective Mass Approximation	27

3.2.2	Four-band $\mathbf{k} \cdot \mathbf{p}$ Hamiltonian	28
3.3	Non-equilibrium Green's Functions	31
3.4	Equations of Motion of the Green's Functions	35
3.5	Numerical Implementation of Non-equilibrium Green's Functions	41
3.5.1	Spatial Discretization of Dyson and Keldysh Equations	41
3.5.2	Implementation of Open Boundary Conditions	43
3.5.3	Mode-Space Methodology	45
3.6	Particle Interaction Self-Energies	47
3.6.1	Acoustic Phonons	48
3.6.2	Polar-Optical Phonons	49
3.7	Material Property Extraction	51
4	Device Physics of Infrared Photodetectors	53
4.1	Photodetector Dark Current	53
4.1.1	Generation Recombination Current	54
4.1.2	Diffusion Current	56
4.1.3	Tunneling Current	57
4.1.4	Surface Leakage Current	59
4.2	Quantum Efficiency	59
4.2.1	pin Detectors	60
4.2.2	nBn Detectors	62
5	Mobility Extraction from Quantum Transport Calculations	64
5.1	Introduction	64
5.2	Mesoscopic Picture of Mobility	65

5.3	InAs/GaSb Example Structure	68
5.4	Analysis of Mobility Extraction Methodologies	70
5.4.1	Average Velocity Method	70
5.4.2	Ballistic Approximation Method	79
5.4.3	Resistance Scaling Method	86
5.5	Mobility Methods Results Comparison	94
5.6	Conclusion	96
6	Effect of Disorder and Strain on the Vertical Hole Mobility in MWIR T2SL-based Curved Focal Plane Arrays	98
6.1	Introduction	98
6.2	Superlattice Structures	99
6.2.1	InAs/InAsSb Structure	99
6.2.2	InAs/GaSb Structure	104
6.3	FPA Device Geometry	106
6.4	Material Effects on Hole Mobility	109
6.4.1	Effect of Disorder	110
6.4.2	Effect of Strain	112
6.5	QE in Curved Focal Plane Array	117
6.6	Conclusion	126
7	Type-II Superlattice Optimization for Enhanced Hole Transport in the LWIR Regime	127
7.1	Introduction	127
7.2	SL Structure Optimization	128
7.3	Mobility for Optimized Structures with Ideal Interfaces	131

7.4	Effects Disordered Interfaces on Optimized Structures	133
7.5	Conclusion	136
8	Conclusion	137
A	Ballistic Mobility and Resistance	140
A.1	3D Bulk Ballistic Mobility	140
A.2	3D Bulk Ballistic Resistance	142
	Bibliography	144
	Curriculum Vitae	159

LIST OF TABLES

5.1	The diffusive vertical hole mobility as calculated using the resistance scaling method for a 3/3 ML InAs/GaSb SL at 30 K with an electric field strength of 100 V cm^{-1} using the mean, maximum, and minimum hole densities, respectively, for the data set that includes the 50 nm, 100 nm, 150 nm, 200 nm, and 250 nm calculations. Reprinted with permission from Glennon et al. (2023).	87
-----	---	----

LIST OF FIGURES

2.1	Representation of InAs/GaSb band structure where the band gaps of each layer are colorized.	11
2.2	Representation of InAs/InAsSb band structure where the band gaps of each layer are colorized.	12
2.3	Representation of a W SL band structure, as proposed in Aifer et al. (2005), where the band gaps of each layer are colorized.	13
2.4	Representation of M SL band structure, as proposed in Ref. Nguyen et al. (2007c), where the band gaps of each layer are colorized.	15
2.5	Representation of N SL band structure, as proposed in Ref. Salihoglu et al. (2012), where the band gaps of each layer are colorized.	16
2.6	The absorption coefficient extracted for (a) MWIR Ga-free and Ga-based SLs from Klipstein et al. (2014) and (b) a LWIR Ga-free SL from Manyk et al. (2019).	17
2.7	The vertical carrier mobility extracted for (a) electrons (Swartz & Myers, 2014; Taghipour et al., 2017; Casias et al., 2020; Gui et al., 1998) and (b) holes (Olson et al., 2017; Casias et al., 2020; Tsai et al., 2020; Soibel et al., 2020; Arounassalame et al., 2022; Gui et al., 1998) from various publications for T2SL structures in the MWIR and LWIR regimes.	18
2.8	The experimental minority hole lifetime extracted for various T2SLs in the MWIR and LWIR regimes.	20

2.9	The QE extracted for backside-illuminated nBn devices with (a) MWIR Ga-free (Arounassalame et al., 2022) and Ga-based (Bishop et al., 2008) SL active regions. Also included is the QE extracted for an nBn device with a (b) LWIR Ga-free SL active region (Gunapala et al., 2019).	21
3.1	The Konstantinov-Perel contour for the exact solution to the Green's function as presented in (Stefanucci & Van Leeuwen, 2013). The offset from the time axis is for illustration purposes only.	33
3.2	The Keldysh contour for the solution to the Green's function in the adiabatic approximation as presented in (Stefanucci & Van Leeuwen, 2013), with (a) and without (b) initial correlations. The offset from the time axis is for illustration purposes only.	34
4.1	Simplified band diagrams of a (a) pin and an (b) nBn PD.	54
4.2	Simplified band diagrams of a (a) pin and an (b) nBn PD with representations of SRH scattering in the depletion regions of the devices.	55
4.3	Simplified band diagrams of a (a) pin and an (b) nBn PD with representations of diffusion dark current in the quasi-neutral regions of the devices.	57
4.4	Simplified band diagrams of a (a) pin and an (b) nBn PD with representations of tunneling in the pin device and lack of tunneling in the nBn device.	59
4.5	Calculated QE for simple models of pin and nBn detectors with the same material parameters and the same active region thickness. The depletion region extends into the active region in the homojunction pin, but the depletion region is encompassed completely within the barrier layer. Photogenerated carriers in the depletion region of the device are collected efficiently resulting in higher QE for the pin device at lower temperatures.	62

5.1	The apparent, ballistic, and diffusive-limited mobility calculated for an example InAs device at 77 K as a function of device length. Reprinted with permission from Glennon et al. (2023).	67
5.2	The calculated energy band structure of a 3/3 nm InAs/GaSb SL plotted as a function of the transverse wave vector and modified with vertical lines representing the dispersion in the vertical wave vector. The band gap results in a cut-off wavelength of approximately $5\mu\text{m}$. Reprinted with permission from Glennon et al. (2023).	68
5.3	Example band diagrams for the (a) electron and (b) hole mobility calculations.	70
5.4	The calculated hole velocity magnitude (light red line with x's) and density (dark red dashed line with asterisks) throughout the growth direction of a 100 nm MWIR InAs/GaSb structure. Reprinted with permission from Glennon et al. (2023).	71
5.5	A conceptual model demonstrating that a simple average of the velocity over space, without accounting for variation of density, will overestimate the true average velocity per particle, as the concentration of low velocity particles is far higher than high velocity particles. Reprinted with permission from Glennon et al. (2023).	72
5.6	A conceptual model that demonstrates that a simple spatial average of velocity over the entire structure will overestimate the average velocity of the particle as it transits the SL as the particle is spending significantly more time in the wells at lower velocities. Reprinted with permission from Glennon et al. (2023).	73

5.7	The apparent vertical electron (blue line with asterisks) and hole (red line with x's) mobility as a function of temperature calculated using the average velocity method for a 200nm MWIR T2SL with an electric field of strength $2,000 \text{ V cm}^{-1}$ (100 V cm^{-1}). Reprinted with permission from Glennon et al. (2023).	74
5.8	The vertical electron mobility as a function of temperature (green line with x's) for a $4.3 \mu\text{m}$ LWIR SL as reported by Swartz and Myers Swartz & Myers (2014). Also plotted are the apparent vertical electron (blue dashed line with pluses) and hole (red dotted line with asterisks) mobility calculated using the average velocity method for a 200nm MWIR T2SL. Reprinted with permission from Glennon et al. (2023).	76
5.9	The calculated apparent vertical electron (a) and hole (b) mobility as a function of temperature for different simulation sizes, as calculated via the average velocity method. Reprinted with permission from Glennon et al. (2023).	77
5.10	The mobility calculated as a function of electric field strength for (a) electrons and (b) holes at a temperature of 200 K using the resistance scaling method. Reprinted with permission from Glennon et al. (2023).	79
5.11	The calculated vertical electron (hole) mobility as a function of temperature for simulation sizes of (a) ((d)) 100nm, (b) ((e)) 150nm, and (c) ((f)) 200nm, respectively, as calculated via the ballistic approximation method. The apparent mobility (dark blue/red line with x's) is broken up into components of ballistic mobility (blue/red line with asterisks) and diffusive mobility (light blue/red line with crosses). Reprinted with permission from Glennon et al. (2023).	81

5.12	The calculated LDOS (in 10^{15} cm^{-3}) at 200 K for the SL structure used to calculate hole transport for a calculation with (a) ACO and POP scattering and one (b) without scattering overlaid on top of the conduction and valence bands of the SL structure. The portion of the LDOS corresponding with the conduction miniband states have been removed for clarity. Reprinted with permission from Glennon et al. (2023).	83
5.13	The mobility calculated as a function of temperature and density mesh spacing size using the ballistic approximation for (a) electrons and (b) holes with electric field strengths of $2,000 \text{ V cm}^{-1}$ and 100 V cm^{-1} , respectively. Reprinted with permission from Glennon et al. (2023).	85
5.14	The resistance-area product (green lines) and hole density (purple dotted lines), respectively, calculated for majority holes as a function of simulation size at temperatures of 30 K and 77 K. Linear regression on the 30 K (77 K) resistance data gives an R^2 value of 0.994 (0.999). Reprinted with permission from Glennon et al. (2023).	87
5.15	The diffusive vertical hole mobility calculated using the resistance scaling method for each combination of pairs of calculations with consecutive simulation sizes at temperatures of 30 K (yellow lines) and 77 K (red dotted lines). The mobility is calculated using three different values for the hole density: the maximum, the mean, and the minimum of the two calculations in the pair. Reprinted with permission from Glennon et al. (2023).	88

5.16 The diffusive vertical mobility as a function of temperature for a MWIR InAs/GaSb SL calculated using the resistance scaling method from quantum transport simulations by using Eq. (5.10) (dark red line with error bars) and Eq. (3.98) (light red dashed line with asterisks) for holes. Also plotted is the vertical mobility for electrons calculated using Eq. (5.10) (blue line with pluses). Finally, the experimentally obtained electron vertical mobility as a function of temperature (green line with x's) for a $4.3\mu\text{m}$ LWIR SL as reported by Swartz & Myers (2014). Reprinted with permission from Glennon et al. (2023). 89

5.17 The resistance-area product (green lines) and electron density (purple dotted lines), respectively, calculated for majority electrons as a function of simulation size at temperatures of 77 K, 120 K, and 160 K. Linear regression on the resistance results in R^2 values of 0.990, 0.992, and 0.993, respectively. Reprinted with permission from Glennon et al. (2023). 90

5.18 The resistance-area-density product calculated for majority electrons as a function of simulation size at several temperatures. Linear regression was performed on the calculations with lengths of 200 nm and greater returning R^2 values of 0.992, 0.995, 0.997, 0.998, and 0.997, respectively, suggesting that valid mobility may be extracted using Eq. (3.98). Reprinted with permission from Glennon et al. (2023). 91

5.19	The electron (data at higher energy levels) and hole (data at lower energy levels) spatially resolved spectral currents (in 10^6 Acm^{-2} and 10^4 Acm^{-2} , respectively) and scattering rates (in $10^{26} \text{ s}^{-1}\text{cm}^{-3}$ and $10^{24} \text{ s}^{-1}\text{cm}^{-3}$, respectively) associated with POP scattering for a 200 nm simulation at 77 K. POP scattering is size-dependent for electrons, but nearly size-independent for holes at this scale. Note that this figure is a composite plot of two separate calculations, one for electrons and one for holes, with electric field strengths of 100 V cm^{-1} and $2,000 \text{ V cm}^{-1}$, respectively. Thus, the SL band diagrams were only included in the two insets as they would conflict in the composite plot. (The spectral currents are displayed in a gray scale color map while the POP scattering rates are displayed in a blue/red color map.) Reprinted with permission from Glennon et al. (2023).	92
5.20	The electron (dark blue line with x's) and hole (dark blue line with pluses) apparent vertical mobility plotted as a function of temperature calculated using the average velocity method. Also, the apparent vertical mobility calculated by combining diffusive and ballistic components using Matthiessen's rule derived from resistance scaling analysis for electrons (light blue dotted line with diamonds) and holes (light red dotted line with squares). These results correspond with simulation sizes of 200 nm. Reprinted with permission from Glennon et al. (2023).	95
5.21	The diffusive vertical electron and hole mobility as a function of temperature calculated using both resistance scaling analysis (Eq. (3.98)) and the ballistic approximation method (Eq. (5.1)) from 200 nm simulations. Reprinted with permission from Glennon et al. (2023).	96

6.1	The energy band structure of the SL structure with (a) ideal and (b) graded interfaces calculated as a function of the transverse wave vector. It is modified with vertical lines representing the dispersion in the vertical wave vector.	100
6.2	The Sb concentration profile of an MWIR InAs/InAsSb SL. The nominal (red line) and graded (black line) concentration profiles are plotted along with the actual profile represented by bar plot with one bar per spatial mesh node in the case of (a) no disorder and (b) disorder. Note, the nominal profile demonstrates the Sb concentration of the Muraki model SL if no Sb segregation occurred. This is a different ternary alloy composition than that of the ideal SL that was also investigated. Reprinted with permission from Glennon et al. (2024).	101
6.3	Histogram of the cutoff wavelengths calculated for (a) low and (b) high disorder SLs with ternary alloy layer compositions of InAs _{0.65} Sb _{0.35} and InAs _{0.48} Sb _{0.52} . Reprinted with permission from Glennon et al. (2024).	102
6.4	Band diagrams of the (a) ideal, (b) no disorder, (c) low disorder, and (d) high disorder ga-free SLs for the simulations with domain size of approximately 120 nm. Reprinted with permission from Glennon et al. (2024).	103
6.5	example	104
6.6	Examples of the InAs _{1-x} GaSb _x alloy composition profile (colorbar) for one SL period of the modified-Muraki structure in the case of (a) no disorder and (b) disorder as a function of spatial node. The nominal and modified-Muraki alloy composition profiles are overlaid on top to demonstrate the impact that atomic incorporation and disorder have on the intended SL structure. Reprinted with permission from Glennon & Bellotti (2023).	105

6.7	Band diagrams of the (a) ideal, (b) no disorder, (c) low disorder, and (d) high disorder Ga-based SLs for the simulations with domain size of approximately 120 nm. Partially reprinted with permission from Glennon & Bellotti (2023).	106
6.8	The components of the strain vector $\vec{S} = \{\epsilon_{xx}, \epsilon_{yy}, \epsilon_{zz}, \gamma_{xy}\}$ extracted from a FEA calculation of a $45 \text{ mm} \times 50 \text{ mm} \times 100 \mu\text{m}$ InAsSb die curved to an ROC of 70 mm.	107
6.9	The (a) projected axisymmetric strain calculated from the strain configuration extracted from the FEA calculations of a curved-FPA die with a ROC of 70 mm presented in Fig. 6.8. Also included is the (b) residual strain component from the transformed strain vector that is not included in the Hamiltonian. Reprinted with permission from Glennon et al. (2024).	109
6.10	The vertical hole mobility calculated as a function of temperature for the ideal (blue line with circles), no disorder (cyan line with diamonds), low disorder (green line with triangles), and high disorder (red line with squares) structures for the (a) Ga-free and (b) Ga-based SLs. Also plotted are experimental results for vertical hole mobility reported in (a) Casias et al. (2020) (black dotted line with x's) and (b) Liu et al. (2022) (gray dotted line with +'s) for two different MWIR InAs/InAsSb SLs. Ga-free plot ((a)) is reprinted with permission from Glennon et al. (2024).	110
6.11	The hole current spectrum as a function of position for example structures of the (a) ideal, (b) no disorder, (c) low disorder, and (d) high disorder Ga-based SLs, normalized to the maximum value in the ideal structure, for the simulations with domain size of approximately 120 nm at 200 K. Reprinted with permission from Glennon & Bellotti (2023).	112

6.12	The vertical hole mobility calculated as a function of temperature for different magnitudes of negative (positive) axisymmetric strain for the Ga-free (a) ((b)) ideal, (c) ((f)) no disorder, (d) ((g)) low disorder, and (e) ((h)) high disorder SLs. Reprinted with permission from Glennon et al. (2024).	113
6.13	The energy band structure of the ideal Ga-free SL calculated as a function of the transverse wave vector for external axisymmetric strains of (a) $-1.2%$, (b) $-0.5%$, (c) $0.0%$, (d) $+0.5%$, (e) $+0.8%$, and (f) $+1.6%$. It is modified with vertical lines representing the dispersion in the vertical wave vector. Reprinted with permission from Glennon et al. (2024).	114
6.14	The (a) vertical hole mobility calculated as a function of positive axisymmetric strain for each SL structure. Also included are the band structures calculated for the (b) ideal and (c) no disorder SL in which the HH and LH separation is negligible. Reprinted with permission from Glennon et al. (2024).	116
6.15	The (a) ((d)) vertical hole mobility, (b) ((e)) minority hole diffusion length, and (c) ((f)) subsequent QE calculated for a backside illuminated nBn device as a function of axisymmetric strain for the Ga-free ideal (blue line with circles), no disorder (cyan line with diamonds), low disorder (green line with triangles), and high disorder (red line with squares) SLs for the Ga-free (Ga-based) SL. The shaded areas indicate the minimum and maximum values obtained from the different disordered structures for each strain value. The ideal structures do not have disorder, so there is no shaded area. (a) ((d)), (b) ((e)), and (c) ((f)) adapted with permission from Glennon et al. (2024) (Glennon & Bellotti (2023)).	119

6.16	Approximate internal QE calculated as a function of spatial coordinates of the curved die at 120 K for the ideal, no disorder, low disorder, and high disorder SLs for a Ga-based nBn detector. (a) ((b)) adapted with permission from Glennon et al. (2024) (Glennon & Bellotti (2023)).	121
6.17	2σ of approximated QE calculated as a function of spatial coordinates of the curved die at 120 K for the ideal, no disorder, low disorder, and high disorder SLs. Reprinted with permission from Glennon et al. (2024). . . .	123
6.18	2σ of approximated QE calculated as a function of spatial coordinates of the curved die at 120 K for the ideal, no disorder, low disorder, and high disorder SLs. Reprinted with permission from Glennon & Bellotti (2023). .	124
6.19	The internal QE estimated as a function of temperature for the Ga-free (a) ideal, (b) no disorder, (c) low disorder, and (d) high disorder SLs under +0.0% (blue line with circles), +0.8% (green line with triangles), and +1.6% (red line with squares) axisymmetric strain. Adapted with permission from Glennon et al. (2024).	125
7.1	The band structures calculated for the (a) 14/5 ML InAs/InAs _{0.43} Sb _{0.57} structure and the (b) 21/12 ML InAs/InAs _{0.61} Sb _{0.39} structure on a GaSb substrate and the (c) 16/7 ML InAs _{0.66} Sb _{0.34} /InAs _{0.48} Sb _{0.52} structure on a 6.2 Å substrate. The vertical lines represent the dispersion with respect to the vertical wave vector.	131
7.2	Examples of the band diagrams for the (a) InAs/InAs _{0.43} Sb _{0.57} and the (b) InAs/InAs _{0.61} Sb _{0.39} on a GaSb substrate and (c) InAs _{0.66} Sb _{0.34} /InAs _{0.48} Sb _{0.52} on a 6.2 Å substrate structures.	132

7.3 The vertical hole mobility calculated as a function of temperature for the 34/6 ML $\text{InAs}_{0.97}\text{Sb}_{0.03}/\text{InAs}_{0.52}\text{Sb}_{0.48}$ structure (green line with circles) and $\text{InAs}/\text{InAs}_{0.61}\text{Sb}_{0.39}$ structure (red line with triangles) both on a GaSb lattice and the 5/3 ML $\text{InAs}_{0.66}\text{Sb}_{0.34}/\text{InAs}_{0.48}\text{Sb}_{0.52}$ structure (blue line with diamonds) on a 6.2 Å substrate for ideal interfaces. 133

7.4 Example band diagrams of an $\text{InAs}/\text{InAs}_{0.43}\text{Sb}_{0.57}$ SL structure with (a) ideal and (b) disordered interfaces, on a GaSb substrate. 134

7.5 The vertical hole mobility calculated as a function of temperature for the 34/6 ML $\text{InAs}_{0.97}\text{Sb}_{0.03}/\text{InAs}_{0.52}\text{Sb}_{0.48}$ structure (green line with circles) and $\text{InAs}/\text{InAs}_{0.61}\text{Sb}_{0.39}$ structure (red line with triangles) both on a GaSb lattice and the 5/3 ML $\text{InAs}_{0.66}\text{Sb}_{0.34}/\text{InAs}_{0.48}\text{Sb}_{0.52}$ structure (blue line with diamonds) on a 6.2 Å substrate for positional disordered interfaces. The range of mobility for each structure is included as a shaded area around the mean data. 134

LIST OF SYMBOLS AND ABBREVIATIONS

BLIP	background limited performance
cFPA	curved focal plane array
EFA	envelope-function approximation
EMA	effective mass approximation
FEA	finite element analysis
FET	field effect transistor
FPA	focal-plane array
GR	generation and recombination
HEMT	high-electron mobility transistor
HH	heavy-hole
HOT	high operating temperature
LWIR	long-wave infrared
ML	monolayer
MWIR	mid-wave infrared
NEGF	nonequilibrium Greens functions
PD	photodetectors
QE	quantum efficiency
QWIP	quantum well infrared photodetector
ROC	radius of curvature
SL	superlattice
SRH	Shockley-Read-Hall
T2SL	type-ii superlattices

CHAPTER 1

Introduction

1.1 MOTIVATION

Type-II superlattices (T2SLs) have been developed as an important class of quantum structures based on III-V and other semiconductor materials. Specifically, T2SLs based on III-V materials are being investigated as an alternative to the established II-VI bulk material system for infrared (IR) photodetection due to the tunability of the band gap over a large portion of the IR spectrum (Rogalski et al., 2017). These materials exhibit some predicted advantages over the established HgCdTe material system. However, the demonstration of superior performance of these materials is still elusive (Rogalski et al., 2019). Proposed T2SL materials include Ga-based (Rehm et al., 2009; Nguyen et al., 2007b; Martyniuk et al., 2014; Delmas et al., 2017; Klipstein, 2022) and Ga-free (Ting et al., 2009; Haddadi et al., 2014; Ting et al., 2020) superlattices (SLs) as well as more complicated structures such as the “W” (Meyer et al., 1995; Aifer et al., 2005, 2006, 2010; Olson et al., 2016), “M” (Nguyen et al., 2007c,a, 2008, 2009; Delaunay et al., 2009; Lang & Xia, 2013; Chevallier et al., 2017; Du et al., 2020; Singh et al., 2022), and “N” (Salihoglu et al., 2012, 2014; Hostut et al., 2015; Wu et al., 2016; Akel et al., 2018; Du et al., 2020) structures. The abundance of different structures in the T2SL material system demonstrates the incredibly versatility this material system offers in terms of band structure design, but it also highlights a problem in optimizing these materials to realize the theoretical advantages. Experimental realization and characterization of IR T2SL materials and devices is costly and time consuming. With an effectively infinite parameter space of different T2SL designs, a comprehensive experimental investigation aimed at optimizing the structures would require significant investment. Thus, methodologies for simulating the physics of these materials

could provide significant aid in the development of this material system and reduce the resources required for developing viable prototypes. This work will focus on the simulation of carrier transport in T2SL materials across several investigations. The overarching goal is to simulate the performance of advanced materials and devices for use in the field of IR photodetection.

Mobility is an important component of diffusion length and impacts the collection of photogenerated carriers in PDs. While techniques exist for studying the vertical carrier mobility in T2SLs, such as magnetotransport (Umana-Membreno et al., 2012; Swartz & Myers, 2014) and time-of-flight (Olson et al., 2013) methods, they can be challenging resulting in relatively few studies. The field would greatly benefit from the development of a method to systematically study mobility in T2SLs using simulation. To the author's knowledge, prior to the work in this dissertation there had not yet been a comprehensive analysis of the extraction of mobility from quantum transport simulations for application to IR PDs. This is important, because as devices shrink, the concept of mobility requires careful consideration due to the increasing influence of contact and ballistic resistances to carrier transport (Shur, 2002; Niquet et al., 2014). Concurrently, quantum transport simulations are computationally expensive, so the domain size of the simulations can be limited according to computational resources. Thus, the impact of this device size dependence on the apparent mobility needs to be taken into account when predicting device properties for a larger structure. To this end, a comprehensive investigation on the extraction of mobility from non-equilibrium Green's functions (NEGF) for use in predicting T2SL IR PD performance will be presented in Chapter 5. In later chapters, this information will be used as the foundation for investigations of the fundamental transport properties of various T2SL structures.

An emerging architecture in the field of IR sensors is the curved focal-plane array

(cFPA). This design is a modification of the standard focal-plane array (FPA) in which the planar device is mechanically curved, resulting in a structure that exhibits fewer optical aberrations and a reduced optical footprint (Guenter et al., 2017). For T2SL materials to achieve ubiquitous use they must be compatible with the state-of-the-art device designs. However, the curving procedure of the cFPA introduces another complexity in the prediction of T2SL material performance. The curving procedure introduces an additional strain which can affect the electrical characteristics of the material. This work will present the results of two investigations into the use of the two most common T2SL materials in mid-wave (MWIR) cFPAs in Chapter 6.

The biggest hurdle to the adoption of T2SLs as a material of choice for IR PDs is the failure of these materials to achieve the performance of state-of-the-art HgCdTe in many applications (Rogalski et al., 2019). The effectively infinite parameter space of T2SL designs presents a challenge in finding structures that are optimized for particular properties due to the high cost of experiment and characterization of T2SL materials. A methodology developed to search for optimized structures through simulation could lead to the development of T2SL materials with enhanced performance. To this end, the results of a study on the development of a method for optimizing n-type T2SLs devices in the long-wave (LWIR) regime, which suffer from relatively low QE (Gunapala et al., 2019), for enhanced hole transport will be presented in Chapter 7. The focus of the study is on predicting the hole transport efficiency based on band structure calculations and Gaussian process regression.

1.2 OUTLINE

The remainder of this dissertation will be organized into seven chapters. Chapter 2 will be an introduction into the field of IR materials for photodetection, focusing particularly on

T2SLs. An overview of the quantum transport formalism used to study carrier transport in T2SLs will be presented in Chapter 3. A brief overview of a few analytical models for predicting IR PD performance will be given in Chapter 4. Chapter 5 will present the results of a comprehensive investigation into the extraction of mobility from quantum transport simulations for T2SLs. Chapter 6 will present the results of two studies on MWIR T2SL-based cFPAs predicting the QE for different magnitudes of structural disorder. An investigation into optimizing LWIR Ga-free T2SL structures for enhanced hole mobility will be presented in Chapter 7. Finally, general conclusions will be given in Chapter 8.

CHAPTER 2

Infrared Photodetection

Infrared (IR) sensors have several properties that make them important devices in several fields. IR radiation is emitted by objects when at a temperature between 30 K and 4,000 K (Razeghi & Nguyen, 2014), as determined by Wien's displacement law:

$$\lambda_{max} = \frac{2898}{T}, \quad (2.1)$$

where the wavelength λ_{max} is in mm and T is the temperature in Kelvin. This means that objects at these temperatures can be detected without additional light sources, a process called "passive sensing". This is particularly advantageous for defense (Rogalski, 2003) and astronomical applications (Beletic et al., 2008). Additionally, IR radiation has bands of high atmospheric transmission, particularly in the mid-wave (MWIR) ($3\mu m - 5\mu m$) and long-wave (LWIR) ($8\mu m - 12\mu m$) regimes (Rogalski, 2003). Specifically, objects at a temperature of 300 K emit radiation at a wavelength of $9.7\mu m$. This allows for imaging of objects through atmospheric haze. The most common IR sensors fall into two categories: thermal sensors and photonic sensors.

Thermal sensors were early examples of IR detectors. The operating principal for thermal detectors is that incoming IR radiation will change the temperature of the sensing material. Then, some temperature-dependent mechanism is measured in the sensing material which determines the temperature of the target object (Rogalski, 2003). There are several drawbacks to this category of IR detectors. Specifically, they are typically wavelength independent, preventing the analysis spectral content and they have relatively slow response times (Rogalski, 2003) compared with photonic sensors. However, it is worth mentioning that microbolometers can still be competitive, particularly in the LWIR regime, for low cost

IR detection due to the ability for detection at room temperature Rogalski et al. (2023).

Photonic sensors operate through the absorption of a photon in a semiconductor absorber layer and the subsequent collection of the photogenerated charge carriers. In contrast with thermal sensors, photonic sensors exhibit a wavelength dependent response to incident photon flux (Rogalski, 2003). They can achieve perfect signal-to-noise and fast response times; however, they do require cooling (Rogalski, 2003). The state-of-the-art high operating temperature (HOT) IR photodetectors (PDs) are typically photonic detectors with HgCdTe absorber layers (Rogalski et al., 2023). In the following sections, I will provide a brief overview of three of the most common material categories for MWIR and LWIR PDs: HgCdTe, quantum well infrared photodetectors (QWIPs), and type-II superlattices (T2SLs). The rest of this dissertation will focus on T2SL photonic detectors for the potential use in high-performance MWIR and LWIR PDs.

2.1 BULK HgCdTe

Bulk HgCdTe is the typical material of choice in IR PDs that require the highest performance (Kinch, 2007; Rogalski et al., 2023). This can be attributed to the fact that at present, they exhibit the most favorable properties for simultaneously achieving high-QE and background-limited performance (BLIP) at higher temperatures (Rogalski et al., 2023). This includes a composition dependent band gap (BG) that ranges from a negative gap to $1.5eV$ (Bianconi & Mohseni, 2020). Additionally, these materials exhibit high absorption coefficients, vertical carrier mobility, and minority carrier lifetimes (Rogalski et al., 2023). I will elaborate further on some of these properties in Section 2.3.2 as a point of comparison with those of T2SLs. While these properties are very advantageous for IR detectors, there are several disadvantages of using HgCdTe compared to alternative options. Firstly, the II-VI bonds are relatively weak, leading to surface and interface defects (Bianconi &

Mohseni, 2020). Furthermore, they tend to suffer from relatively poor uniformity and low yield, resulting in increased costs of production (Bianconi & Mohseni, 2020). Additionally, the substrate used for growing HgCdTe is CdZnTe which has a low industrial base and high cost (Bajaj et al., 2007). Lastly, the cutoff wavelength of bulk ternary alloys are adjusted by a single composition parameter. This reduces the ability to optimize structures for specific use cases in contrast with the versatility of quantum structures like QWIPs and T2SLs (Razeghi & Nguyen, 2014). QWIPs and T2SLs present a potential alternative which may not reach the same level of performance, but could provide adequate performance for specific use cases at a reduced cost.

2.2 QUANTUM WELL INFRARED PHOTODETECTORS

QWIPs are a type of intersubband photonic device that are typically developed with more chemically stable wide BG materials (Rogalski, 2003). Thus, high yield relative to HgCdTe results in reduced cost (Chen et al., 2022). As mentioned in the previous section, an additional advantage is that the spectral response of a QWIP can be adjusted in various ways (material, structure), which provides greater versatility in optimization and design of devices. At temperatures below 50K, QWIPs can be competitive with HgCdTe (Chen et al., 2022). However, there are several disadvantages that limit the overall performance of these materials. The intersubband process typically involves the excitation of electrons from the ground state to an excited state. This can be done in a bound-to-bound process in which the excited state is still confined to the well or in a bound-to-continuum process in which the excited state is in the continuum state above the well barrier (Chen et al., 2022). Due to the selection rules associated with this type of transition, normal incident light is not able to be absorbed. This severely reduces the quantum efficiency (QE) that can be achieved with these devices alone, and require additional components (like grating) to improve this value

(Rogalski, 2011). For example, Choi et al. (2015) demonstrated a resonator-QWIP design which was able to achieve a QE of up to 40% in the LWIR regime. Additionally, the relatively high thermal generation rate in QWIPs results in maximum operating temperatures that are much lower than state-of-the-art detectors in the MWIR and LWIR regimes (Rogalski, 2003). QWIPs are more competitive for longer wavelength infrared regimes where HgCdTe and T2SLs require low operating temperatures as well (Rogalski, 2003).

2.3 TYPE-II SUPERLATTICES

Type-II superlattices (T2SLs) are an important class of quantum structures based on III-V and other semiconductor materials. In particular, T2SLs based on III-V materials are being investigated as an alternative to the established II-VI bulk material system for infrared (IR) photodetection. They can be thought of as a hybrid between bulk infrared materials and QWIPs, incorporating a combination of the benefits of each material class. Absorption occurs via interband processes between minibands, similar to bulk materials. However, they also exhibit substantial structural control over the response of these materials to particular infrared bands. The type-II overlap in these structures allows for significant wavefunction overlap between wells in the structure, resulting in the formation of minibands (Razeghi & Nguyen, 2014). Of which, the BG can be tuned over a large portion of the IR spectrum (Rogalski et al., 2017). These materials exhibit some predicted advantages over the more established bulk II-VI material system due to theoretically lower Auger recombination rates (Youngdale et al., 1994) and stronger chemical bonding (Rogalski et al., 2017). Furthermore, there is a large existing industrial base for III-V materials which should result in reduced manufacturing costs (Bajaj et al., 2007). However, the demonstration of superior performance of these materials is still elusive (Rogalski et al., 2019). The two most common T2SL materials are the Ga-based (Rehm et al., 2009; Nguyen et al., 2007b; Martyniuk

et al., 2014; Delmas et al., 2017; Klipstein, 2022) and Ga-free (Ting et al., 2009; Haddadi et al., 2014; Ting et al., 2020) superlattices (SLs). These two different material systems have competing advantages. With the inclusion of more complicated structures such as the “W” (Meyer et al., 1995; Aifer et al., 2005, 2006, 2010; Olson et al., 2016), “M” (Nguyen et al., 2007c,a, 2008, 2009; Delaunay et al., 2009; Lang & Xia, 2013; Chevallier et al., 2017; Du et al., 2020; Singh et al., 2022), and “N” (Salihoglu et al., 2012, 2014; Hostut et al., 2015; Wu et al., 2016; Akel et al., 2018; Du et al., 2020) structures. These structures are composed of an underlying SL structure, like the Ga-based or Ga-free version, with an additional repeating barrier layer incorporated within the SL period. With these various structures, fine control over the band structure of a photodetector can be achieved using T2SLs.

I will present a summary of these structures in Section 2.3.1. Then, I will discuss several important material properties for predicting IR device performance comparing those of T2SLs with state-of-the-art HgCdTe in Section 2.3.2. Finally, I will present the QE that is achieved in some T2SL IR PDs and compare them with a few alternatives in Section 2.3.3.

2.3.1 Type-II Superlattice Structures

InAs/Ga(In)Sb SLs were first proposed as a viable material for application in IR detectors by Smith & Mailhot (1987). Since then, T2SLs have been investigated as an alternative to the more established bulk material systems. As described in Ting et al. (2020), the investigation into Ga-free InAs/InAsSb SLs predates InAs/Ga(In)Sb (Osborn, 1984), but renewed interest was generated in the use of the material for IR detection when significantly longer minority carrier lifetimes were demonstrated in InAs/InAsSb SLs than in InAs/GaSb SLs for LWIR (Steenbergen et al., 2011). While these two structures are the most common, several more complex III-V heterostructures have been developed as well, including the so-

called “W” (Aifer et al., 2005), “M” (Nguyen et al., 2007c), and “N” (Salihoglu et al., 2012) structures. A brief review of these structures will be provided in this section.

T2SL structures tend to suffer from relatively short SRH lifetimes (Kopytko & Rogalski, 2022). Thus, basic pin PDs tend to suffer from high dark current, reducing the operating temperature (Li et al., 2019). As mentioned in Rogalski et al. (2023), achieving HOT is a main goal of modern high performance IR PDs. To reduce this dark current, various barrier detector architectures have been utilized (Martyniuk et al., 2014). One popular device is the nBn photodetector which has been designed specifically to reduce the dark current associated with GR mechanisms, tunneling currents, and surface leakage (Maimon & Wicks, 2006). The depletion region extends nearly exclusively over the large gap barrier layer reducing the dark current associated with SRH mechanisms. Additionally, by selectively etching to the top of the barrier layer a natural passivation layer is provided (Maimon & Wicks, 2006). Finally, band-to-band tunneling current is reduced due to the electric field being confined to the wide gap material layer. In this dissertation, we will investigate several T2SL structures and will focus on the application of these materials to the current nBn designs.

2.3.1.1 InAs/GaSb

InAs/GaSb SLs have been investigated as an alternative to the more established bulk material systems for IR detection, particularly for MWIR and LWIR (Rogalski et al., 2017). Reasonably high quantum efficiency (QE) has been demonstrated for InAs/GaSb absorbers in both the MWIR (Rehm et al., 2009; Hostut & Ergun, 2021) and LWIR (Nguyen et al., 2007b; Hostut & Ergun, 2021) regimes. Furthermore, theoretical predictions indicate that these SLs should exhibit significantly reduced Auger recombination when compared with bulk materials (Smith et al., 1985; Grein et al., 1993; Youngdale et al., 1994). While suf-



Figure 2.1: Representation of InAs/GaSb band structure where the band gaps of each layer are colorized.

fering from higher dark current when compared with HgCdTe (MCT), the development of barrier architectures has significantly improved the performance of IR PDs utilizing this SL (Martyzniuk et al., 2014; Delmas et al., 2017; Klipstein, 2022).

InAs/GaSb is a type-II SL which means that the conduction band of the InAs layer overlaps the valence band of the GaSb layer (Rogalski et al., 2017). The high conduction and valence band offsets between InAs and GaSb allow for relatively narrow well thicknesses. This improves the spatial overlap of the electron and hole wavefunctions resulting in higher absorption near the cut-off wavelength compared with InAs/InAsSb SLs (Klipstein et al., 2014). A representation of the InAs/GaSb SL structure is given in Fig. 2.1.

2.3.1.2 InAs/InAsSb

InAs/InAsSb SLs have several advantages over InAs/GaSb SLs, including a simpler growth process and high defect tolerance (Ting et al., 2022a). However, the most consequential advantage is that InAs/InAsSb has been demonstrated to have much longer minority carrier lifetimes in the MWIR (Höglund et al., 2013) and LWIR (Steenbergen et al., 2011) regimes than Ga-based SLs. However, due to the smaller band offsets compared with InAs/GaSb,

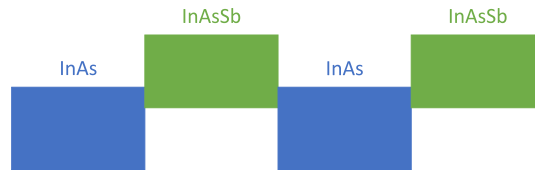


Figure 2.2: Representation of InAs/InAsSb band structure where the band gaps of each layer are colorized.

InAs/InAsSb SLs require larger SL periods to produce the same band gap. The larger spatial separation of the electron and hole wavefunctions results in lower absorption near the cut-off wavelength (Klipstein et al., 2014). Consequently, InAs/InAsSb typically have lower QE values (Alshahrani et al., 2022). This is a particular issue for n-type InAs/InAsSb at longer wavelengths (i.e. LWIR and very-long-wave (VLWIR)) where hole diffusion lengths are short (Ting et al., 2020, 2022a). A representation of the InAs/InAsSb SL structure is given in Fig. 2.2.

2.3.1.3 “W” Structure

The “W” structure SL was first proposed in 1995 by Meyer et al. (1995) as a replacement material for InAs/InGaAs in MWIR lasers with the goal of achieving higher gain. This structure consists of incorporating AlSb barriers between InAs layers which in turn surround a Ga(In)Sb layer. In 2005, Aifer and colleagues proposed using the W structure for the absorber of LWIR and VLWIR PDs (Aifer et al., 2005) and achieved high QE photodiodes using an alternative W structure with AlGaInSb barriers (Aifer et al., 2006). Furthermore, graded-gap devices have been developed that benefit from the precise control



Figure 2.3: Representation of a W SL band structure, as proposed in Aifer et al. (2005), where the band gaps of each layer are colored.

over the band structure that can be achieved using W structures that strongly suppress bulk tunneling and GR in the depletion region of T2SL IR detectors (Canedy et al., 2009; Aifer et al., 2010). Finally, the W structures can also be incorporated into T2SL photodetectors in the form of majority carrier barriers that significantly reduce dark current (Olson et al., 2016). Promising results were achieved using a Ga-free version of the W-structure for the absorber and barrier layers for both MWIR and LWIR photodetection (Olson et al., 2016).

The W structure theoretically should have improved optical properties over traditional T2SLs owing to the increased electron-hole overlap as well as the quasi-2D density of states (Aifer et al., 2005, 2006). Furthermore, the W structure features increased effective masses that can suppress tunneling currents (Aifer et al., 2006). A representation of the W SL structure is given in Fig. 2.3.

2.3.1.4 “M” Structure

Initially proposed in 2007 by Nguyen and colleagues, the “M” structure SL was designed as an alternative to the W structure that exhibits better growth properties. The layer structure consists of the repeating layer pattern AlSb/GaSb/InAs/GaSb/AlSb. The M structure

has all common atom interfaces, while the W structure has AlSb/InAs interfaces which are highly stressed, suggesting that the M structure should have lower defect density (Nguyen et al., 2007c,a). The AlSb barrier layer creates a double quantum well structure for holes, thus affording the M structure precise control over both the conduction and valence mini-band levels (Nguyen et al., 2007c,a). Due to this property, the M structure is a highly versatile barrier layer material that can be tuned to the device requirements (Nguyen et al., 2008). Since its proposal, the M structure barrier has been incorporated in numerous T2SL photodetectors with promising results (Nguyen et al., 2008; Delaunay et al., 2009; Nguyen et al., 2009). Recently, a two-color LWIR T2SL photodetector was demonstrated incorporating M structure barriers and achieving background limited performance (BLIP) at 77K (Chevallier et al., 2017).

Like the W structure, it has been suggested that the M structure may improve absorption as the AlSb barrier pushes the hole wavefunction towards the InAs layers. However, it was demonstrated that the inclusion of AlSb barriers demonstrates no significant enhancement in the absorption coefficient (Lang & Xia, 2013). On the other hand, the inclusion of M barrier layers are predicted to reduce dark current through three main mechanisms: reduced Auger recombination by increasing separation of the heavy-hole (HH) and light-hole (LH) bands, reduced generation-recombination in the depletion region through inclusion of barrier layer, and reduced band-to-band tunneling with increased effective mass (Du et al., 2020). A representation of the M SL structure is given in Fig. 2.4.

2.3.1.5 “N” Structure

The “N” structure was proposed in 2012 by Salihoglu and colleagues as an alternative to the M structure (Salihoglu et al., 2012). The structure consists of periodic layers of InAs/AlSb/GaSb. It is predicted to improve the electron-hole wavefunction overlap over

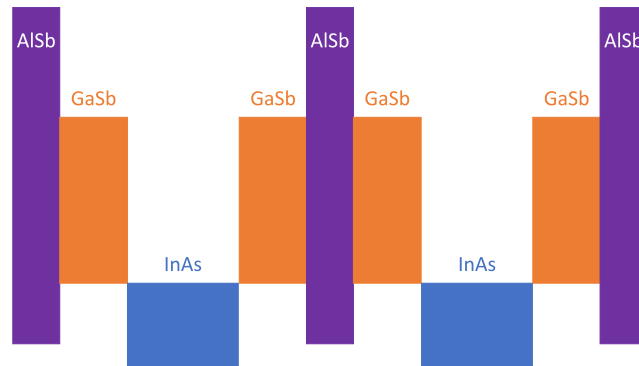


Figure 2.4: Representation of M SL band structure, as proposed in Ref. Nguyen et al. (2007c), where the band gaps of each layer are colorized.

the M structure when in reverse bias while maintaining the other advantages of the M structure (Salihoglu et al., 2012; Hostut et al., 2015; Wu et al., 2016; Akel et al., 2018; Du et al., 2020). Since its proposal, high performance detectors have been demonstrated with N structure absorber and barrier layers that substantially suppress dark current (Salihoglu et al., 2012, 2014; Hostut et al., 2015).

The asymmetric incorporation of the AlSb barrier layer in the N structure compared with the M structure shifts the electron and hole wavefunctions to compensate for the shifts associated with reverse bias. It has been demonstrated theoretically that the inclusion of the AlSb barrier increases absorption at the interface by about 25% (Salihoglu et al., 2012). A representation of the N SL structure is given in Fig. 2.5.

2.3.2 Type-II Superlattice Material Properties

Throughout this dissertation, when studying the transport properties of holes, we will frequently make estimations of the QE for an example device. The three most important material properties for the QE are the absorption coefficient, the vertical carrier mobility, and the minority carrier lifetime. In the following sections, a brief overview of some

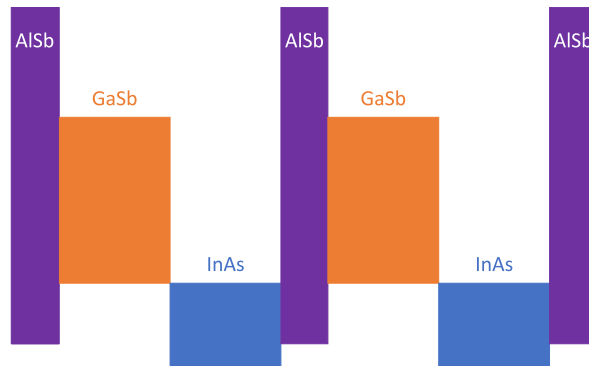


Figure 2.5: Representation of N SL band structure, as proposed in Ref. Salihoglu et al. (2012), where the band gaps of each layer are colorized.

experimental values for these parameters for T2SLs to date will be presented.

2.3.2.1 Absorption

The absorption coefficient is a parameterization of the efficiency of photon absorption through a material as a function of photon energy. When light is incident on a semiconductor material, photons with sufficient energy can excite an electron from the valence band into the conduction band forming a photogenerated electron-hole pair. The efficiency with which this occurs is a function of the electronic properties of the material. In general, bulk materials with direct band gaps like HgCdTe and InSb will exhibit relatively high absorption coefficients near the cutoff energy (Rogalski et al., 2023). While Ga-free and Ga-based T2SLs are typically direct gap materials in reciprocal space, due to the type-II alignment, there is a spatial separation between the electron and hole wavefunctions. Absorption probability is a function of the spatial overlap between the electron and hole wavefunctions, so the absorption coefficients that are achievable in these materials are typically of smaller magnitude. Also, as mentioned in Section 2.3.1.2, Ga-free superlattices typically require thicker SL periods, which results in a reduced absorption coefficient when compared with

Ga-based small period SLs, particularly in the LWIR regime (Alshahrani et al., 2022). The absorption coefficient extracted for Ga-free and Ga-based SLs in the MWIR and for a Ga-free SL in the LWIR regime are reproduced from Klipstein et al. (2014) and Manyk et al. (2019), respectively, in Fig. 2.6. Note that all line plots in this dissertation have been generated using MATLAB[®] with a standardization toolbox (Aalok, 2021).

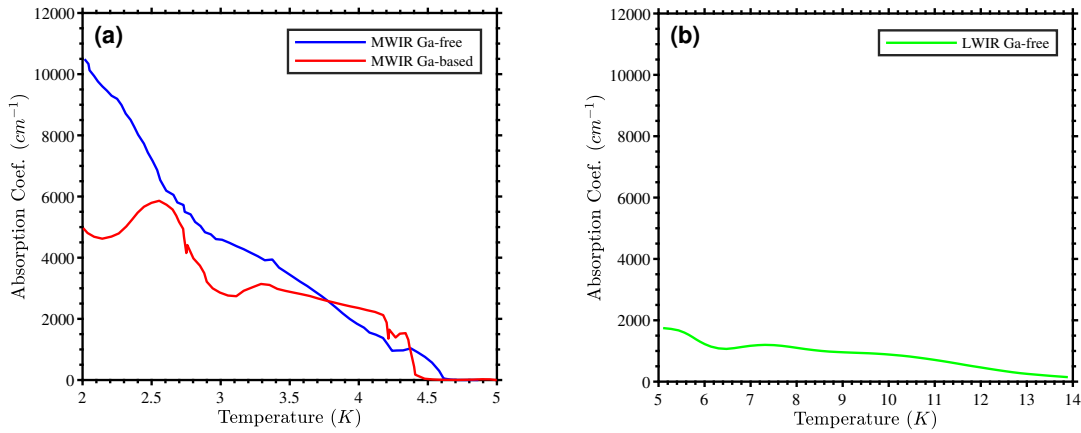


Figure 2.6: The absorption coefficient extracted for (a) MWIR Ga-free and Ga-based SLs from Klipstein et al. (2014) and (b) a LWIR Ga-free SL from Manyk et al. (2019).

These results match expectations with the MWIR Ga-based SL exhibiting the highest absorption coefficient near cutoff ($1,500\text{ cm}^{-1}$) and that of the MWIR Ga-free SL being higher ($1,000\text{ cm}^{-1}$) than the LWIR Ga-free SL (500 cm^{-1}). We will use these values when investigating MWIR Ga-free and Ga-based T2SLs in Chapter 6 and LWIR Ga-free T2SLs in Chapter 7.

2.3.2.2 Vertical Carrier Mobility

Mobility is an important component of diffusion length and can affect carrier collection in PDs. It is a parameterization of the efficiency with which carriers can transport through a material. While techniques exist for studying the vertical carrier mobility in T2SLs, such

as magnetotransport (Umana-Membreno et al., 2012; Swartz & Myers, 2014) and time-of-flight (Olson et al., 2013) methods, they can be challenging, resulting in relatively few studies. I have included the results of several investigations in Fig. 2.7.

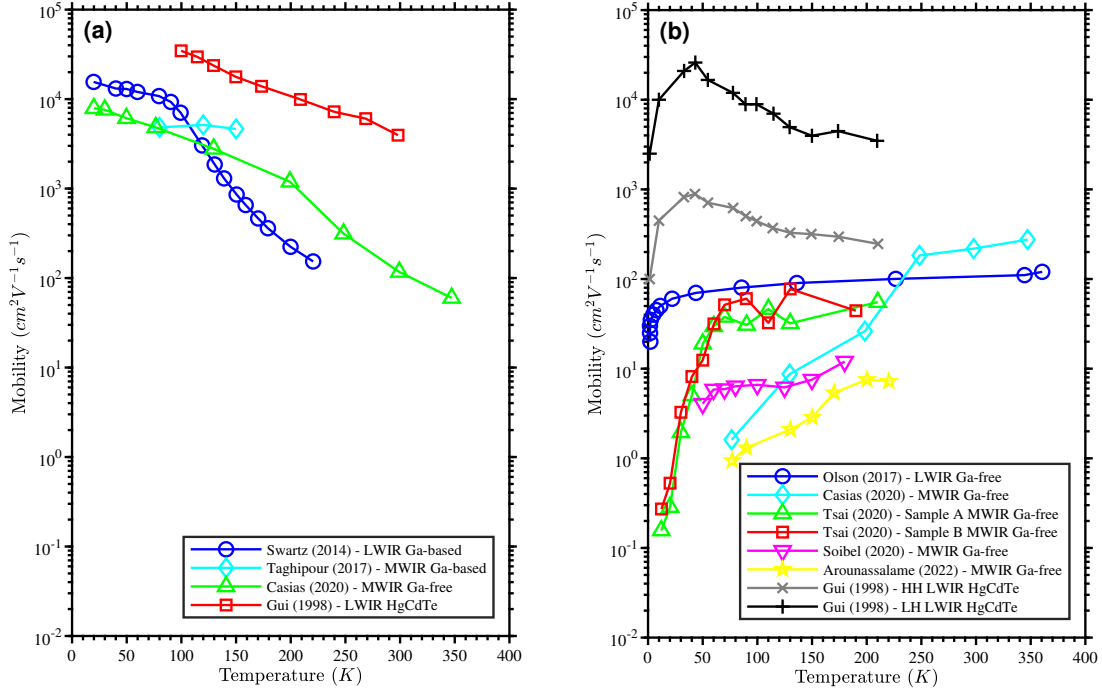


Figure 2.7: The vertical carrier mobility extracted for (a) electrons (Swartz & Myers, 2014; Taghipour et al., 2017; Casias et al., 2020; Gui et al., 1998) and (b) holes (Olson et al., 2017; Casias et al., 2020; Tsai et al., 2020; Soibel et al., 2020; Arounassalame et al., 2022; Gui et al., 1998) from various publications for T2SL structures in the MWIR and LWIR regimes.

The most obvious difference between the mobility data for electrons and holes is the inversion of the temperature dependence. It has been demonstrated that this can arise due to SL disorder resulting in hopping transport between localized states (Bellotti et al., 2021). Consequentially, the magnitude of the mobility for holes can also be several orders of magnitude lower than electrons, particularly at lower temperatures. This suggests that hole transport is more substantially impacted by the structure properties of the T2SL material

and would benefit from studies aimed at optimizing the structure for enhanced hole transport. I will touch upon how high positive asymmetric strain in the SL plane may be a path towards improved hole transport in Chapter 6. While not necessarily demonstrated in the specific data in Fig. 2.7, band structure investigations computing the hole effective mass as a function of cut-off wavelength for Ga-free T2SLs suggest that hole transport should become poorer with increasing cut-off wavelength (Ting et al., 2017). This is due to the fact that LWIR Ga-free T2SLs require relatively thick SL periods to achieve long cut-off wavelengths. This may be counteracted to some degree by having fewer interfaces, and thus less SL disorder. In Chapter 7, I will present a comprehensive investigation aimed at finding Ga-free T2SL structures optimized for enhanced hole transport in the LWIR regime.

Also included in Fig. 2.7 is experimental data on the electron, HH hole, and LH hole mobility for bulk $\text{Hg}_{0.776}\text{Cd}_{0.224}\text{Te}$ for comparison (Gui et al., 1998). The HgCdTe sample exhibits higher electron and hole mobility than the T2SLs, which can be expected for a bulk material compared with a heterostructure in the growth direction. It should be noted that the inversion of the hole mobility in the bulk HgCdTe is likely due to ionized impurity scattering (Gui et al., 1998).

2.3.2.3 *Minority Carrier Lifetime*

In addition to mobility, lifetime is another important parameter impacting carrier collection efficiency in PDs. It determines how long photogenerated carriers will perpetuate before being recombined. As mentioned in Section 2.3.1.2, Ga-free T2SLs have demonstrated significantly longer minority carrier lifetimes compared with Ga-based SLs. Various studies have demonstrated lifetimes on the order of μs while studies on Ga-based T2SLs have placed the minority carrier lifetime on the order of ns (Rogalski et al., 2023). This discrepancy has been purported to be attributed to Ga-based defects or potentially due to the

thicker barriers causing greater carrier confinement in Ga-free SLs (Razeghi & Nguyen, 2014). This suggests an advantage for using Ga-free T2SLs, but as pointed out in Section 2.3.2.1, Ga-free T2SLs tend to have lower absorption coefficients that can offset this advantage. It is also worth noting that HgCdTe have demonstrated minority carrier lifetimes on the order of ms (Rogalski et al., 2023).

In the following dissertation, the focus will be on T2SL structures for use in nBn detectors. Specifically, the results of investigations on both Ga-free and Ga-based MWIR structures for use in nBn detectors, in which the minority carriers are holes, will be presented in Chapter 6. Furthermore, an investigation into optimizing the Ga-free T2SL structures for hole transport in the LWIR regime will be described in Chapter 7. For this, we will use experimental values for the minority hole lifetimes. The results of minority hole lifetimes extracted from Ga-free (Martyniuk et al., 2013) and Ga-based (Soibel et al., 2020; Arounassalame et al., 2022) T2SLs in the MWIR regime and a Ga-free T2SL in the LWIR regime (Olson et al., 2017) are included in Fig. 2.8.

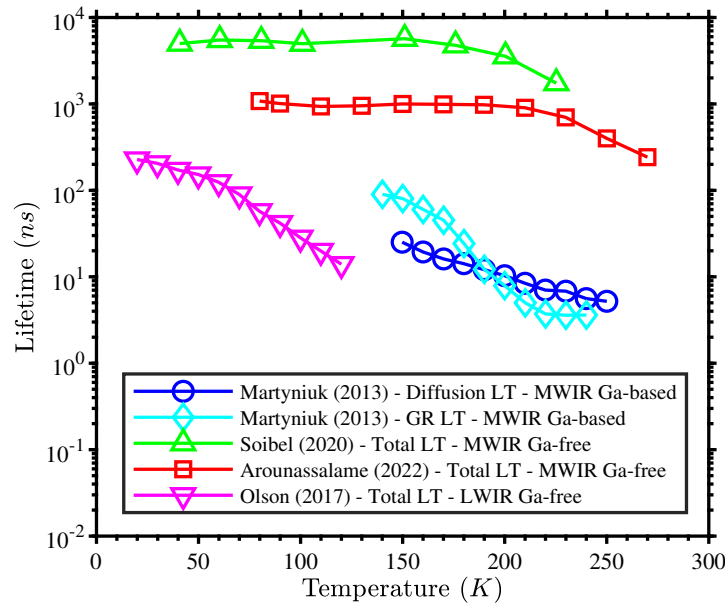


Figure 2.8: The experimental minority hole lifetime extracted for various T2SLs in the MWIR and LWIR regimes.

2.3.3 Quantum Efficiency of T2SL IR Devices

The QE of a PD is the ratio of captured photogenerated carriers to incident photons. Therefore, it is a function of the absorption of photons (generation of photocarriers) and the lifetime and mobility (collection of photocarriers). Devices with high QE are necessary for high performance. I have included experimental QE results from the literature for backside-illuminated nBn detectors with Ga-free and Ga-based SL active regions in the MWIR and for a Ga-free SL in the LWIR regime in Fig. 2.9.

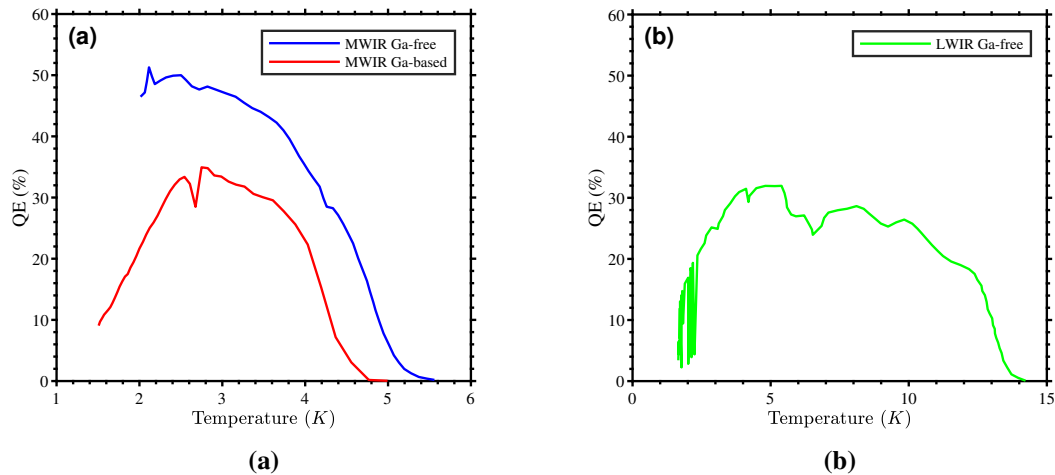


Figure 2.9: The QE extracted for backside-illuminated nBn devices with (a) MWIR Ga-free (Arounassalame et al., 2022) and Ga-based (Bishop et al., 2008) SL active regions. Also included is the QE extracted for an nBn device with a (b) LWIR Ga-free SL active region (Gunapala et al., 2019).

It is worth noting that these results depend not only on the material, but also on the details of the device and environment (thickness of the active region, applied bias, and the temperature). So, a one-to-one comparison is not possible. However, we can examine the results qualitatively. In the MWIR regime the Ga-free nBn PD is capable of achieving higher QE than the Ga-based SL. This is likely due to the longer minority hole lifetimes of Ga-free SLs. Furthermore, the LWIR Ga-free nBn detector suffers from low QE near cutoff com-

pared to the MWIR devices. This is likely due to the low absorption coefficient for Ga-free SLs in the LWIR region. We will consider these results when investigating MWIR Ga-free and Ga-based T2SLs in Chapter 6 and LWIR Ga-free T2SLs in Chapter 7. Chapter 7, in particular, summarizes the results of a study aimed at optimizing the hole mobility in LWIR Ga-free SLs which result in improved QE. It is worth mentioning that the superior transport characteristics and absorption in HgCdTe allow for QE's in excess of 70% (Haran et al., 2019).

CHAPTER 3

Non-equilibrium Green's Functions Formalism

This chapter will introduce an overview of the quantum transport model used throughout this work. For a more comprehensive discussion, the interested reader should turn to Bertazzi et al. (2020); Montoya (2023).

3.1 INTRODUCTION

This chapter will cover the theoretical background underlying the model for carrier transport in this work. As discussed in Chapter 2, vertical carrier mobility is an important component relating to the performance of infrared (IR) sensors. Particularly, it can result in a reduction in the quantum efficiency (QE) of the photodetection elements of a sensor due to a reduction in the carrier capture efficiency. Given that the state-of-the-art type-II superlattice (T2SL) photodetectors (PDs) exhibit lower QE than HgCdTe PDs (see Section 2.3.3), understanding the impact that the superlattice (SL) design and material strain have on the mobility could present a methodology for optimizing sensor performance. However, the extraction of experimental mobility is costly and time consuming, so the field would benefit greatly from a theoretical methodology for predicting the carrier mobility in T2SLs to reduce to the investment necessary for developing optimized prototype structures. Due to the highly nanostructured nature of T2SLs, carrier transport in these materials is complex. Carrier transport in T2SLs is characterized by multiple mechanisms involving the interplay between tunneling and scattering (Tsu & Esaki, 1991; Laikhtman & Miller, 1993). The non-equilibrium Green's functions (NEGF) formalism is fully quantum mechanical in nature, which means that quantum effects like tunneling are treated implicitly. Multiple methods of transport, like hopping and miniband, as well as the transition between them can coexist within the NEGF formalism (Wacker & Jauho, 1998) which means it is well

suited to study vertical transport in T2SLs (Bertazzi et al., 2020).

In this section, I will provide a brief overview of the quantum transport model utilized for studying transport in T2SLs. Section 3.2 will present the non-interacting Hamiltonian model for III-V T2SL materials utilized in this work. Then, Section 3.3 will introduce the Green's functions which are relevant to the NEGF formalism followed by a presentation of the equations of motion of the Green's functions necessary for calculating the steady-state dynamics of the system in Section 3.4. Section 3.5 will present the numerical implementation of NEGF within the system of interest. The form of the scattering interactions that are incorporated into the NEGF formalism through non-local self-energies will be presented in Section 3.6. Finally, the equations necessary for extracting the one-particle properties of the system and subsequently calculating the vertical carrier mobility will be discussed in Section 3.7.

3.2 BAND STRUCTURE MODEL

Before discussing the quantum transport model it will be useful to cover the non-interacting Hamiltonian used to describe the band structure of T2SLs. While band structure models with atomic resolution can be used to describe these structures, the computational complexity of the NEGF methodology precludes the use of these models for relatively large structures. For this reason, we employ a multi-band $k \cdot p$ band structure model, a continuum model, where the small-scale atomic aspects of the matrix-elements are averaged over an element of the discretized basis (Veprek, 2009). This section includes the key equations and important assumptions following the approach presented in Montoya (2023).

It is assumed that the envelope of the wavefunctions in the growth direction of system of interest vary slowly with respect to the atomic structure of the material. In this case, we

can assume that the wavefunction conforms to the following ansatz (Veprek, 2009)¹:

$$\Psi_{\mathbf{k}_t}(\mathbf{r}_t, z) = \frac{1}{\sqrt{A}} e^{i\mathbf{k}_t \cdot \mathbf{r}_t} \sum_n u_n(\mathbf{r}_t, z) F_{n\mathbf{k}}(\mathbf{r}_t), \quad (3.1)$$

where A is the normalization area, \mathbf{k}_t and \mathbf{r}_t are the transverse wavevector and position vector, respectively, z is the position along the growth direction, $u_n(\mathbf{k}_t, \mathbf{r}_t)$ is the zone-center Bloch function for band n , and $F_{n\mathbf{k}}(\mathbf{r})$ are the envelope functions. Therefore, a real-space basis is chosen composed of functions with the following form (Steiger, 2009; Montoya, 2023):

$$\phi_{n,i,\mathbf{k}_t}(\mathbf{r}_t, z) = \frac{1}{\sqrt{A}} e^{i\mathbf{k}_t \cdot \mathbf{r}_t} u_n(\mathbf{r}_t, \mathbf{z}) t_i(z), \quad (3.2)$$

where $t(i)$ is a shape function that is centered at the point z_i over a discrete grid of points in the growth direction. The non-interacting Hamiltonian for an electron in a lattice of atoms with spin orbit coupling can be expressed as:

$$\hat{H}_0(\mathbf{r}) = \frac{1}{2m_0} \hat{p}^2(\mathbf{r}) + \sum_i V(\mathbf{r} - \mathbf{R}_i) + \frac{1}{4M_0^2 c^2} [\nabla V \times \hat{\mathbf{p}}] \cdot \boldsymbol{\sigma}, \quad (3.3)$$

where \hat{p} is the momentum operator, V is the potential due to atoms in the lattice, and $\boldsymbol{\sigma}$ is the Pauli spin matrix. To extract the matrix elements of the Hamiltonian, we can take the inner product of \hat{H}_0 over the basis functions (see Eq.3.2) as such:

$$H_{ij,mn} = \int_V d\mathbf{r} \phi_{m,i,\mathbf{k}_t}^*(\mathbf{r}) \hat{H}_0(\mathbf{r}) \phi_{n,j,\mathbf{k}_t}(\mathbf{r}), \quad (3.4)$$

¹Note: ChatGPT has been used as an aid to generate the LaTeX code for several of the equations from cited sources in this dissertation (OpenAI, 2023). However, it has not been used to generate any new content in this work.

where $\mathbf{r} = (\mathbf{r}_t, z)$. This results in the following expression (Montoya, 2023):

$$H_{ij,mn} = \sum_{\mathbf{k}} \left[\left(E_{n0} + \frac{\hbar^2 k_t^2}{2m_0} \right) \delta_{mn} \int_{l_e} dz t_i(z) t_j(z) + H_{mn}^r \int_{l_e} dz t_i(z) t_j(z) + \frac{\hbar}{m_0} \int_{l_e} dz t_i(z) \mathbf{k} \cdot \mathbf{p}_{mn} t_j(z) + \delta_{mn} \frac{\hbar^2}{2m_0} \int_{l_e} dz \frac{\partial t_i}{\partial z} \frac{\partial t_j}{\partial z} \right], \quad (3.5)$$

where $\mathbf{k} = (\mathbf{k}_t, k_z)$ and $k_z = -i \frac{\partial}{\partial z}$. The following quantities are locally averaged over the unit cell Ω centered at z :

$$H_{mn}^{so}(z) = \frac{1}{\Omega} \int_{\Omega} d\mathbf{r} u_m^*(\mathbf{r}) \frac{1}{4M_0^2 c^2} [\nabla V \times \hat{\mathbf{p}}] \cdot \boldsymbol{\sigma} u_n(\mathbf{r}), \quad (3.6)$$

$$P_{mn}(z) = \frac{1}{\Omega} \int_{\Omega} d\mathbf{r} u_m^*(\mathbf{r}) \hat{p}(r) u_n(\mathbf{r}). \quad (3.7)$$

There were several approximations that were used in the derivation of Eq. 3.5. First, the following quantity is assumed to be insignificant as the crystal momentum $\hbar \mathbf{k}$ is small compared with the particle momentum \mathbf{p} (Montoya, 2023):

$$\int d\mathbf{r} t_i(z) u_m^*(\mathbf{r}) \frac{i\hbar}{4m_0^2 c^2 \sqrt{A}} [\nabla V \times \mathbf{k}] \cdot \boldsymbol{\sigma} e^{i\mathbf{k} \cdot \mathbf{r}} t_j(z) u_n(\mathbf{r}) \approx 0. \quad (3.8)$$

Following this, each remaining term of the Hamiltonian in Eq. 3.4 are subject to lattice-cell averaging of the following form (Montoya, 2023):

$$\int d\mathbf{r} t_i(z) u_m^*(\mathbf{r}) \bar{O} t_j(z) u_n(\mathbf{r}) \approx A \int dz t_i(z) t_j(z) O_{mn}(z), \quad (3.9)$$

and

$$O_{mn}(z) = \frac{1}{\Omega} \int_{\Omega} d\mathbf{r} u_m^*(\mathbf{r}) \bar{O} u_n(\mathbf{r}). \quad (3.10)$$

Then, it is assumed that the potential V within individual elements is approximated as the periodic potential of a bulk homogeneous material, resulting in the following (Montoya, 2023):

$$\frac{1}{\Omega} \int_{\Omega} d\mathbf{r} u_m^*(\mathbf{r}) \left[-\frac{\hbar^2}{2m_0} \nabla^2 + \sum_i V(\mathbf{r} - \mathbf{R}_i) \right] u_n(\mathbf{r}) \approx E_{n0} \delta_{mn}. \quad (3.11)$$

Lastly, the integral in the growth direction was discretized into a sum of integrals over each element, as such (Montoya, 2023):

$$\int dz \rightarrow \sum_e \int_{l_e} dz, \quad (3.12)$$

For a practical implementation of the $\mathbf{k} \cdot \mathbf{p}$ Hamiltonian it is necessary to choose a limited number of bands which are the most relevant to the application under investigation. The effects of the other bands are included perturbatively via Lowdin renormalization (Chuang, 2012). The chosen bands of interest encompass the set A and the remote bands will encompass set B. Then, the effective Hamiltonian matrix elements that account for the remote bands is given as follows (Veprek, 2009; Montoya, 2023):

$$H'_{ij,mn} = H_{ij,mn} + \sum_c \int_{l_c} dz t_i(z) \left[\frac{\hbar^2}{m_0^2} \sum_{b \in B} \frac{(\mathbf{k} \cdot \mathbf{p}_{\mathbf{m},b})(\mathbf{k} \cdot \mathbf{p}_{\mathbf{b},n})}{E_{m0} - E_{b0}} \right] t_j(z). \quad (3.13)$$

This results in matrix elements that are polynomial in \mathbf{k} to second order.

3.2.1 Effective Mass Approximation

One of the band structure models utilized in this work is the effective mass approximation (EMA). It is a single band model, and the matrix elements of the Hamiltonian can be

expressed as follows (Montoya, 2023):

$$H_{i_n, j_n}^{k \cdot p} = \sum_e \left[E_{n0} + \frac{\hbar^2}{2} \sum_{\alpha, \beta=x, y, z} \left(\frac{1}{m^*} \right)_{\alpha, \beta} k_\alpha k_\beta \right] \int_{l_e} dz t_i(z) t_j(z), \quad (3.14)$$

where:

$$\left(\frac{1}{m^*} \right)_{\alpha, \beta} = \frac{1}{m_0} \left(\delta_{\alpha, \beta} + \frac{1}{m_0} \sum_{n' \neq n} \frac{P_{n, n'}^\alpha P_{n', n}^\beta + P_{n, n'}^\beta P_{n', n}^\alpha}{E_{n0} - E_{n'0}} \right). \quad (3.15)$$

3.2.2 Four-band $\mathbf{k} \cdot \mathbf{p}$ Hamiltonian

Recognizing the form of Eq. 3.5 and Eq. 3.13, the bulk $\mathbf{k} \cdot \mathbf{p}$ Hamiltonian including perturbations from the remote bands can be expressed as a polynomial of second order in \mathbf{k} (Veprek, 2009):

$$H_{\text{bulk}}^{k \cdot p}(\mathbf{k}) = \sum_{\alpha, \beta=x, y, z} k_\alpha \bar{H}_{\alpha, \beta}^{(2)} k_\beta + \sum_{\alpha=x, y, z} \bar{H}_\alpha^{(1)} k_\alpha + \bar{H}^{(0)} \quad (3.16)$$

By using the atomic-like basis set as expressed in Liu & Chuang (2002); Qiao et al. (2012) and applying the axial approximation, which enforces axial symmetry of the dispersion in the transverse direction, the 8x8 $\mathbf{k} \cdot \mathbf{p}$ Hamiltonian for zinc-blende can be block-diagonalized and expressed as:

$$H_{\text{bulk}}^{k \cdot p}(\mathbf{k}) = \begin{bmatrix} H_{4 \times 4}^U(\mathbf{k}) & 0 \\ 0 & H_{4 \times 4}^L(\mathbf{k}) \end{bmatrix}, \quad (3.17)$$

with (Liu & Chuang, 2002):

$$H_{4 \times 4}^U = \begin{bmatrix} E_c + A & -3V_p & -V_p + iU & -\sqrt{2}V_p - iU \\ -3V_p & E_c - P - Q & R_p + iS_p & \sqrt{2}R_p - \frac{i}{\sqrt{2}}S_p \\ -V_p - iU & R_p - iS_p & E_c - P + Q & -\sqrt{2}Q + i\sqrt{3}S_p \\ -\sqrt{2}V_p + iU & \sqrt{2}R_p + \frac{i}{\sqrt{2}}S_p & -\sqrt{2}Q - i\sqrt{3}S_p & E_c - P - \Delta \end{bmatrix}, \quad (3.18)$$

$H_{4 \times 4}^L$ can be found by taking the conjugate transpose of $H_{4 \times 4}^U$. Each of the terms defined in Eq. 3.18 are as follows (Liu & Chuang, 2002):

$$\begin{aligned} A &= A_k + A_\varepsilon = \left(\frac{\hbar^2 k^2}{2m_0} \right) (k_x^2 + k_y^2) + a(\varepsilon_x + \varepsilon_y + \varepsilon_z), \\ P &= P_k + P_\varepsilon = \left(\frac{\hbar^2}{2m_0} \right) \gamma_1 (k_x^2 + k_y^2) - a_0(\varepsilon_x + \varepsilon_y + \varepsilon_z), \\ Q &= Q_k + Q_\varepsilon = \left(\frac{\hbar^2}{2m_0} \right) \gamma (k_x^2 - 2k_y^2) + \frac{b}{2}(\varepsilon_x + \varepsilon_y - 2\varepsilon_z), \end{aligned} \quad (3.19)$$

where the O_k terms correspond with the unstrained perturbed matrix element and the O_ε terms correspond with the influence of asymmetric strain in the transverse plane via deformation potentials. Additionally, the other terms are defined as (Liu & Chuang, 2002):

$$\begin{aligned} R_p &= \left(\frac{\hbar^2}{2m_0} \right) \sqrt{3} \left(\frac{\gamma_2 + \gamma_3}{2} \right) k_x^2, \\ S_p &= \left(\frac{\hbar^2}{2m_0} \right) 2\sqrt{3}\gamma_x k_x k_z, \\ V_p &= \frac{1}{\sqrt{6}} P_c k_r, \\ U &= \frac{1}{\sqrt{3}} P_c k_z. \end{aligned} \quad (3.20)$$

For T2SLs in which periodicity is broken in the growth direction, to derive the heterogeneous $k \cdot p$ Hamiltonian, one must start with the bulk Hamiltonian (Eq.3.16) where k_z

must be replaced with the differential operator $-i\frac{\partial}{\partial z}$ and correct operator ordering must be used. The time-independent Schrodinger equation for the nanostructure envelope functions can be expressed as (Montoya, 2023):

$$\begin{aligned} H_{\text{T2SL}}^{k,p}(\mathbf{k})F_{\mathbf{k}_t}(z) &= \left[H^{(0)}(\mathbf{k}_t, z) - i\hbar H_L^{(1)}(\mathbf{k}_t, z) \frac{\partial}{\partial z} - i\hbar \frac{\partial}{\partial z} H_R^{(1)}(\mathbf{k}_t, z) \right. \\ &\quad \left. - \hbar^2 \frac{\partial^2}{\partial z^2} H^{(2)}(\mathbf{k}_t, z) \right] F_{\mathbf{k}_t}(z) \\ &= EF_{\mathbf{k}_t}(z) \end{aligned} \quad (3.21)$$

The envelope functions are approximated using Lagrange polynomials in a finite-element implementation of Galerkins procedure in the weak formulation (Montoya, 2023). Then, multiplying on the left by a test function and integrating over space results in the following generalized eigenvalue problem (Zhou et al., 2014; Montoya, 2023):

$$\sum_j H_{i,j}^{k,p}(\mathbf{k})F_j(\mathbf{k}_t) = E \sum_i \int dz t_i(z) t_j(z) F_j(\mathbf{k}_t) \quad (3.22)$$

where the final Hamiltonian used for heterogeneous structures $H_{i,j}^{k,p}(\mathbf{k})$ in the growth z direction is expressed as (Montoya, 2023):

$$\begin{aligned} H_{i,j}^{k,p}(\mathbf{k}) &= \sum_e \left[\int_{l_e} dz t_i(z) H^{(0)}(\mathbf{k}, z) t_j(z) - i \int_{l_e} dz t_i(z) H_L^{(1)}(\mathbf{k}, z) \frac{\partial t_j}{\partial z} \right. \\ &\quad \left. - i \int_{l_e} dz \frac{\partial t_i}{\partial z} H_R^{(1)}(\mathbf{k}, z) t_j(z) + \int_{l_e} dz \frac{\partial t_i}{\partial z} H^{(2)}(z) \frac{\partial t_j}{\partial z} \right], \end{aligned} \quad (3.23)$$

Note that for the first order bulk terms in $H_{i,j}^{k,p}(\mathbf{k})$ it is important that the correct form of operator ordering is used to avoid spurious solutions (Veprek et al., 2007; Veprek, 2009). This is achieved by applying Foreman operator ordering (Foreman, 1997) to Eq. 3.18 as

described in Section 5.4.13 of Cambri (2017).

3.3 NON-EQUILIBRIUM GREEN'S FUNCTIONS

The fundamental theory behind the quantum transport model that was used to simulate carrier transport in this work is presented in this section. The system under investigation is composed of many particles under the influence of various complex interactions. It is segregated into a device region, in which the various scattering mechanisms take action, and contacts, which act as carrier reservoirs under thermal equilibrium. The simulation of quantum system dynamics starts with the time-dependent Schrodinger's equation (TDSE) for an isolated system:

$$i\hbar \frac{d}{dt} |\Psi(t)\rangle = H(t) |\Psi(t)\rangle \quad (3.24)$$

where the state of the system as a function of time is described by $|\Psi(t)\rangle$ and $H(t)$ is the Hamiltonian governing the system behavior. In the case of a time-independent Hamiltonian, the solution to the TDSE is given as follows:

$$|\Psi(t)\rangle = e^{-\frac{i}{\hbar} H(t-t_0)} |\Psi(t_0)\rangle \quad (3.25)$$

However, for a general system, the Hamiltonian cannot be expected to be time-independent. The general solution to the TDSE for a time-dependent Hamiltonian is as follows (Stefanucci & Van Leeuwen, 2013):

$$|\Psi(t)\rangle = \hat{U}(t, t_0) |\Psi(t_0)\rangle, \quad (3.26)$$

where the evolution operator $\hat{U}(t, t_0)$ is defined as (Stefanucci & Van Leeuwen, 2013):

$$U(t_2, t_1) = \begin{cases} \mathcal{T} \exp \left(-\frac{i}{\hbar} \int_{t_1}^{t_2} dt' \hat{H}(t') \right), & t_2 > t_1, \\ \overline{\mathcal{T}} \exp \left(+\frac{i}{\hbar} \int_{t_2}^{t_1} dt' \hat{H}(t') \right), & t_2 < t_1. \end{cases} \quad (3.27)$$

\mathcal{T} and $\overline{\mathcal{T}}$ are the chronological and anti-chronological ordering operator.

The time-dependent quantum average of an observable governed by Schrodinger's equation can then be expressed via the following equation (Stefanucci & Van Leeuwen, 2013):

$$O(t) = \langle \Psi(0) | \hat{O}(t) | \Psi(0) \rangle = \langle \Psi_0 | \hat{U}^\dagger(t, 0) \hat{O} \hat{U}(t, 0) | \Psi_0 \rangle, \quad (3.28)$$

The quantity $O(t)$ can be described as the overlap between the initial state of the system $|\Psi(t)\rangle$ and one in which there is an evolution of the initial state $|\Psi(t)\rangle$ from t_0 to t , and execution of the operator at t , and then an evolution of the state back to t_0 (Stefanucci & Van Leeuwen, 2013). Taking into account the definition of the time-evolution operators, it is possible to rewrite this equation as the following:

$$O(t) = \langle \Psi_0 | \mathbf{T} e^{-i \int_{t_0}^t dt' \mathbf{H}(t')} \hat{O} \mathbf{T} e^{-i \int_{t_0}^t dt' \mathbf{H}(t')} | \Psi_0 \rangle \quad (3.29)$$

By defining a contour in the complex time plane (see Fig. 3.1), Eq. 3.29 becomes:

$$O(t) = \langle \Psi_0 | \mathbf{T} e^{-i \int_c d\bar{z} \mathbf{H}(\bar{z})} \hat{O}(t) | \Psi_0 \rangle \quad (3.30)$$

where \bar{z} is an index on the Schwinger-Keldysh contour (not to be confused with the growth direction coordinate z), \mathbf{T} is the contour ordering operator.

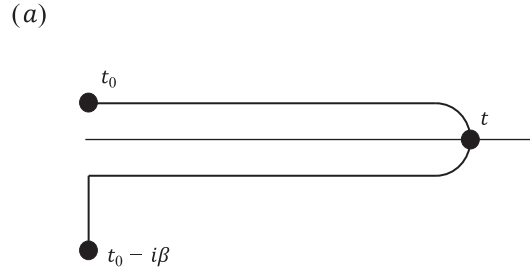


Figure 3.1: The Konstantinov-Perel contour for the exact solution to the Green's function as presented in (Stefanucci & Van Leeuwen, 2013). The offset from the time axis is for illustration purposes only.

This provides us with notation that will be useful in the case of Green's functions.

When a system is coupled to the environment, it is no longer in a pure state. In this case, it becomes convenient to speak instead in terms of ensemble-averages. In coupling an isolated system to the environment, the interaction can be accounted for through a probability distribution (Stefanucci & Van Leeuwen, 2013). The ensemble-average of an operator can be thought of as the weighted sum of expectation values for many identical systems coupled to the environment, taking into account the probability distribution (Stefanucci & Van Leeuwen, 2013). The ensemble-average of an operator can be expressed as follows (Stefanucci & Van Leeuwen, 2013):

$$O(t) = \frac{\text{Tr} \left(\mathcal{T} e^{-i \int_0^t dt' \hat{H}(t')} \hat{O}(t) \right)}{\text{Tr} \left(\mathcal{T} e^{-i \int_0^t dt' \hat{H}(t')} \right)} \quad (3.31)$$

where the integration is over the contour which is exact and is displayed in Fig. 3.1. The Hamiltonian is also specified over the contour in which H_m is over portion of the contour in imaginary time and H is over the portion of the contour in real time. The inclusion of H_m is related to the initial correlations prior to switch-on of the perturbing Hamiltonian which is not pertinent to this work in which we only investigate steady-state dynamics.

An approximation that can be made on the exact contour is the adiabatic approximation, in which it is assumed that the interacting density matrix can be evolved from the non-interacting density matrix via adiabatic switch-on of the interaction (Stefanucci & Van Leeuwen, 2013). In this case, the contour over which the integration occurs is presented in Fig. 3.2a.

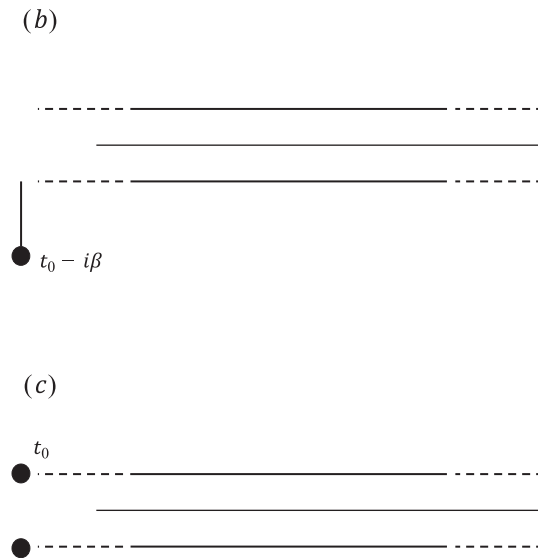


Figure 3.2: The Keldysh contour for the solution to the Green's function in the adiabatic approximation as presented in (Stefanucci & Van Leeuwen, 2013), with (a) and without (b) initial correlations. The offset from the time axis is for illustration purposes only.

Given that we are interested in steady-state behavior exclusively, we do not care about initial correlations. Thus, the final contour over which the steady-state ensemble-average of an operator is presented in Fig. 3.2b.

The general definition of the Greens function of n-order $G^{(n)}(1; 1'; \dots; n; n')$ is the ensemble average of n pairs of contour-ordered field operators $\Psi(1)\Psi^\dagger(1')$ in the Heisenberg

picture (Stefanucci & Van Leeuwen, 2013):

$$G^{(n)}(1; 1'; \dots; n; n') = -\frac{i^n}{\hbar^n} \langle \mathcal{T} \Psi_{\mathcal{H}}(1) \dots \Psi_{\mathcal{H}}(n) \Psi_{\mathcal{H}}^\dagger(n') \dots \Psi_{\mathcal{H}}^\dagger(1') \rangle \quad (3.32)$$

where a compound argument notation has been used in which $n = \mathbf{r}, t$ and $n' = \mathbf{r}', t'$. The Greens function can also be shown to be equal to (Montoya, 2023):

$$G^{(n)}(1; 1'; \dots; n; n') = \frac{1}{i^n} \frac{\text{Tr} [\mathcal{T} \exp -i \int_c d\bar{z} \hat{H}(\bar{z}) \hat{\Psi}(1) \dots \hat{\Psi}(n) \hat{\Psi}^\dagger(n') \dots \hat{\Psi}^\dagger(1')]}{\text{Tr} [\mathcal{T} \exp -i \int_c d\bar{z} \hat{H}(\bar{z})]}, \quad (3.33)$$

where for our interest in steady-state behavior the integration is over the contour c displayed in Fig. 3.2b. The Green's function on the contour contains the steady-state properties of interest to this work. The next section will focus on the equations of motion for the Green's functions eventually leading to the presentation of the Dyson and Keldysh equation for calculating the real-time Green's functions.

3.4 EQUATIONS OF MOTION OF THE GREEN'S FUNCTIONS

To calculate the Greens functions, it is necessary to solve for the equations of motion with respect to the time arguments on the contour. I will briefly introduce the type of Hamiltonian that will be used to derive the equations of motion of the Greens functions. It includes the fully solvable component H_0 that describes the effect of the lattice and the electrostatics as well as a part containing the particle interactions H_i , both of which are time-independent. Additionally, there is a time-dependent component responsible for driving the system out of equilibrium which is included via a perturbative term $H_{\text{ext}}(t)$. Thus, the full Hamiltonian will be of the form:

$$\hat{H}(t) = \hat{H}_0 + \hat{H}_i + \hat{H}_{\text{ext}}(t). \quad (3.34)$$

The complete Hamiltonian can be expressed in second-quantization as follows (Montoya, 2023):

$$\begin{aligned} \hat{H}(t) = & \int d\mathbf{r} \hat{\Psi}^\dagger(\mathbf{r}, t) [\hat{H}_0(\mathbf{r}) + U(\mathbf{r}, t)] \hat{\Psi}(\mathbf{r}, t) \\ & + \frac{1}{2} \int d\mathbf{r} \int d\mathbf{r}' \hat{\Psi}^\dagger(\mathbf{r}, t) \hat{\Psi}^\dagger(\mathbf{r}', t) V(\mathbf{r} - \mathbf{r}') \hat{\Psi}(\mathbf{r}', t) \hat{\Psi}(\mathbf{r}, t), \end{aligned} \quad (3.35)$$

where the potential V describes the carrier-carrier interactions and U a single-particle perturbing potential. From here, the equations of motion for the field operator $\hat{\Psi}_\mu(\mathbf{r}, t)$ can be derived (Montoya, 2023):

$$\begin{aligned} i\hbar \frac{\partial}{\partial t} \hat{\Psi}_\mu(\mathbf{r}, t) = & [\hat{H}_0(\mathbf{r}) + U(\mathbf{r}, t)] \hat{\Psi}_\mu(\mathbf{r}, t) \\ & + \int d\mathbf{r}' V(\mathbf{r} - \mathbf{r}') \hat{\Psi}_\mu^\dagger(\mathbf{r}', t) \hat{\Psi}_\mu(\mathbf{r}', t) \hat{\Psi}_\mu(\mathbf{r}, t). \end{aligned} \quad (3.36)$$

The equation of motion for $\hat{\Psi}_\mu^\dagger(\mathbf{r}, t)$ is found by taking the adjoint of Eq. 3.36 (Stefanucci & Van Leeuwen, 2013):

$$\begin{aligned} i\hbar \frac{\partial}{\partial t} \hat{\Psi}_\mu^\dagger(\mathbf{r}, t) = & - \hat{\Psi}_\mu^\dagger(\mathbf{r}', t) \left[\overleftarrow{\hat{H}}_0(\mathbf{r}) + \overleftarrow{U}(\mathbf{r}, t) \right] \\ & - \int d\mathbf{r}' V(\mathbf{r} - \mathbf{r}') \hat{\Psi}_\mu^\dagger(\mathbf{r}, t) \hat{\Psi}_\mu^\dagger(\mathbf{r}', t) \hat{\Psi}_\mu(\mathbf{r}', t), \end{aligned} \quad (3.37)$$

where the arrow above an operator \overleftarrow{O} implies that it is applied to the field operator term on the left. The derivation for the equations of motion of the Greens function of general order, given Eq. 3.32, follows from this result and can be expression as (Stefanucci & Van Leeuwen, 2013):

$$\left[i \frac{d}{dz_k} - h(k) \right] \hat{G}_n(1, \dots, n; 1', \dots, n')$$

$$\begin{aligned}
&= \pm i \int d\bar{1} v(k; \bar{1}) \hat{G}_{n+1}(1, \dots, n, \bar{1}; 1', \dots, n', \bar{1}^+) \\
&\quad + \sum_{j=1}^n (\pm)^{k+j} \delta(k; j) \hat{G}_{n-1}(1, \dots, k, \dots, n; 1', \dots, j', \dots, n'), \quad (3.38)
\end{aligned}$$

$$\begin{aligned}
&\hat{G}_n(1, \dots, n; 1', \dots, n') \left[-i \frac{\overleftarrow{d}}{dz'_k} - h(k') \right] \\
&= \pm i \int d\bar{1} v(k'; \bar{1}) \hat{G}_{n+1}(1, \dots, n, \bar{1}^-; 1', \dots, n', \bar{1}) \\
&\quad + \sum_{j=1}^n (\pm)^{k'+j} \delta(k'; j) \hat{G}_{n-1}(1, \dots, k', \dots, n; 1', \dots, j', \dots, n'). \quad (3.39)
\end{aligned}$$

This equation is known as the Martin-Schwinger hierarchy, and it is valid for each of the contours suggested in Fig. 3.1 and Fig. 3.2 (Stefanucci & Van Leeuwen, 2013). For the properties pertinent to this work, the one-particle Greens function is the most relevant. The equations of motion of the one-particle Greens function can be extracted from Eq. 3.38 and Eq. 3.39 resulting in (Montoya, 2023):

$$\left[i\hbar \frac{\partial}{\partial t_1} - \hat{H}_0(\mathbf{r}_1) - U(1) \right] G(1'1) = \delta(1'1) - i\hbar \int_C d2V(1-2)G^{(2)}(121'2^+), \quad (3.40)$$

$$\left[-i\hbar \frac{\partial}{\partial t_{1'}} - \hat{H}_0(\mathbf{r}_{1'}) - U(1') \right] G(1'1) = \delta(1'1) - i\hbar \int_C d2V(1'-2)G^{(2)}(12^-1'2). \quad (3.41)$$

Where $G^{(2)}$ is the two-particle Greens function. From Eq 3.38 and Eq 3.39 it is clear that to solve for $G^{(2)}$, you need $G^{(3)}$, and so on. This continues in an infinite hierarchy, prohibiting a direct solution to the equations of motion for G . To move forward, Eq. 3.40 and Eq. 3.41 can be rewritten as (Montoya, 2023):

$$\left[i\hbar \frac{\partial}{\partial t_1} - \hat{H}_0(r_1) - U(t_1) \right] G(1'1) = \delta(1'1) + \int_C d3\Sigma(13)G(3'1'), \quad (3.42)$$

$$\left[-i\hbar \frac{\partial}{\partial t_{1'}} - \hat{H}_0(r_{1'}) - U(t_{1'}) \right] G(1'1) = \delta(1'1) + \int_C d^3G(13)\Sigma(3'1'), \quad (3.43)$$

where Σ encodes the entire effect of the particle interactions onto the one-particle dynamics. The non-interacting Green's function can be expressed as (Stefanucci & Van Leeuwen, 2013):

$$\left[i\hbar \frac{d}{dz_1} - h(1) \right] G_0(1;1') = \delta(1;1'), \quad (3.44)$$

$$G_0(1;1') \left[-i\hbar \frac{d}{dz_{1'}} - h(1') \right] = \delta(1;1'). \quad (3.45)$$

The final form of the equations of motion for the one-particle Green's function are the Dyson's equations (Stefanucci & Van Leeuwen, 2013):

$$G(1;2) = G_0(1;2) + \int d^3d^4 G_0(1;3)\Sigma(3;4)G(4;2), \quad (3.46)$$

$$G(1';2) = G_0(1';2) + \int d^3d^4 G(1';3)\Sigma(3;4)G_0(4;2). \quad (3.47)$$

This is the formal solution for the one-particle Green's function in which, in the exact solution, the self-energy Σ depends in a complex way on the Green's function (Stefanucci & Van Leeuwen, 2013). However, the integral over the contour presents a complication. To resolve this, several new real-time GFs can be introduced as analytic continuations of G (Stefanucci & Van Leeuwen, 2013):

$$G(1'1) = \begin{cases} G^<(1'1) & t_1, t'_1 \in C_t, \\ G^>(1'1) & t_1, t'_1 \in C_{t'}, \\ G^{\bar{}}(1'1) & t_1 \in C_t, t'_1 \in C_{t'}, \\ G^{\bar{}}(1'1) & t_1 \in C_{t'}, t'_1 \in C_t, \end{cases} \quad (3.48)$$

which are referred to as the chronological, anti-chronological, lesser, and greater Green's functions, respectively. The contour over which they correspond is the one in Fig. 3.2b. The expressions for each of these quantities are as follows (Stefanucci & Van Leeuwen, 2013):

$$\begin{aligned}
G^<(1'1) &= -\frac{i}{\hbar} \langle \mathcal{T}_C \hat{\Psi}(1') \hat{\Psi}^\dagger(1) \rangle \\
G^>(1'1) &= -\frac{i}{\hbar} \langle \mathcal{T}_C \hat{\Psi}(1) \hat{\Psi}^\dagger(1') \rangle \\
G^\parallel(1'1) &= \pm \frac{i}{\hbar} \langle \hat{\Psi}^\dagger(1') \hat{\Psi}(1) \rangle \\
G^>(1'1) &= -\frac{i}{\hbar} \langle \hat{\Psi}(1) \hat{\Psi}^\dagger(1') \rangle
\end{aligned} \tag{3.49}$$

When solving NEGF problems, it is typical to use the retarded and advanced Green's functions in place of the chronological and anti-chronological ones. These are defined via (Stefanucci & Van Leeuwen, 2013):

$$G^R(1, 1') = \theta(t_1 - t_{1'}) [G^>(1, 1') - G^<(1, 1')] = G^A(1', 1)^\dagger \tag{3.50}$$

The equations of motion for the real-time Green's functions presented above are derived according to the Langreth rules. The derivation is skipped here, but can be found in Montoya (2023) for the interested reader. The resulting Dyson's and Keldysh equations for the retarded (advanced) and lesser(greater) Green's functions, respectively, are provided below (Montoya, 2023):

$$G^R(1'1) = G_0^R(1'1) + \int d2 \int d3 G_0^R(1'2) \Sigma^R(2'3) G^R(3'1), \tag{3.51}$$

$$G^{\lessgtr}(1'1) = \int d2 \int d3 G^R(1'2) \Sigma^{\lessgtr}(2'3) G^A(3'1). \tag{3.52}$$

The real-time Green's functions contain the full information of the steady-state dynamics of one-particle properties in the system in question. To solve them one needs to know the form of the real-time self-energy terms for a given interaction. In Section 3.6, I will provide the equations for the real-time self-energy expressions for several particle-particle interactions that will be pertinent to this work as derived according to the self-consistent Born approximation (SCBA).

A final note of import is that given that we are interested only in the steady-state properties of the system, we can further simplify the calculation of Eq. 3.51 and Eq. 3.52. In steady-state, the values of t_1 and t_2 are not important, but rather the time difference between them $\tau = t_2 - t_1$. It is then possible to take the Fourier transport of the Green's functions, as such (Montoya, 2023):

$$\tilde{G}(r, r'; E) = \int_{-\infty}^{\infty} d\tau e^{iE\tau} G^R(r, r'; \tau) \quad (3.53)$$

resulting in Green's functions that depend only upon one energy argument, rather than two time ones. The Dyson and Keldysh equations for the real-time Green's functions in energy space are then given as follows (Montoya, 2023):

$$G^{R/A}(r, r'; E) = G_0^{R/A}(r, r'; E) + \int dr_1 \int dr_2 G_0^{R/A}(r, r_1; E) \Sigma^{R/A}(r_1, r_2; E) G^{R/A}(r_2, r'; E), \quad (3.54)$$

$$G^{\lessgtr}(r, r'; E) = \int dr_1 \int dr_2 G^R(r, r_1; E) \Sigma^{\lessgtr}(r_1, r_2; E) G^A(r_2, r'; E). \quad (3.55)$$

3.5 NUMERICAL IMPLEMENTATION OF NON-EQUILIBRIUM GREEN'S FUNCTIONS

In this section, I will briefly describe the numerical implementation and boundary conditions necessary for simulating carrier transport in T2SLs.

3.5.1 Spatial Discretization of Dyson and Keldysh Equations

The discretization of the quantum transport model was presented in greater detail in Montoya (2023), but the main expressions and assumptions are reproduced in this section. Starting from the definition of the Green's function, discretization can be achieved by first expanding the field operators in the real-space basis expressed in Eq. 3.2 (Montoya, 2023):

$$\hat{\Psi}_H(r, t) = \sum_{\mathbf{v}} \phi_{\mathbf{v}}(r) \hat{c}_{\mathbf{v}}(t) \quad (3.56)$$

$$\hat{\Psi}_H^\dagger(r, t) = \sum_{\mathbf{v}} \phi_{\mathbf{v}}^*(r) \hat{c}_{\mathbf{v}}^\dagger(t) \quad (3.57)$$

Next, plugging this in to the definition of the single-particle Green's function which is obtained from Eq. 3.32, the discretized Green's function over space is expressed as (Montoya, 2023):

$$\begin{aligned} G(r, t; r', t') &= -\frac{i}{\hbar} \langle \mathcal{T} \hat{\Psi}_H(r, t) \hat{\Psi}_H^\dagger(r', t') \rangle \\ &= -\frac{i}{\hbar} \langle \mathcal{T} \left(\sum_{\mathbf{v}} \phi_{\mathbf{v}}(r) \hat{c}_{\mathbf{v}}(t) \right) \left(\sum_{\mu} \phi_{\mu}^*(r') \hat{c}_{\mu}^\dagger(t') \right) \rangle \\ &= \sum_{\mathbf{v}\mu} \phi_{\mathbf{v}}(r) \left(-\frac{i}{\hbar} \langle \mathcal{T} \hat{c}_{\mathbf{v}}(t) \hat{c}_{\mu}^\dagger(t') \rangle \right) \phi_{\mu}^*(r') \\ &= \sum_{\mathbf{v}\mu} \phi_{\mathbf{v}}(r) G_{\mathbf{v}\mu}(t, t') \phi_{\mu}^*(r'), \end{aligned} \quad (3.58)$$

In energy space, this expression becomes:

$$G(r, r'; E) = \sum_{\nu\mu} \phi_\nu(r) G_{\nu\mu}(E) \phi_\mu^*(r'). \quad (3.59)$$

The matrix form of the Dyson and Keldysh equations can thus be written as follows (Montoya, 2023):

$$G^R(E) = G_0^R(E) + G_0^R(E) \Sigma^R(E) G^R(E), \quad (3.60)$$

$$G^<(E) = G^R(E) \Sigma^<(E) G^A(E). \quad (3.61)$$

where the Greens functions are all expressed in contravariant form:

$$G(r, r'; E) = \sum_{\nu\mu} \phi_\nu(r) G_{\nu\mu}(E) \phi_\mu^*(r'), \quad (3.62)$$

and the self-energy is expressed in covariant form:

$$\tilde{G}_{\nu\mu}(E) = \int dr \int dr' \phi_\nu^*(r) G(r, r'; E) \phi_\mu(r'). \quad (3.63)$$

The non-interacting Green's function of Eq. 3.60 is expressed as follows (Montoya, 2023):

$$G_0^R(E) = [(E + i\eta)M - H - U]^{-1}, \quad (3.64)$$

where:

$$\begin{aligned} H_{\mu\nu} &= \int dr \phi_\nu^*(r) \hat{H}_0(r) \phi_\mu(r), \\ U_{\mu\nu} &= \int dr \phi_\nu^*(r) U(r) \phi_\mu(r), \\ M_{\mu\nu} &= \int dr \phi_\nu^*(r) \phi_\mu(r). \end{aligned} \quad (3.65)$$

Note that the overlap matrix M has been introduced with the form (Steiger, 2009) provided in Eq. 3.65.

where the coarse-graining assumption of $k \cdot p$ was used which assumes that the envelope functions vary slowly over a unit cell. Also, $\eta \rightarrow 0^+$ which is necessary for the Green's function to have the correct properties (Stefanucci & Van Leeuwen, 2013). Ultimately, Eq. 3.60 and Eq. 3.61 are ultimately the two equations that are solved in the NEGF calculations in this work.

3.5.2 Implementation of Open Boundary Conditions

A more comprehensive derivation of the open boundary condition implementation is provided in Montoya (2023). However, the key equations and assumptions are summarized in this section. Up to this point, the equations that have been developed to study quantum transport in T2SLs only encompass the isolated device. To study the conduction of carriers through a region of T2SL material, the system is coupled to semi-infinite contacts on both ends of the simulation domain. This allows for carrier injection into, and collection from, the device region of the simulation. The strategy used for introducing semi-infinite contacts to the device domain is to fold the influence of them into a self-energy term that will be included in Eq. 3.60 and Eq. 3.61. This will be in addition to the self-energy terms associated with particle-particle interactions. The full derivation for the pertinent equations in this section is given in Montoya (2023). However, this section will provide the most important expressions.

The derivation begins by starting with the Dyson's equation for a system with three coupled sections (device and contacts) (Montoya, 2023):

$$\begin{bmatrix} \hat{\mathcal{H}}_{L,D} & \hat{\mathcal{H}}_{L,DL} & 0 \\ \hat{\mathcal{H}}_{DL} & \hat{\mathcal{H}}_D & \hat{\mathcal{H}}_{DR} \\ 0 & \hat{\mathcal{H}}_{RD} & \hat{\mathcal{H}}_R \end{bmatrix} \begin{bmatrix} G_L^R & G_{LD}^R & G_{LR}^R \\ G_{DL}^R & G_D^R & G_{DR}^R \\ G_{RL}^R & G_{RD}^R & G_R^R \end{bmatrix} = \begin{bmatrix} 1 & 0 & 0 \\ 0 & 1 & 0 \\ 0 & 0 & 1 \end{bmatrix} \quad (3.66)$$

where $\hat{\mathcal{H}}$ terms have the following form:

$$\hat{\mathcal{H}} = ES - H - \Sigma \quad (3.67)$$

Eq. 3.66 can be solved for the case of a nearest-neighbor Hamiltonian where only the boundary terms are non-zero resulting in the boundary self-energy expressions (Montoya, 2023):

$$\begin{aligned} \Sigma_{1,1}^{RB} &= \left\{ \tilde{H}_{DL}^{1,0} \right\} [g_{0,0}^R] \left\{ \tilde{H}_{DL}^{0,1} \right\} \\ \Sigma_{N,N}^{RB} &= \left\{ \tilde{H}_{DR}^{N,N+1} \right\} [g_{N+1,N+1}^R] \left\{ \tilde{H}_{DR}^{N+1,N} \right\} \\ \Sigma_{1,1}^{SB} &= \left\{ \tilde{H}_{DL}^{1,0} \right\} [g_{0,0}^S] \left\{ \tilde{H}_{DL}^{0,1} \right\} \\ \Sigma_{N,N}^{SB} &= \left\{ \tilde{H}_{DR}^{N,N+1} \right\} [g_{N+1,N+1}^S] \left\{ \tilde{H}_{DR}^{N+1,N} \right\} \end{aligned} \quad (3.68)$$

where

$$g_L^R = \tilde{H}_L^{-1} = [ES_L - H_L - \Sigma_L]^{-1}, \quad (3.69)$$

$$g_R^R = \tilde{H}_R^{-1} = [ES_R - H_R - \Sigma_R]^{-1}. \quad (3.70)$$

The retarded boundary self-energy terms are calculated via a method that matches the boundary terms of the envelope function which can be accomplished in the single (Polizzi & Datta, 2003) and multi-band (Piprek, 2017) cases. The final expressions for the left and right contacts are (Montoya, 2023):

$$\begin{aligned} \Sigma_{1,1}^{RB}(k, E) &= -iH^{(2)}(z_1)\chi^L K^L [\chi^L]^{-1} + iH^R(k, z_1), \\ \Sigma_{N,N}^{RB}(k, E) &= -iH^{(2)}(z_N)\chi^R K^R [\chi^R]^{-1} + iH^R(k, z_N), \end{aligned} \quad (3.71)$$

where χ and K are the row vectors of eigenfunctions of the bulk Hamiltonian associated

with outgoing waves and the diagonal matrix of the corresponding longitudinal wavevector, respectively. They are expressed as follows (Montoya, 2023):

$$\boldsymbol{\chi}^{L(R)} = [\boldsymbol{\chi}_1^{L(R)}, \dots, \boldsymbol{\chi}_{N_b}^{L(R)}] \quad (3.72)$$

$$K_z^{L(R)} = \begin{pmatrix} k_z^{L(R),1} & 0 & \dots & 0 \\ 0 & k_z^{L(R),2} & \dots & 0 \\ \vdots & \vdots & \ddots & \vdots \\ 0 & 0 & \dots & k_z^{L(R),N_b} \end{pmatrix}, \quad (3.73)$$

Finally, the lesser (greater) boundary self-energies can be calculated by assuming bulk-like behavior of the contact material at equilibrium via (Montoya, 2023):

$$\begin{aligned} \Sigma_{1,1}^B &= -f_{FD}(E - \mu_L)(\Sigma_{1,1}^{RB} - \Sigma_{1,1}^{AB}), \\ \Sigma_{N,N}^B &= -f_{FD}(E - \mu_R)(\Sigma_{N,N}^{RB} - \Sigma_{N,N}^{AB}), \end{aligned} \quad (3.74)$$

$$\begin{aligned} \Sigma_{1,1}^B &= [1 - f_{FD}(E - \mu_L)](\Sigma_{1,1}^{RB} - \Sigma_{1,1}^{AB}), \\ \Sigma_{N,N}^B &= [1 - f_{FD}(E - \mu_R)](\Sigma_{N,N}^{RB} - \Sigma_{N,N}^{AB}), \end{aligned} \quad (3.75)$$

The main assumption of this section is that the contacts can be treated as semi-infinite bulk material at equilibrium.

3.5.3 Mode-Space Methodology

A more comprehensive explanation for the mode space methodology can be found in Bertazzi et al. (2020). However, the main points are reproduced in this section. The self-consistent loop of the SCBA is computationally inefficient for devices with a relatively large number of spatial nodes. Therefore, while the final calculation of the Dyson and

Keldysh equations is performed in real space (Eq. 3.60 and Eq. 3.61), the inner loop of the SCBA is performed in a problem-matched, mode space basis. The approach starts with the generalized eigenvalue problem for solving Schrodinger's equation in the finite-element basis (Bertazzi et al., 2020):

$$H_0\Psi_l = E_M\Psi_l \quad (3.76)$$

where the expression is written in matrix form. This equation is then transformed by means of Lowdin symmetric orthogonalization to a standard eigenvalue problem as follows (Bertazzi et al., 2020):

$$M^{-1/2}H_0M^{-1/2}\Psi_l = E_l\Psi_l \quad (3.77)$$

The solutions are separated into two different sets: near and remote. The sets are categorized according to the proximity in energy to the center of the energy range being investigated. To accommodate the calculation of the self energy, it is pertinent to have an orthogonalized basis set in real space. This is done by diagonalizing the position operator in the near and remote basis resulting in maximally localized basis functions (Zeng et al., 2013; Bertazzi et al., 2020):

$$\tilde{Z}_{\alpha_i}\Psi_{\alpha_i}^{ML} = z_{\alpha_i}\Psi_{\alpha_i}^{ML}, \quad (3.78)$$

with

$$\tilde{Z}_{\alpha} = T \dagger_{\alpha} M^{-1/2} Z M^{-1/2} T_{\alpha}, \quad (3.79)$$

where Z is the position operator in the finite-element basis. The transformation matrix T_{α} has columns for the near ($\alpha = n$) and remote ($\alpha = r$) modes. Then with $P_{\alpha} = \{\Psi_{\alpha_1}^{ML} \dots \Psi_{\alpha_n}^{ML}\}^T$ an additional transformation matrix $P = \{P_n, P_r\}$ is defined, and the Dyson and Keldysh equations (Eq. 3.60 and Eq. 3.61) can be expressed in this new mode

space (Bertazzi et al., 2020):

$$\tilde{G}^R(E) = \tilde{G}_0^R(E) + \tilde{G}_0^R(E)\tilde{\Sigma}^R(E)\tilde{G}^R(E), \quad (3.80)$$

$$\tilde{G}^{\leq}(E) = \tilde{G}^R(E)\tilde{\Sigma}^{\leq}(E)\tilde{G}^A(E). \quad (3.81)$$

with the Green's functions and self-energies of the form:

$$\begin{aligned} \tilde{G} &= P^\dagger T^\dagger M^{-1/2} Z M^{-1/2} T P \\ \tilde{\Sigma} &= P^\dagger T^\dagger M^{1/2} \Sigma M^{1/2} T P. \end{aligned} \quad (3.82)$$

The effect of the remote bands on the system are included via additional self-energy terms (Bertazzi et al., 2020):

$$\tilde{\Sigma}_{nn}^R = \tilde{A}_{nr} \tilde{g}_{rr}^R \tilde{A}_{rn} \quad (3.83)$$

$$\tilde{\Sigma}_{nn}^< = -\tilde{\Sigma}_{nr}^< \tilde{g}_{rr}^A \tilde{A}_{rn}^* - \tilde{A}_{nr} \tilde{g}_{rr}^R \tilde{\Sigma}_{rn}^< + \tilde{A}_{nr} \tilde{g}_{rr}^< \tilde{A}_{rn}^* \quad (3.84)$$

with $\tilde{g}_{nn}^R = \tilde{A}_{nr}^{-1}$, $\tilde{g}_{nr}^< = \tilde{g}_{nr}^R \tilde{\Sigma}_{nr}^< \tilde{g}_{nr}^A$, and with terms of the form $\tilde{A} = E\mathbf{I} - \tilde{H}$. In mode space, the spatial coordinate in the growth direction will be replaced by the eigenpositions z_i .

3.6 PARTICLE INTERACTION SELF-ENERGIES

The derivation of the particle-particle interaction self-energies is complex and will not be present here. The interested reader can turn to Section 2.7 in Montoya (2023) for more detail. However, this section will provide the pertinent self-energy expressions for electron-phonon interactions while mentioning the most important approximations.

The SCBA approximation is implemented in which the full Green's function is used in the diagrammatic expansion of the self-energies resulting in higher order diagrams (Mon-

toya, 2023). The Hartree and Fock terms were included, while higher order irreducible terms were truncated. In deriving the self-energy for electrons, it was assumed that the phonon bath remains in equilibrium as carrier concentration in IR absorber layers are not large enough to impose non-equilibrium behavior on phonon populations (Compagnone et al., 2002; Bertazzi et al., 2020). Lastly, the principle component of the retarded self-energy is neglected as it leads only to energy renormalization (Aeberhard, 2008). Considering these approximations, the self-energies for electron-phonon interactions can be expressed as follows (Montoya, 2023):

$$\begin{aligned} \hat{\Sigma}^{\lessgtr}(k, E)_{ij} = \sum_{\mathbf{q}} |U_{\mathbf{q}}|^2 e^{iq_z(z_i - z_j)} \{ M [N_{\mathbf{q}} \hat{G}^{\lessgtr}(k - q, E \mp \hbar\omega) \\ + (\langle N_{\mathbf{q}} \rangle + 1) \hat{G}^{\lessgtr}(k - q, E \pm \hbar\omega)] M \}_{ij}, \end{aligned} \quad (3.85)$$

where the Bose-Einstein occupation number of the phonon bath is expressed as $n_{\mathbf{q}} = \left(e^{\beta \hbar \omega_{\mathbf{q}}} - 1 \right)^{-1}$ for a given angular frequency $\omega_{\mathbf{q}}$, mode \mathbf{q} of the phonon, and $\beta = (k_b T)^{-1}$. The retarded self-energy is expressed as (Aeberhard, 2008; Bertazzi et al., 2020):

$$\begin{aligned} \hat{\Sigma}^R(k, E)_{ij} = \sum_{\mathbf{q}} |U_{\mathbf{q}}|^2 e^{iq_z(z_i - z_j)} \{ M [N_{\mathbf{q}} \hat{G}^R(k - q, E + \hbar\omega) \\ + (\langle N_{\mathbf{q}} \rangle + 1) \hat{G}^R(k - q, E - \hbar\omega)] M \}_{ij}, \end{aligned} \quad (3.86)$$

3.6.1 Acoustic Phonons

For the electron-phonon interaction with acoustic phonons, the scattering strength is given according to the deformation-potential scattering theory (Bertazzi et al., 2020):

$$U_{\mathbf{q}} = \sqrt{\frac{\hbar D_a^2}{2V \rho u_l}} \mathbf{Q}, \quad (3.87)$$

where D_a is the deformation potential, which in this work is assumed to be 8 eV (Hess, 2012; Bertazzi et al., 2020), ρ is the mass density of the material, and u_l is the longitudinal sound velocity.

The electron-phonon interaction for acoustic phonons is considered as elastic in this work. Furthermore, assuming that the change in phonon occupation is negligible due to the following: $n_q \approx \frac{k_B T}{\hbar \omega_q} \approx n_q + 1$ (Montoya, 2023), the final expressions for the self-energies for acoustic phonon scattering are (Montoya, 2023):

$$\hat{\Sigma}_{i,j}^{\leq}(k, E) = \frac{1}{\Delta_{ij}} \left(\frac{D^2 k_B T}{A \rho u^2} \right) \sum_{q_t} \{S \hat{G}_{i,j}^{\leq}(k - q_t, E) S\} \quad (3.88)$$

where

$$\frac{1}{\Delta_{ij}} = \frac{1}{L} \sum_{q_z} e^{iq_z(z_i - z_j)} \approx \frac{1}{2\pi} \int_{-\pi/a_L}^{\pi/a_L} dq_z e^{iq_z(z_i - z_j)} = \frac{1}{\pi} \frac{\sin\left(\frac{\pi}{a_L}(z_i - z_j)\right)}{z_i - z_j}, \quad (3.89)$$

and a_L is the growth direction lattice constant.

3.6.2 Polar-Optical Phonons

For polar-optical scattering, within the Fröhlich formalism it is assumed that the phonons are dispersion-less and subject to a scattering strength of (Belenky et al., 2020):

$$U_q = \sqrt{\frac{e^2 \hbar \omega_{LO}}{2V} \left(\frac{1}{\epsilon_\infty} - \frac{1}{\epsilon_s} \right) \frac{Q}{Q^2 + q_0^2}} \quad (3.90)$$

where $\hbar \omega_{LO}$ is the longitudinal phonon energy, assumed to be 30 meV in this work (Bertazzi et al., 2020). Additionally, ϵ_∞ and ϵ_0 are the optical and static dielectric constants, respectively, q_0 is the Debye-Hückel screening length, assumed to be 10 nm in this work (Bertazzi et al., 2020). Applying this to Eq. 3.85 and Eq. 3.86 and applying the axial approximation,

the resulting expression for the self-energies of polar-optical scattering is as follows (Montoya, 2023):

$$\begin{aligned}\Sigma_{i,j}^{\leq}(k, E) &= \frac{e^2 \hbar \omega_{LO}}{4\pi^2} \left(\frac{1}{\epsilon_{\infty}} - \frac{1}{\epsilon_s} \right) \\ &\times \int dq_t q_t F(q_t, s_{ij}, k) \\ &\times \left\{ S \left[(n_{LO} + 1) G^{\leq}(q_t, E \pm \hbar \omega_{LO}) \right. \right. \\ &\quad \left. \left. + n_{LO} G^{\leq}(q_t, E \mp \hbar \omega_{LO}) \right] S \right\}_{i,j},\end{aligned}\tag{3.91}$$

$$\begin{aligned}\Sigma_{ij}^R(k, E) &= \frac{e^2 \hbar \omega_{LO}}{4\pi^2} \left(\frac{1}{\epsilon_{\infty}} - \frac{1}{\epsilon_s} \right) \\ &\times \int dq_t q_t F(q_t, s_{ij}, k) \\ &\times \left\{ M \left[\frac{1}{2} (G^R(q_t, E - \hbar \omega_{LO}) \right. \right. \\ &\quad \left. \left. - G^R(q_t, E + \hbar \omega_{LO})) \right. \right. \\ &\quad \left. \left. + (n_{LO} + 1) G^R(q_t, E + \hbar \omega_{LO}) \right. \right. \\ &\quad \left. \left. + n_{LO} G^R(q_t, E - \hbar \omega_{LO}) \right] M \right\}_{i,j},\end{aligned}\tag{3.92}$$

with

$$\begin{aligned}F(q, s_{ij}, k) &= \int_0^{\frac{\pi}{a_L}} dq_z \cos(q_z s_{ij}) \\ &\times \left[\frac{1}{\sqrt{(k^2 + q^2 + q_z^2 + q_0^2)^2 - 4k^2 q^2}} - \frac{q_0^2}{(k^2 + q^2 + q_z^2 + q_0^2)^2 - 4k^2 q^2} \right]\end{aligned}\tag{3.93}$$

In this expression, $q'_t = k - q_t$, where it is assumed that k is small which is reasonable for a $k \cdot p$ band structure with a direct gap. Also introduced is the expression $s_{ij} = z_i - z_j$.

3.7 MATERIAL PROPERTY EXTRACTION

Once calculated, the Green's functions can be used to determine one-particle properties that are relevant to this work, like the carrier density and current. The carrier density can be computed from (Aeberhard, 2008):

$$\rho_{n,p}(z) = (\mp) \frac{i}{A} \sum_{\bar{k}} \int \frac{dE}{2\pi} G^{\lessgtr}(z, z, \bar{k}, E) \quad (3.94)$$

which in the real space basis used in this work (Eq. 3.2) becomes (Montoya, 2023):

$$\rho_{n,p}(z) = -\frac{i}{A} \sum_k \int \frac{dE}{2\pi} \text{Tr}[\mathbf{G}_{i,j}^{\lessgtr}(k, E)], \quad (3.95)$$

with \mathbf{G} expressed in matrix notation. Furthermore, the current density can be extracted from the following equation (Lake & Pandey, 2006; Montoya, 2023):

$$J_{i \rightarrow i+1} = \frac{1}{\hbar A} \sum_k \int \frac{dE}{2\pi} \left\{ \text{Tr} \left[(H_{i,i+1}(k) - ES_{i,i+1}) G_{i+1,i}^{\lessgtr}(k, E) \right] \right. \\ \left. - \text{Tr} \left[(H_{i+1,i}(k) - ES_{i+1,i}) G_{i,i+1}^{\lessgtr}(k, E) \right] \right\}. \quad (3.96)$$

Another quantity that will prove useful in Chapter 5 is the divergence of the current which can be interpreted as the recombination rate for a scattering mechanism when it is used with the self-energy corresponding with a single scattering mechanism rather than the total one (Steiger, 2009; Montoya, 2023):

$$\frac{\partial J}{\partial z}(z_i, E) = -\frac{1}{2\pi\hbar A \Delta z_i} \sum_k \text{Tr} \left\{ \left[\Sigma^R(k, E) G^{\lessgtr}(k, E) + \Sigma^{\lessgtr}(k, E) G^A(k, E) \right] \right. \\ \left. - \left[G^R(k, E) \Sigma^{\lessgtr}(k, E) - G^{\lessgtr}(k, E) \Sigma^A(k, E) \right] \right\}_{i,i}, \quad (3.97)$$

Due to the non-negligible ballistic effects in the regime of transport investigated, we use resistance scaling analysis to solve for the vertical hole mobility as described in Glennon et al. (2023):

$$pR(L_s) = pR_c + pR_B + \frac{L_s}{\mu e}, \quad (3.98)$$

where R_c and R_B are the contact and ballistic resistances, respectively, L_s is the simulation size, μ is the mobility we are extracting, e the elementary charge, and p represents the hole density. The explanation for this expression will be developed extensively in Chapter 5 in which an analysis on the extraction of mobility from NEGF calculations is presented. This concludes the introduction to the quantum transport theory model used throughout this work. The next chapter will present some basic device physics related to IR PDs for which the mobility calculated via Eq. 3.98 will be important.

CHAPTER 4

Device Physics of Infrared Photodetectors

As pointed out in Chapter 2, type-II superlattice (T2SL) photodetectors (PDs) tend to suffer from high dark currents in comparison with state-of-the-art HgCdTe PDs. For this reason, various barrier architectures have been developed. Barrier devices have achieved some success in improving the detectivity in T2SL PDs (Alshahrani et al., 2022). The nBn structure, was designed to reduce the dark current associated with generation-recombination (GR) mechanisms, tunneling currents, and surface leakage (Maimon & Wicks, 2006). In this work, we have focused on using a model for QE in nBn detectors to evaluate several examples of T2SL structures.

In Section 4.1, the most common sources of dark current are introduced. In doing so, the advantages of nBn PDs over the more traditional pin PD are explained. Then, a comparison of the QE for pin versus nBn architectures will be presented in Section 4.2, demonstrating one of the main drawbacks for nBn PDs.

4.1 PHOTODETECTOR DARK CURRENT

Dark current is defined as the current that persists in a PD when not under illumination. During photodetection, dark current leads to shot noise which limits the detectivity of a PD (Nguyen, 2010). Common sources of dark current are GR mechanisms in the depletion region, thermal generation and diffusion of carriers in the charge neutral region, tunneling, and surface leakage (Nguyen, 2010). Thus, the dark current can be separated as follows:

$$J_{dark} = J_{GR} + J_{diff} + J_t + J_{surf}. \quad (4.1)$$

The following sections will briefly describe each component of the dark current in

relation to pin and nBn PDs. The goal is to demonstrate some of the advantages of the nBn PD design and justify using it to provide a baseline for predicting the impact that the calculated mobility will have on device performance. Figs 4.1a and 4.1b present simplified band diagrams of a pin and an nBn PD, respectively, that will be useful for discussing the dark current mechanisms in the next sections.

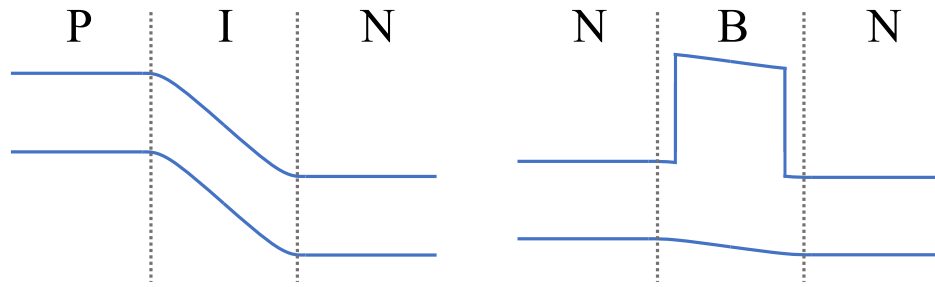


Figure 4.1: Simplified band diagrams of a (a) pin and an (b) nBn PD.

4.1.1 Generation Recombination Current

GR current is a common problem for T2SL materials, limiting the maximum operating temperature for BLIP (Maimon & Wicks, 2006). As mentioned in Chapter 2, Auger recombination tends to be suppressed in T2SL materials due to the strain induced energy separation of the light-hole (LH) and heavy-hole (HH) bands as well as the relatively flat dispersion in the growth direction when compared with bulk semiconductors (Rogalski, 2003). Thus, Shockley-Reed-Hall (SRH) processes tend to dominate the GR dark current (Nguyen, 2010). The dark current due to SRH processes in the depletion region of a p-n junction for mid-gap states at large bias ($eV \gg kT$) is given by the following expression (Nguyen, 2010):

$$J_{dark} = \frac{en_i W}{\sqrt{\tau_n \tau_p}} \frac{V}{V - V_b}. \quad (4.2)$$

where W is the depletion region thickness, V the applied bias, V_b the built-in potential, $\tau_{n(p)}$ the electron (hole) SRH lifetime, and n_i the intrinsic carrier concentration. Note that at low temperatures, the requirement for high reverse bias is relatively low. When comparing the dark current present in a pin versus an nBn PD, the key parameter is the intrinsic carrier concentration. The intrinsic carrier concentration in a semiconductor material has a negative exponential dependence on the BG, as such: (Maimon & Wicks, 2006)

$$n_i \propto \exp\left(\frac{-E_g}{2kT}\right). \quad (4.3)$$

where E_g is the BG. This is the key different between the pin and nBn PD, where in the pin design the depletion region is in the small BG i-region and in the nBn design the depletion region is mostly relegated to the large gap barrier layer. The activation energy for carriers scattering into trap states is significantly greater for wide BG materials as in the nBn barrier layer. Thus, the nBn detector can be expected to reduce the dark current associated with SRH processes compared with the pin design. This distinction is demonstrated via a simple model in Fig. 4.2.

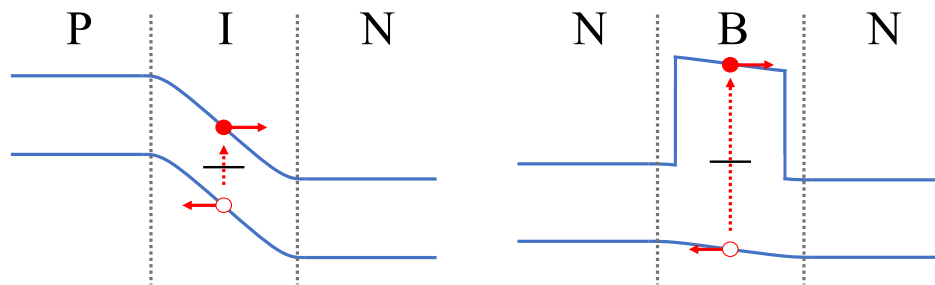


Figure 4.2: Simplified band diagrams of a (a) pin and an (b) nBn PD with representations of SRH scattering in the depletion regions of the devices.

A final comment is that SRH processes are due to material defects with states that exist

within the forbidden gap region of a semiconductor. Therefore, it is not an intrinsic quality of the material and can be reduced via improvement in the growth process (Nguyen, 2010).

4.1.2 Diffusion Current

The diffusion current in a p-n junction can be represented by the following expression (Nguyen, 2010):

$$J_{diff} = J_0 \left(\exp\left(\frac{eV}{kT}\right) - 1 \right), \quad (4.4)$$

where J_0 is the dark current at zero bias. The first term is representative of majority carrier diffusion from a region of low concentration to one of higher concentration. For reverse-biased pin PDs, the potential barrier is likely too high for this component to be significant. However, the second term is associated with the drift of minority carriers in which minority carriers that are able to diffuse to the depletion region are swept up by the electric field (Nguyen, 2010). The expression for the dark current in a p-n junction under the assumption of reflective contacts is the following (Nguyen, 2010):

$$J_0 = en_i^2 \left(\frac{D_n}{N_D L_n} \tanh\frac{w_n}{L_n} + \frac{D_p}{N_A L_p} \tanh\frac{w_p}{L_p} \right), \quad (4.5)$$

where $D_{n(p)}$ is the minority carrier diffusion coefficient, $L_{n(p)}$ is the minority carrier diffusion length, and $w_{n(p)}$ the length of the quasi-neutral region contributing to the dark current.

In the case of nBn detectors under reverse-bias, we expect the diffusion near the depletion region in this case to be dominated by minority carrier drift from the quasi-neutral region. Due to both sides of the depletion region being n-doped, only the n-doped absorber layer have minority holes that can be swept up by the depletion region. If we take the

contribution from only the n-type absorber layer, we would get the following:

$$J_0 = en_i^2 \left(\frac{D_n}{N_D L_n} \tanh \frac{w_n}{L_n} \right). \quad (4.6)$$

Therefore, the difference between the pin and nBn design is that the pin has diffusion contribution from minority electrons and holes in both quasi-neutral regions, while the nBn design is only subject to contribution from the minority holes via one of the quasi-neutral regions. Note, it is assumed that the depletion region extends over the whole i-region and barrier layer for the pin and nBn PD, respectively. Thus, if all other material and device parameters were equal, one would expect the nBn to have lower diffusion dark current than the pin design. However, this is a very rudimentary analysis and an in-depth analysis would have to take into consideration the detailed description of the two devices. This distinction is demonstrated via a simple model in Fig. 4.3.

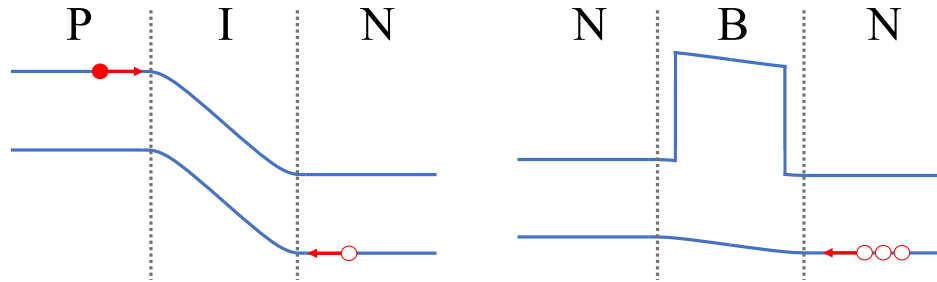


Figure 4.3: Simplified band diagrams of a (a) pin and an (b) nBn PD with representations of diffusion dark current in the quasi-neutral regions of the devices.

4.1.3 Tunneling Current

Another source of dark current in traditional pin PDs is tunneling current from the p-region valence band to the n-region conduction band. The two most common mechanisms are

band-to-band tunneling and trap-assisted tunneling. In band-to-band tunneling, electrons tunnel across the forbidden gap elastically in a p-n junction in reverse bias (Nguyen, 2010). Additionally, trap-assisted tunneling occurs via intermediate trap states which are caused by defects in the crystal structure. These two mechanisms can become problematic for pin PDs at moderate reverse biases Nguyen (2010).

On the other hand, in the nBn structure, both contact regions are n-doped. This means that a larger built-in field, or a larger reverse bias, would be required to align the valence band of one n-side with the conduction band of the other. Tunneling between the conduction bands of the n-regions is also diminished due to the thickness of the barrier region. Thus, the band diagrams suggest that the pin design would be more susceptible to tunneling dark current than the nBn design for equal built-in potential and reverse bias. However, it must be mentioned that the nBn design may require greater reverse bias to achieve optimal performance than the standard pin diode in order to overcome unintentional hole barriers existing between the absorber and contact layers. Thus, the specific design of each device and the device quality will have a significant impact on the relative performance. In Fig. 4.4, an example of electrons tunneling between the valence band of the p-region and the conduction band of the n-region is presented. Additionally, I demonstrate the failure of tunneling occurring between the valence band of the barrier layer and the conduction band of the n-type absorber layer.

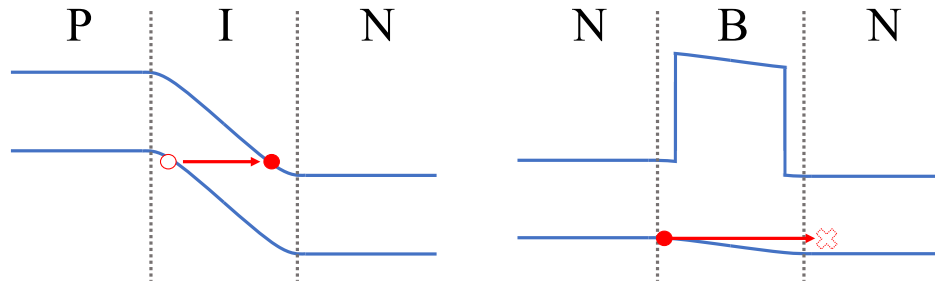


Figure 4.4: Simplified band diagrams of a (a) pin and an (b) nBn PD with representations of tunneling in the pin device and lack of tunneling in the nBn device.

4.1.4 Surface Leakage Current

Surface leakage current is dark current resulting from conduction at the etched surface of the device (Razeghi & Nguyen, 2014). To reduce the surface leakage current in a typical pin PD, surface passivation must be used which can present certain challenges (Tan et al., 2021). However, the nBn structure can be designed such that it contains an intrinsic passivation layer. After lithography, selective etching can be chosen to stop at the barrier layer. Then, the contact layer and the barrier are coated in gold, with the final result being that the barrier layer behaves as a passivation layer as well (Maimon & Wicks, 2006).

Ultimately, the nBn design can inherently suppress dark current due to SRH processes, tunneling, and surface leakage current. This is important for creating IR PDs that can operate at higher temperatures. However, one drawback of the nBn device is that it does not capture carriers as efficiently as the standard pin PD.

4.2 QUANTUM EFFICIENCY

As discussed in Section 2.3.3, the QE of a PD can be defined as the ratio of captured photogenerated carriers to incident photons. This is a measure of the efficiency of capturing

photons resulting in a detection signal. As such, it is an important measurement for evaluating IR PD performance. In the following sections, a brief comparison of the QE for pin devices versus that for nBn devices is presented.

4.2.1 pin Detectors

First, the QE for a backside-illuminated P-on-N device will be investigated. In this case, photons impinge upon the device in the n-region first. Thus, it is the most directly comparable to the nBn design. The quantum efficiency is the sum of the contributions from the two quasi-neutral regions and the depletion region as follows:

$$\eta = \eta_p + \eta_d + \eta_n. \quad (4.7)$$

In the case of the P-on-N device, it will be assumed that the p-doped region does not contribute to the QE. Thus, the QE from the contributions of the depletion region and the n-doped region is calculated, as such (Nguyen, 2010):

$$\eta_d = e^{-\alpha w_n} - e^{-\alpha(w_n - W)} \quad (4.8)$$

$$\eta_n = \left(\frac{\alpha L_n}{\alpha^2 L_n^2 - 1} \right) \left[\frac{\alpha L_n - e^{-\alpha w_n} \sinh\left(\frac{w_n}{L_n}\right)}{\cosh\left(\frac{w_n}{L_n}\right)} - \alpha L_n e^{-\alpha w_n} \right], \quad (4.9)$$

where α is the absorption coefficient. Note that reflection has been ignored in these equations and that perfect collection is assumed in the depletion region where photogenerated carriers are swept to the contacts via the electric field. While an ideal homojunction pin device would have an intrinsically doped active region within which the depletion region extends throughout, unintentional doping can lead to a significantly reduced depletion region

thickness (Nguyen, 2010). In the case of a Ga-based SLs it was shown to be below $0.8\ \mu\text{m}$ (Nguyen, 2010). To probe the potential value of the QE in this device, several material and device parameters that would be relevant for a Ga-free SLS were selected. An absorption coefficient of $1,000\ \text{cm}^{-1}$ and a minority hole lifetime of $1\ \mu\text{s}$ (see Section 2.3.2.1) were assumed. The hole mobility as a function of temperature was extracted from Casias et al. (2020) and used to calculate the minority hole diffusion length as a function of temperature. The Einstein relation can be used to approximate the minority carrier diffusion coefficient from the minority carrier mobility and lifetime via:

$$D_{n,p} = \mu \frac{kT}{q}. \quad (4.10)$$

The minority carrier diffusion length can then be calculated from the diffusion coefficient and the mobility via:

$$L_{n,p} = \sqrt{D_{n,p}\tau_{n,p}}. \quad (4.11)$$

A depletion region width of $0.8\ \mu\text{m}$ was selected while the rest of the device was chosen to be $4.2\ \mu\text{m}$ for a total of $5\ \mu\text{m}$ for the active region. The QE calculated as a function of temperature has been plotted in Fig. 4.5. Next, these results will be compared with those of an nBn detector described in the next section. 4.5.

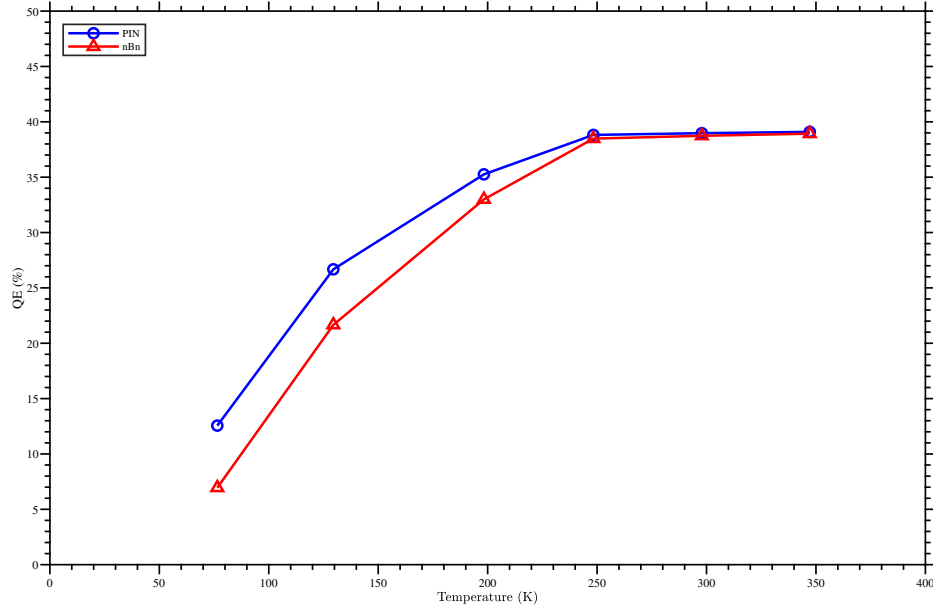


Figure 4.5: Calculated QE for simple models of pin and nBn detectors with the same material parameters and the same active region thickness. The depletion region extends into the active region in the homojunction pin, but the depletion region is encompassed completely within the barrier layer. Photogenerated carriers in the depletion region of the device are collected efficiently resulting in higher QE for the pin device at lower temperatures.

4.2.2 nBn Detectors

The QE of a backside-illuminated nBn detector is taken as just the n-doped region contribution:

$$\eta_n = \left(\frac{\alpha L_n}{\alpha^2 L_n^2 - 1} \right) \left[\frac{\alpha L_n - e^{-\alpha w_n} \sinh\left(\frac{w_n}{L_n}\right)}{\cosh\left(\frac{w_n}{L_n}\right)} - \alpha L_n e^{-\alpha w_n} \right]. \quad (4.12)$$

This equation assumes absorption only occurs in the active n-doped region. Absorption in the IR regime will not occur in the high BG barrier layer and it is assumed that the other n-doped layer is too thin to contribute significantly. All of the other material parameters were selected to be the same as those for the pin device in Section 4.2.1. The only difference is

that the absorber n-doped region will be $5\ \mu\text{m}$ in this case. This was chosen to account for the fact that no absorption occurs in the depletion region of the B-n junction in which the depletion region extends nearly exclusively over the barrier layer. Thus, the active region of the nBn device is the same length as that in the pin device. The QE calculated as a function of temperature for the nBn detector was also included in Fig. 4.5. It is clear that the QE in the pin device is higher than that in the nBn detector at temperatures at which IR PDs are currently operated. This can be attributed to the fact that the nBn design is entirely reliant on diffusion of photogenerated carriers from the active region whereas the depletion region in the pin design encompasses a portion of the active region. Carriers that are generated within the depletion region are efficiently captured due to the built-in electric field. Thus, the pin PD has an advantage over the nBn PD in the context of these simplified models. However, the overall detectivity of a PD, which is calculated as follows (Nguyen, 2010):

$$D^* = \frac{q\lambda}{hc} \eta \sqrt{\frac{R_0 A}{4kT}}, \quad (4.13)$$

is dependent on the dark current (via the $R_0 A$ term) as well as the QE. The advantages of the reduced dark current in the nBn detector can thus result in higher detectivity under the right conditions (Khoshakhlagh et al., 2010).

CHAPTER 5

Mobility Extraction from Quantum Transport Calculations

The bulk of the work presented in this chapter has been published in Glennon et al. (2023). The details have been reproduced and repurposed to serve the overall narrative of this dissertation.

5.1 INTRODUCTION

In this chapter, the results of an investigation we conducted that validates the use of Eq. 3.98 for calculating the vertical hole mobility is presented. As described in Section 3.1, the use of quantum transport methodologies towards the study of nanostructured materials like SLs is advantageous as it reduces the need for uncontrolled approximations. While these methodologies can be effective in studying material properties, typically the computational complexity of the formalism precludes the extension of these simulations to those of a full PD from source-to-drain. Therefore, it is often beneficial to extract parameters that approximate the transport behavior demonstrated in these quantum transport methodologies and apply them within a more computationally feasible model to predict device properties. The most pertinent parameter for this work is the carrier mobility, an important parameter for carrier collection, which can be used to approximate the effects that the nanometer-scale phenomena have on the carrier transport. This extracted mobility can then be used to model PD performance through the use of simpler transport models. One such example is quantum-corrected DD transport models (Witzigmann et al., 2000; de Falco et al., 2005; Ancona & Svizhenko, 2008; Tibaldi et al., 2019). This includes approaches like Schrodinger-Poisson DD (Tibaldi et al., 2021) and landscape-localization DD (Arnold et al., 2016; Filoche et al., 2017) approaches. Alternatively, the mobility can be incorporated in simpler analytical models for common PD architectures, as described in Chapter 4.

However, carrier mobility is not germane to quantum transport methodologies, such as NEGF, and requires special considerations. In this chapter, we will examine the common methods for carrier mobility extraction from NEGF calculations in the context of T2SLs.

5.2 MESOSCOPIC PICTURE OF MOBILITY

Several methods for extracting the carrier mobility from quantum transport simulations have been demonstrated in the literature. However, it is not clear whether the concept of mobility is valid for arbitrarily small devices. Theoretical mobility investigations (Shur, 2002; Wang & Lundstrom, 2003; Huet et al., 2007; Zilli et al., 2007; Gnani et al., 2010; Riyadi & Arora, 2011; Arora, 2012; Guarnay et al., 2014; Bellotti et al., 2021) and experimental evidence (Łusakowski et al., 2005, 2007; Wang et al., 2008; Liu et al., 2011; Gu et al., 2012; Majumdar & Antoniadis, 2014; Lin et al., 2016) demonstrate a degradation in the apparent mobility for nanoscale devices, suggesting that the use of the macroscopic mobility becomes questionable at this scale. For computationally demanding formalism, such as NEGF, this can lead to inaccuracies when attempting to use the nanoscale transport simulations to make predictions about device performance if care is not taken.

NEGF calculations are limited computationally to relatively small domains; for the method we typically employ in this dissertation this tends to be on the order of a few hundreds of nanometers. At this scale, the concept of an intrinsic mobility may break down. In nanoscale devices, the ballistic resistance of the device can become significant, limiting the carrier velocity that can be achieved in the device before exiting to the contacts. Shur (2002) presented a phenomenological model for qualitatively describing the “apparent” mobility measured in short channel HEMT devices. In this model, the apparent mobility is described via a Matthiessen’s rule relationship between the standard diffusive mobility and what they refer to as the “ballistic” mobility, a representation of the reduction in the

apparent mobility due to the ballistic resistance, as in the following: (Shur, 2002)

$$\frac{1}{\mu_{app}} = \frac{1}{\mu_{ball}} + \frac{1}{\mu_{diff}} \quad (5.1)$$

To help conceptualize this behavior, we used the expression for the ballistic mobility of a 3D bulk resistor with parabolic bands set between two semi-infinite contacts:

$$\mu_{ball} = \frac{Lv_T}{2(K_B T/q)} \frac{\mathcal{F}_0(\eta_F)}{\mathcal{F}_{1/2}(\eta_F)}, \quad (5.2)$$

where v_T is the unidirectional thermal velocity:

$$v_T = \sqrt{\frac{2k_B T}{\pi m^*}}, \quad (5.3)$$

and

$$\eta_F = (E_F - E_c)/k_B T. \quad (5.4)$$

We derived this expression in Appendix A according to the Landauer formalism. Next we calculated the ballistic mobility of a hypothetical 3D bulk resistor as a function of device length using Eq. (5.2) at a temperature of 77 K with a conduction band effective mass of InAs: 0.023 (Nakwaski, 1995). Then, assuming a diffusive mobility of $50,000 \text{ cm}^2 \text{ V}^{-1} \text{ s}^{-1}$, estimated for electrons in InAs at 77 K with a density of $1.7 \times 10^{16} \text{ cm}^{-3}$ (Rode, 1975), we calculated the apparent mobility using Eq. (5.1) and plotted the results in Fig. 5.1.

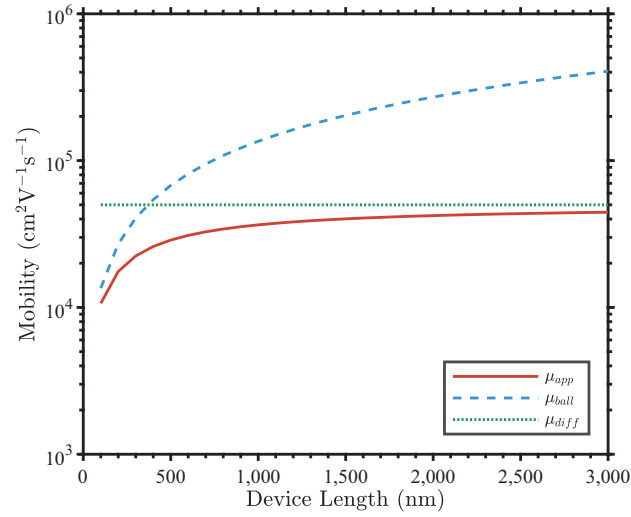


Figure 5.1: The apparent, ballistic, and diffusive-limited mobility calculated for an example InAs device at 77 K as a function of device length. Reprinted with permission from Glennon et al. (2023).

It is clear that the apparent mobility approaches the diffusive mobility in the limit of large devices. However, for smaller devices, the apparent mobility is reduced due to the effect of the ballistic resistance. In the limit of small devices, the carrier velocity is limited entirely by the ballistic resistance. Thus, at the mesoscopic scale, it is clear that the apparent mobility is no longer intrinsic, and depends on the geometry of the device. This is an issue for NEGF calculations that are limited computationally. If one extracts the apparent mobility in a 500 nm NEGF simulation and attempts to use it as an intrinsic material parameter for use in a 3,000 nm device, the results will be inaccurate. Thus, care must be taken when extracting the mobility from NEGF calculations to ensure the understanding of what value is actually being extracted and how to apply it to a larger device simulation. Note that the details of the NEGF model that will be used in the following chapter can be found in Chapter 3.

5.3 INAS/GASB EXAMPLE STRUCTURE

Prior to the examination of the mobility extraction methodologies, the T2SL structure used in the investigation will be described. We chose a prototype 10/10 ML InAs/GaSb SL, lattice matched to a GaSb substrate. In Fig. 5.2, the electronic structure of this SL is presented, computed using the 4×4 $k \cdot p$ model with Bloch boundary conditions.

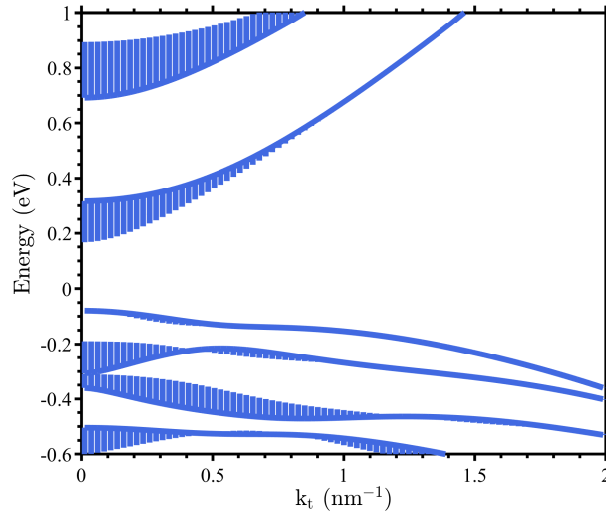


Figure 5.2: The calculated energy band structure of a 3/3 nm InAs/GaSb SL plotted as a function of the transverse wave vector and modified with vertical lines representing the dispersion in the vertical wave vector. The band gap results in a cut-off wavelength of approximately $5 \mu\text{m}$. Reprinted with permission from Glennon et al. (2023).

We selected this structure to produce a nominal cutoff wavelength of approximately $5 \mu\text{m}$ which is in the MWIR regime. The dispersion in the growth direction is represented by vertical lines stemming from the energy of the corresponding in-plane wave number k_t , providing an estimate for the miniband width for a given value of k_t . Of note is that there is much less dispersion in the growth direction of the highest heavy-hole band than there is in the first conduction band, suggesting that holes will have a lower vertical mobility than electrons. This assumption will be confirmed in Section 5.4. We selected an ideal SL, as it exhibits transport with more coherent character than a more realistic disordered structure as

in Bellotti et al. (2021); Glennon & Bellotti (2023); Glennon et al. (2024); ?. As mentioned in Section 5.2, mobility becomes harder to define in simulations where coherent transport is significant. Thus, an ideal SL can better exemplify the differences in the mobility extraction methodologies. As for the contacts, we chose GaSb for simulating hole transport, but the choice in the case of electrons was not as straightforward. The choice of InAs produced high carrier injection near the contact regions resulting in difficulty differentiating between the free electron and hole populations in the multiband context. Thus, we selected the quaternary alloy $\text{GaSb}_{0.10}[\text{InAs}_{0.91}\text{Sb}_{0.09}]_{0.90}$, as defined in Vurgaftman et al. (2001), which is lattice matched with GaSb and avoids these complications. Using the calculated band structure, as in Fig. 5.2, we calculated the Fermi energy at equilibrium for the SL so that the target carrier exhibited a concentration of approximately $2 \times 10^{16} \text{ cm}^{-3}$ in the SL region. We have included example band diagrams of the structures used for the electron and hole calculations in Fig. 5.3a and Fig. 5.3b, respectively.

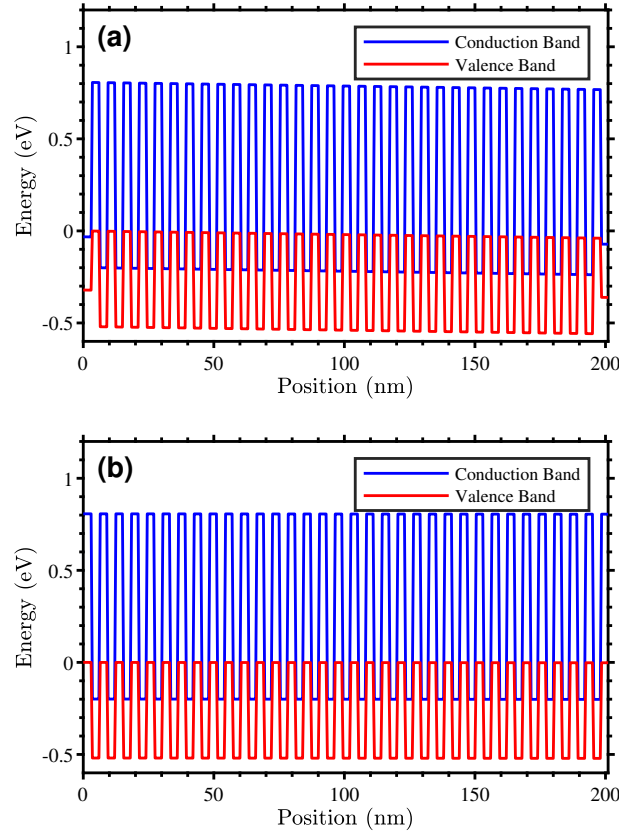


Figure 5.3: Example band diagrams for the (a) electron and (b) hole mobility calculations.

5.4 ANALYSIS OF MOBILITY EXTRACTION METHODOLOGIES

5.4.1 Average Velocity Method

The first method for extracting mobility is based on extracting the mobility from the calculated average carrier drift velocity. For transport in a resistive region, the electron and hole mobility can be extracted from NEGF calculations using the average of the carrier drift velocity, $v_{n,p}$ (Bertazzi et al., 2020; Bellotti et al., 2021):

$$v_{n,p} = \left\langle \frac{J_{n,p}}{\mp en} \right\rangle, \quad (5.5)$$

where the carrier mobility is then calculated via:

$$\mu_{n,p} = \frac{v_{n,p}}{F}. \quad (5.6)$$

$J_{n,p}$ is the carrier current (Eq. (3.96)), e the elementary charge, F the applied electric field in the growth direction, and n represents the carrier density (Eq. (3.95)). Given that this method assumes a resistive region and doesn't account for resistance associated with the inclusion of contacts, ballistic or otherwise, the mobility being calculated is the apparent mobility, as defined in section 5.2. (Glennon et al., 2023) This will become more apparent upon review of the results using this methodology.

Prior to the discussion of the results, a point of clarification about the correct way of calculating the average velocity is pertinent. Carrier density is not constant throughout highly heterogeneous structures like SLs, and due to current conservation, neither is the carrier velocity. We provide an example of the spatial variation in the carrier density and velocity for a T2SL, calculated via Eq. (3.95) and Eq. (5.5), respectively, in Fig. 5.4.

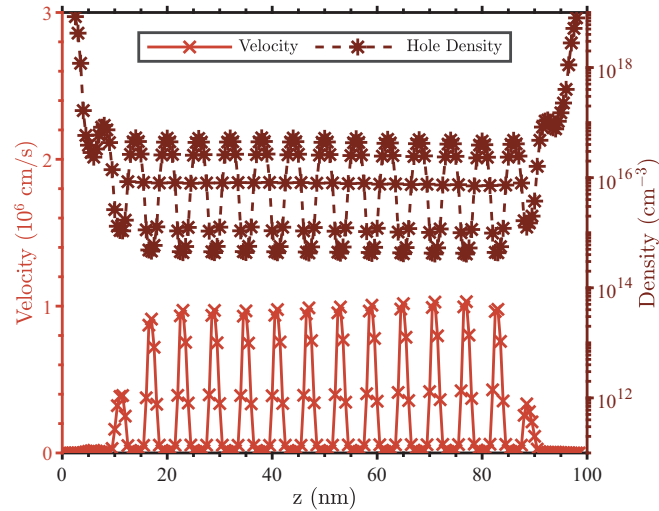


Figure 5.4: The calculated hole velocity magnitude (light red line with x's) and density (dark red dashed line with asterisks) throughout the growth direction of a 100nm MWIR InAs/GaSb structure. Reprinted with permission from Glennon et al. (2023).

The variation in the carrier density needs to be considered, as areas of high density have low velocity and vice versa. An unweighted spatial average of the velocity will overvalue (undervalue) the higher (lower) velocities. We demonstrate this concept in Fig. 5.5, where a small concentration of carriers are moving at higher velocities while a higher concentration are moving at lower velocities.

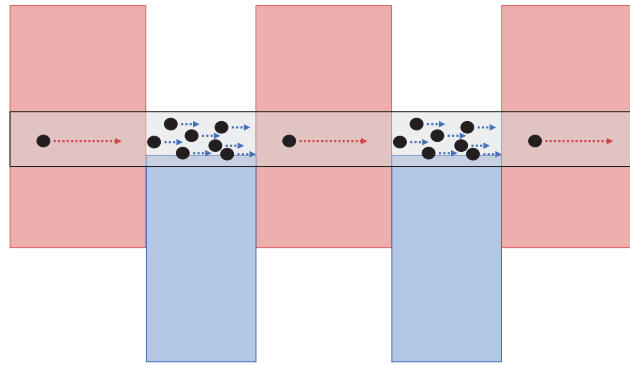


Figure 5.5: A conceptual model demonstrating that a simple average of the velocity over space, without accounting for variation of density, will overestimate the true average velocity per particle, as the concentration of low velocity particles is far higher than high velocity particles. Reprinted with permission from Glennon et al. (2023).

Considering the discretized basis, a concentration-weighted average of the carrier velocity $v_{n,p}$ can be taken as:

$$v_{n,p}(z) = \frac{\sum_i^N [v_i n_i \Delta z_i]}{\sum_i^N [n_i \Delta z_i]} \quad (5.7)$$

where v_i is the velocity at node i , n_i is the carrier density, Δz_i is the element size, and N is the number of nodes. In the work presented in this chapter, we used a spatially uniform grid, so the element size can be factored out of both summations and removed via cancellation of the equivalent terms. Eq. (5.7) considers the variation in the concentration of carriers and can be interpreted as an expectation value of velocity. Given that mobility is a concept that

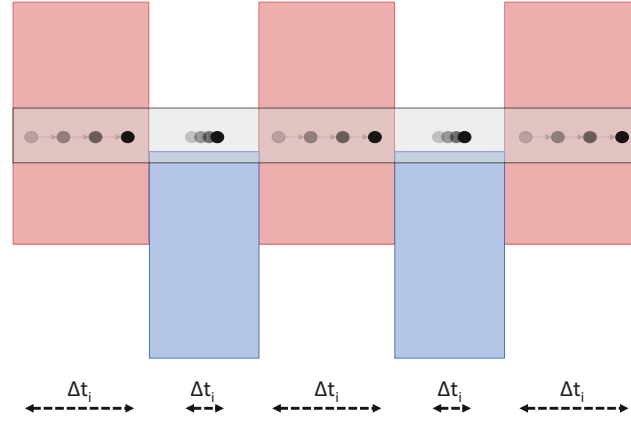


Figure 5.6: A conceptual model that demonstrates that a simple spatial average of velocity over the entire structure will overestimate the average velocity of the particle as it transits the SL as the particle is spending significantly more time in the wells at lower velocities. Reprinted with permission from Glennon et al. (2023).

is typically used to describe transport in a semi-classical model, we motivate that Eq. (5.7) is the correct velocity average to describe transport by discussing the average velocity from a classical perspective. In classical mechanics, the form of velocity for describing the transport of a particle over a distance is the time-average of the velocity. This is presented clearly in Fig. 5.6; the carrier spends more time traversing the well at lower velocity than the barrier.

Using Eq. (5.5), we demonstrated that taking the concentration-weighted average (Eq. (5.7)) on a 1D discretized grid is equivalent to taking the time-average of the velocity of a carrier in the structure:

$$\begin{aligned} \frac{\sum_i^N [v_i n_i \Delta z_i]}{\sum_i^N [n_i \Delta z_i]} &= \frac{\sum_i^N \left[v_i \frac{J}{ev_i} \Delta z_i \right]}{\sum_i^N \left[\frac{J}{ev_i} \Delta z_i \right]} \\ &= \frac{\sum_i^N \Delta z_i}{\sum_i^N \left[\frac{\Delta z_i}{v_i} \right]} \end{aligned}$$

$$= \frac{\sum_i^N \Delta z_i}{\sum_i^N \Delta t_i} \quad (5.8)$$

where t_i is the time it takes the carrier to travel the distance Δz_i . Thus, Eq. (5.7) was confirmed to be the correct approach for calculating the average velocity used in Eq. (5.5).

Moving on to the results of the average velocity method for the structures defined in section 5.2, we computed the apparent vertical mobility from the average velocity method (Eq. (5.5)) as a function of temperature for electrons and holes subjected to electric field strengths of $2,000 \text{ V cm}^{-1}$ and 100 V cm^{-1} , respectively, and reported the results of the average mobility in Fig. 5.7.¹

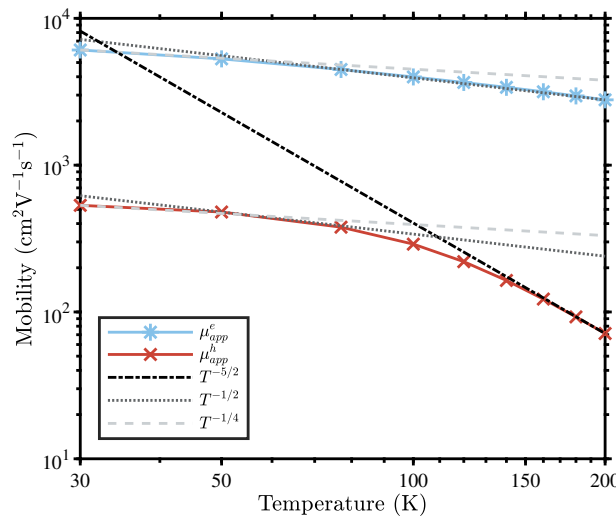


Figure 5.7: The apparent vertical electron (blue line with asterisks) and hole (red line with x's) mobility as a function of temperature calculated using the average velocity method for a 200nm MWIR T2SL with an electric field of strength $2,000 \text{ V cm}^{-1}$ (100 V cm^{-1}). Reprinted with permission from Glennon et al. (2023).

The first thing that is noticeable is that the hole mobility was an order of magnitude lower than the electron mobility, which is expected given the higher hole effective mass and low

¹We chose a higher electric field for studying electrons to increase scattering in the domain as electron transport is highly coherent in this structure. Inelastic scattering will smooth spectral functions, so, in an absence of adequate scattering, the required number of energy integration points can be prohibitively large (Niquet et al., 2014).

HH dispersion in the vertical direction of our structure (Fig. 5.2). This is also consistent with the relative magnitude of the vertical electron mobility and hole mobility reported in T2SL experimental values presented in Section 2.3.2.2.

The electron (hole) mobility decreased monotonically from approximately $6,000\text{cm}^2\text{V}^{-1}\text{s}^{-1}$ ($500\text{cm}^2\text{V}^{-1}\text{s}^{-1}$) to $2,800\text{cm}^2\text{V}^{-1}\text{s}^{-1}$ ($70\text{cm}^2\text{V}^{-1}\text{s}^{-1}$) as temperature increased from 30K to 200K. The electron and hole mobility data exhibited different temperature dependencies which suggests different transport behavior. We compared these trends qualitatively to that of bulk material in the regimes of coherent and diffusive transport. The bulk coherent regime can be described using the analytical expression we derived for the mobility of a 3D bulk device with parabolic bands and constant effective mass under ballistic transport (Eq. 5.2). Given the very small temperature dependence of the Fermi integrals term for non-degenerate doping we found that the temperature dependence of the expression is nearly $T^{-1/2}$. This provides context for the temperature dependencies exhibited in Fig. 5.7 for electrons and holes. The electron mobility exhibited a temperature dependence that is near the $T^{-1/2}$ dependence of bulk ballistic transport, while the hole mobility exhibited a transition from a nearly $T^{-1/4}$ dependence to one that approached $T^{-5/2}$. This suggests that electrons exhibited coherent dominated transport throughout the temperature range investigated, while holes transitioned from coherent dominated to diffusive dominated transport. The $T^{-5/2}$ trend for hole mobility at higher temperatures is likely due to POP scattering dominated transport which is similar to the temperature dependence predicted for POP scattering of electrons in InAs: $\sim T^{-11/5}$ (Li, 1976), while the $T^{-1/4}$ dependence could be due to either a deviation in bulk-like behavior or the Fermi integral terms due to degenerate doping. A qualitatively similar transition in transport regimes from low to high temperature was evident in the experimental vertical electron mobility reported by Swartz & Myers (2014) for a $4.3\mu\text{m}$ SL layer. The results

are reproduced in Fig. 5.8.

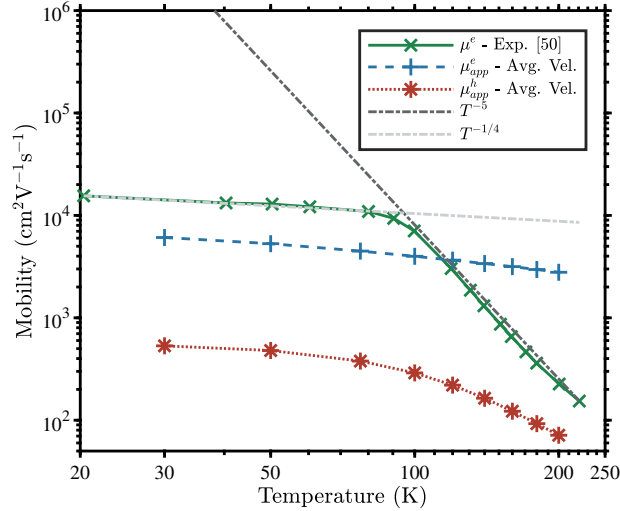


Figure 5.8: The vertical electron mobility as a function of temperature (green line with x's) for a $4.3 \mu\text{m}$ LWIR SL as reported by Swartz and Myers Swartz & Myers (2014). Also plotted are the apparent vertical electron (blue dashed line with pluses) and hole (red dotted line with asterisks) mobility calculated using the average velocity method for a 200 nm MWIR T2SL. Reprinted with permission from Glennon et al. (2023).

The experimental data exhibited an approximately T^{-5} dependence at high temperature, while the calculated hole mobility exhibited a $T^{-5/2}$ dependence. At low temperature, the dependence of the experimental data is nearly $T^{-1/4}$ which is similar to the lowest temperature dependencies of electron and hole apparent mobility (Fig. 5.7) which may suggest coherent transport is present in the experimental data at low temperature. The unexpectedly low mobility at higher temperatures in the experimental data compared with the calculated data for electrons, as well as the T^{-5} dependence, was likely due to the specific structural details of the experimental device not included in the simulation. The non-negligible influence of coherent transport in these calculations suggests that the use of this method may not be reasonable at the temperatures and scale investigated.

As demonstrated in Section 5.2, when ballistic behavior is significant, the apparent mobility is dependent on device length. Evidence of this behavior was demonstrated in

the vertical carrier mobility of electrons and holes for different simulation sizes presented in Figs. 5.9a and 5.9b, respectively.

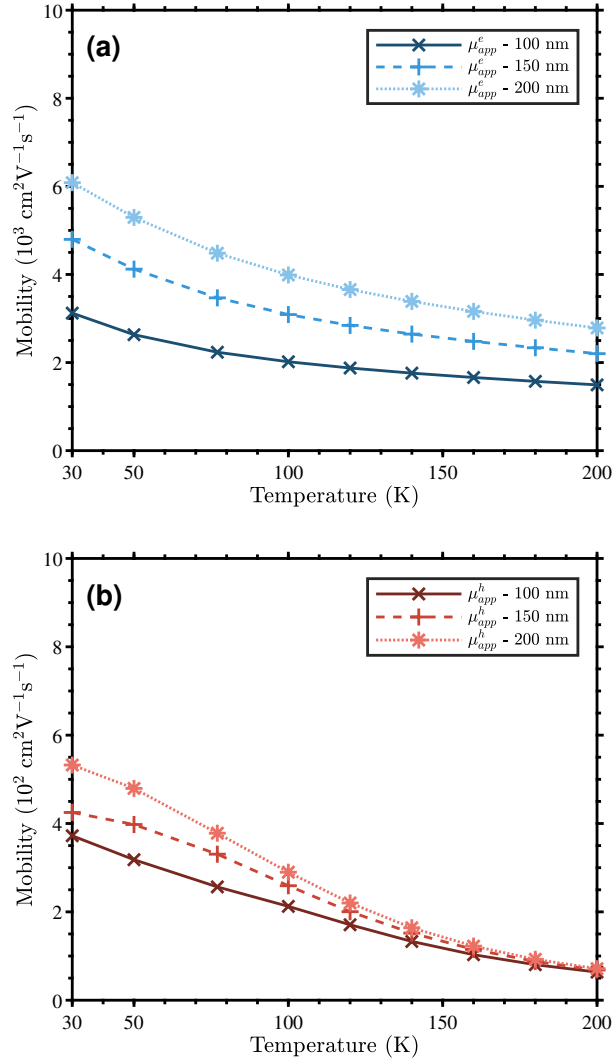


Figure 5.9: The calculated apparent vertical electron (a) and hole (b) mobility as a function of temperature for different simulation sizes, as calculated via the average velocity method. Reprinted with permission from Glennon et al. (2023).

There was a clear length dependence in the calculated mobility for both electrons and holes. The length dependence of the hole mobility is less pronounced compared with that of the electron mobility at a given temperature due to hole transport being more diffusive in nature

than electron transport. These results emphasize the point made in Section 5.2 that using the mobility extracted from NEGF calculations via the average velocity method to predict device properties for a larger device under the assumption that the calculated mobility is intrinsic may be invalid. Considering the issues with an approach such as this, two methods were developed that attempt to exclusively extract the diffusive component of the mobility (Eq. (5.1)). These methods are described in Sections 5.4.2 and 5.4.3, respectively.

As a final note, in Fig. 5.10a and Fig. 5.10b we presented the mobility as a function of electric field strength calculated using the average velocity method at 200 K for electrons and holes, respectively, confirming that the chosen electric fields are below the critical value.

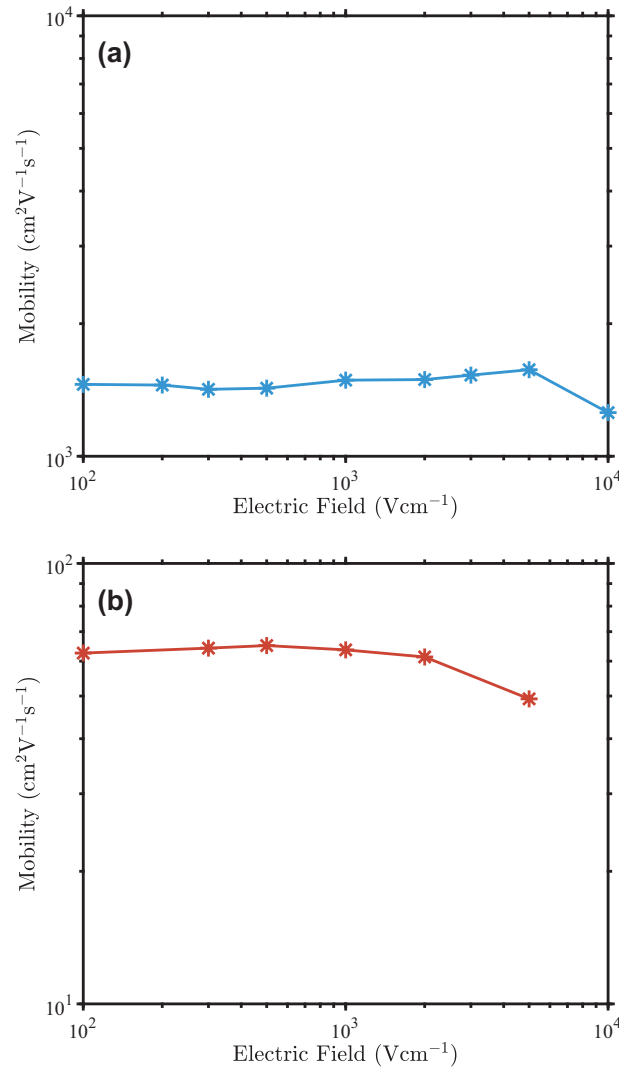


Figure 5.10: The mobility calculated as a function of electric field strength for (a) electrons and (b) holes at a temperature of 200 K using the resistance scaling method. Reprinted with permission from Glennon et al. (2023).

5.4.2 Ballistic Approximation Method

In consideration of this degradation in apparent mobility, a method of mobility extraction evolved from the model introduced by Shur (2002). This model, which is sometimes referred to in the literature as “Shur’s model”, generally incorporates an approximation for the ballistic mobility either from analytical methods (Shur, 2002; Wang & Lundstrom, 2003;

Zilli et al., 2007; Guarnay et al., 2014; Lin et al., 2016) or extracted from a purely ballistic simulation (Huet et al., 2007, 2008; Poli & Pala, 2009; Poli et al., 2009; Pala et al., 2009; Frey et al., 2011). The literature focusing on extracting mobility from quantum transport calculations have focused on the latter method (Poli & Pala, 2009; Poli et al., 2009; Pala et al., 2009; Frey et al., 2011). It is worth mentioning that Shur proposed his model only to “crudely illustrate” the impact that ballistic effects can have on mobility (Shur, 2002), not necessarily to use as a model for making accurate predictions. For the purposes of this dissertation this procedure will be referred to as the “ballistic approximation” method.

Assuming a Matthiessen’s rule relationship between diffusive and ballistic mobility components, as described in Eq. (5.1), the apparent mobility μ_{app} is separated into two components (Shur, 2002):

$$\frac{1}{\mu_{app}} = \frac{1}{\mu_{ball}} + \frac{1}{\mu_{diff}} \quad (5.9)$$

where μ_{ball} is the ballistic mobility and μ_{diff} is the diffusive mobility. We obtained an approximate value of the ballistic mobility from NEGF calculations without the ACO and POP scattering self-energies. Then, we calculated the diffusive, or scattering-limited, mobility via Eq. (5.1). It is noteworthy that Matthiessen’s rule is not generally valid (Esseni & Driussi, 2011) and that its use for separating the ballistic component from the diffusive component has been demonstrated to be questionable at high bias by Wang & Lundstrom (2003) as well as in a non-homogeneous nanowire FET at low bias by Frey et al. (2011).

We used the ballistic approximation method to calculate the apparent, ballistic, and diffusive components of the vertical mobility for electrons and holes via NEGF simulations of several lengths (100 nm, 150 nm, and 200 nm). The results are presented in Figs. 5.11a, 5.11b, and 5.11c (5.11d, 5.11e, and 5.11f) for electrons (holes).

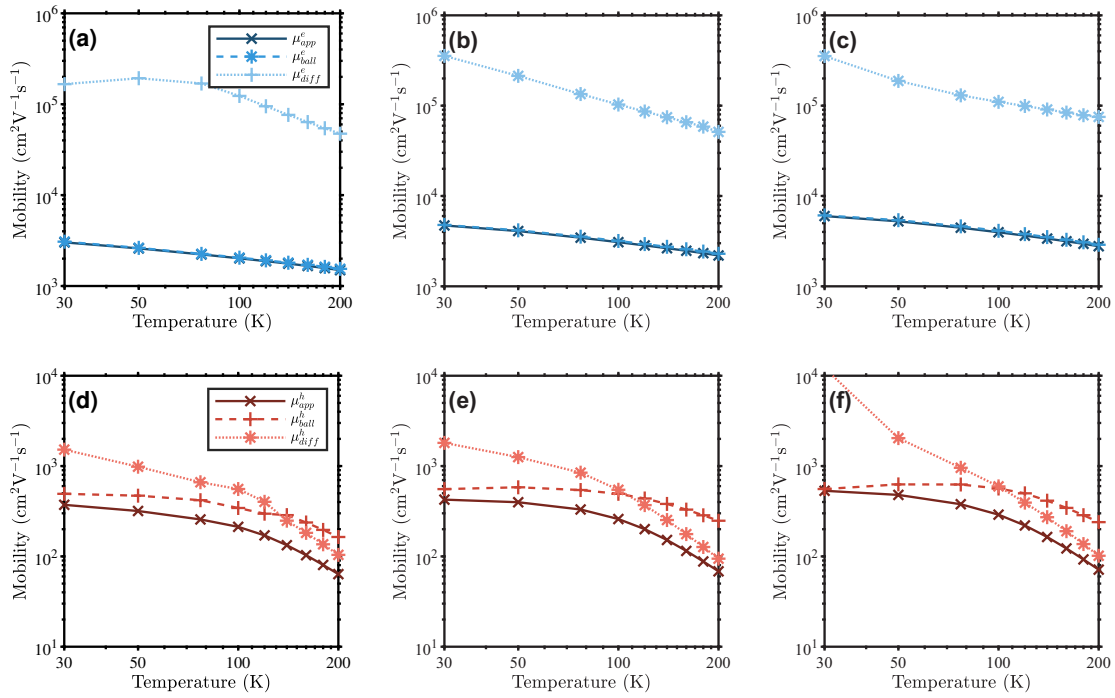


Figure 5.11: The calculated vertical electron (hole) mobility as a function of temperature for simulation sizes of (a) ((d)) 100 nm, (b) ((e)) 150 nm, and (c) ((f)) 200 nm, respectively, as calculated via the ballistic approximation method. The apparent mobility (dark blue/red line with x's) is broken up into components of ballistic mobility (blue/red line with asterisks) and diffusive mobility (light blue/red line with crosses). Reprinted with permission from Glennon et al. (2023).

Looking first at Fig. 5.11c, the electron transport was shown to be nearly completely coherent throughout the temperature range we investigated for the 200 nm simulation which was consistent with the analysis given in Section 5.4.1. The difference between the mobility extracted from the diffusive and ballistic calculations was negligible resulting in very large values for the diffusive mobility. Similar results were observed in Fig. 5.11a and Fig. 5.11b, as expected. However, the results for holes exhibited different behavior. There is a transition between ballistic dominated and diffusive dominated transport at decreasing temperatures for increasing simulation size. Transition temperatures occurred at approximately 130 K, 110 K, and 100 K for simulation sizes of 100 nm, 150 nm, and 200 nm, respectively.

These results were also consistent with those of Section 5.4.1.

There are several caveats we made about this method. First, as mentioned previously in this section, it is not clear how valid Matthiessens rule (Eq. (5.1)) is in the regimes investigated. If it is not valid, then the extracted mobility components could be inaccurate. Furthermore, even if Eq. (5.1) is valid, the diffusive mobility may be a function of the geometry at this scale, so it may not be representative of the intrinsic mobility for an infinitely large SL and instead would only represent diffusive transport in the specific geometry simulated. Finally, the mobility extracted from a ballistic calculation is not necessarily identical to the “ballistic component” of mobility, as defined via Eq. 5.1, in a calculation that includes phonon scattering. Two observations motivate this conclusion. Firstly, when comparing the ballistic approximation method (Eq. 5.1) with our mobility extraction method of choice: Eq. (3.98), it is clear that the ballistic mobility should incorporate a component from the general contact resistance R_c , in addition to the ballistic resistance R_B , which will not be captured in the ballistic calculation (Guarnay et al., 2014). Secondly, the resistance in a ballistic calculation may not be identical to the ballistic resistance in a calculation with diffusive processes (Niquet et al., 2014). We exemplified this by comparing the LDOS calculated with, and without, acoustic and polar-optical phonon scattering for holes at 200 K with an electric field strength of 100 V cm^{-1} in Fig. 5.12a and Fig. 5.12b, respectively.

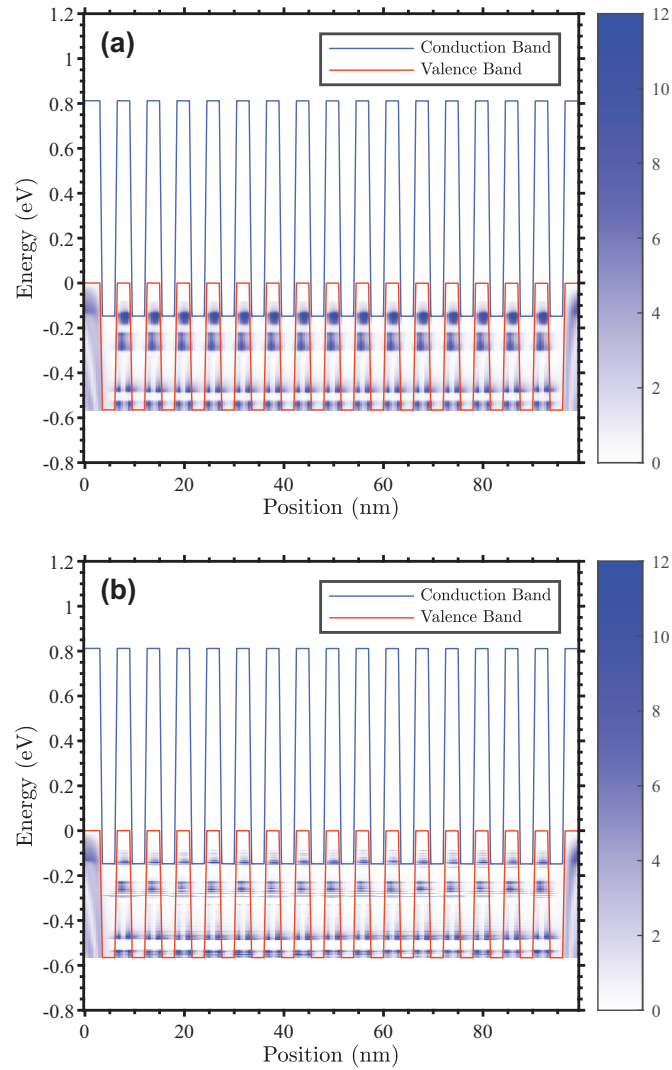


Figure 5.12: The calculated LDOS (in 10^{15} cm^{-3}) at 200K for the SL structure used to calculate hole transport for a calculation with (a) ACO and POP scattering and one (b) without scattering overlaid on top of the conduction and valence bands of the SL structure. The portion of the LDOS corresponding with the conduction miniband states have been removed for clarity. Reprinted with permission from Glennon et al. (2023).

While similar, the LDOS differed between the calculations suggesting a difference in the character of the minibands. Furthermore, we found that the diffusive mobility for holes at low temperatures, as well as those for electrons at all temperatures, were inconsistent when changing the simulation size.

There was some evidence that this inconsistency may be partially the result of insufficiently dense energy meshes which are limited due to computational requirements. For holes, we fixed the energy grid spacing for the diffusive calculations at 1 meV while varying that for the ballistic calculations and calculated the diffusive mobility using the ballistic approximation at temperatures of 30 K, 50 K, and 77 K. The results were reported in Fig. 5.13b. For electrons, the transport in the diffusive calculations is more coherent than it is for holes, thus when using the ballistic approximation it is necessary to reduce the energy grid of the diffusive calculation as well to get positive values for the diffusive mobility. Furthermore, this issue of energy grid spacing for electrons persisted throughout the temperature range investigated, so we varied the temperature between 30 K and 200 K in Fig. 5.13a.

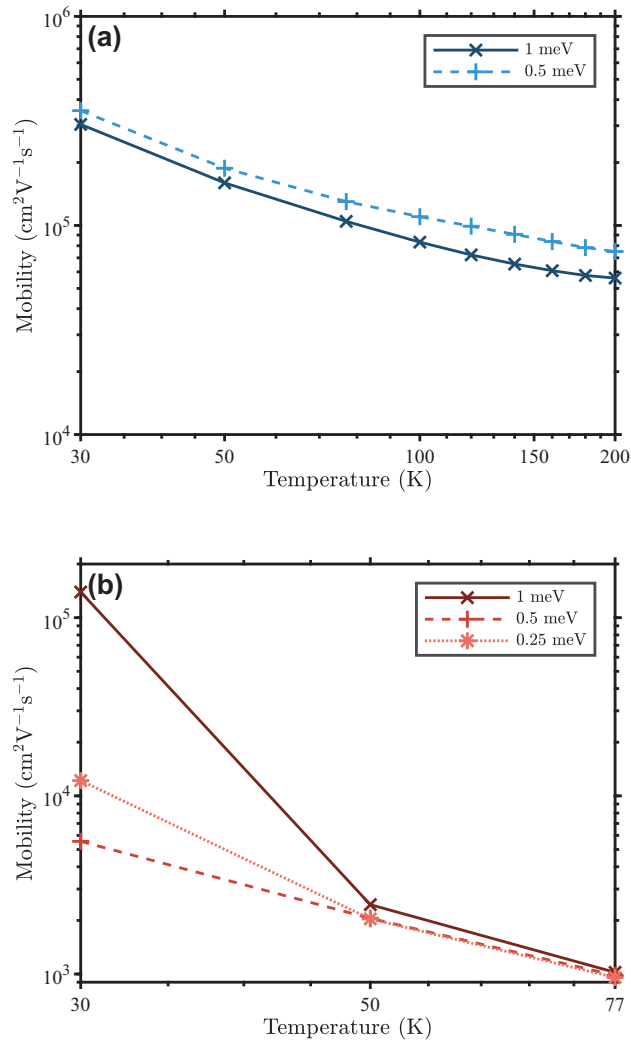


Figure 5.13: The mobility calculated as a function of temperature and density mesh spacing size using the ballistic approximation for (a) electrons and (b) holes with electric field strengths of $2,000 \text{ V cm}^{-1}$ and 100 V cm^{-1} , respectively. Reprinted with permission from Glennon et al. (2023).

The calculated mobility varied significantly with energy mesh density for holes at low temperature and electrons generally, and had not yet reached a “converged” value. This suggests that denser energy meshes are needed, but they are not computationally feasible at this time. However, the consistency of the results for holes at higher temperatures (Fig. (d), Fig. (e), and Fig. (f)) suggests that the ballistic approximation method could be reasonable

to calculate diffusive mobility for holes at high temperatures. However, this method relies on several unconfirmed assumptions, which is contrasted with the method that is introduced in the next section.

5.4.3 Resistance Scaling Method

The final methodology for extracting mobility from NEGF calculations that will be discussed is using the resistance scaling analysis (Frey et al., 2011; Luisier, 2011; Aldegunde et al., 2011; Nguyen et al., 2013; Rhyner & Luisier, 2013; Nguyen et al., 2014). Niquet et al. (2014) presented an approach that extracts the diffusive mobility from quantum transport calculations of nanowire FETs and avoids making approximations of the contact and ballistic resistances. They noted that while this approach avoids uncontrolled approximations, it is only valid under the condition of the channel being “long-enough” such that the intrinsic diffusive processes are well represented within the simulation domain. As devices shrink, the scattering processes may deviate in character from those of macroscopic devices. In this method, one fits the resistance R in the device calculated via Ohms law to the following equation:

$$R(L) = R_c + R_B + \frac{L}{n\mu e}, \quad (5.10)$$

where L is the device length, n is the average carrier density in the SL, e the fundamental charge, and R_c and R_B are the contact and ballistic resistances, respectively. For the model to be valid, the resistance must vary linearly with the simulated SL length and the carrier density in the SL must be consistent between calculations. If so, we can extract the diffusive mobility from the slope of the resistance curve according to Eq. (5.10).

As previously stated, this method for calculating mobility requires that the structure be “long enough” such that the mobility exhibits diffusive transport behavior resulting in the extraction of the intrinsic mobility. Given that hole transport has more diffusive character

than electrons, we analyzed the results for hole mobility first, as the interpretation of the results was more straightforward. Fig. 5.14 depicts the RA product and hole density in the SL as a function of simulation size in the growth direction for an electric field of 100 V cm^{-1} at temperatures of 30 K and 77 K.

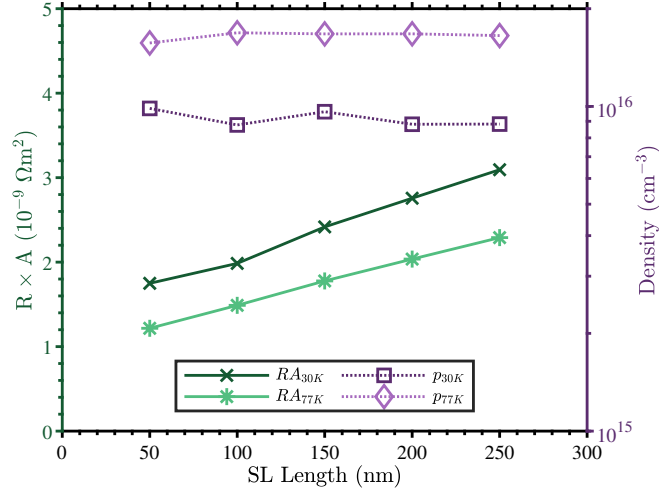


Figure 5.14: The resistance-area product (green lines) and hole density (purple dotted lines), respectively, calculated for majority holes as a function of simulation size at temperatures of 30 K and 77 K. Linear regression on the 30 K (77 K) resistance data gives an R^2 value of 0.994 (0.999). Reprinted with permission from Glennon et al. (2023).

Strong linearity was demonstrated at both temperatures, but the hole density was less consistent at 30 K. We demonstrated the impact that this had on the intrinsic vertical mobility calculation by using the mean, minimum, and maximum hole densities in separate calculations of mobility using Eq. (5.10). We reported the results in Table 5.1.

Table 5.1: The diffusive vertical hole mobility as calculated using the resistance scaling method for a 3/3 ML InAs/GaSb SL at 30 K with an electric field strength of 100 V cm^{-1} using the mean, maximum, and minimum hole densities, respectively, for the data set that includes the 50 nm, 100 nm, 150 nm, 200 nm, and 250 nm calculations. Reprinted with permission from Glennon et al. (2023).

	Mean Density	Max Density	Min Density
Mobility	978	910	1,023

The mobility range suggested by these calculations is only a zero-order approximation. This error estimation does not take into account the impact that varying density may have on the value of the resistance. This will be elaborated on in the discussion of the mobility calculation for electrons later in this section.

To understand how increasing the simulation size affects the calculation, we calculated the diffusive mobility using the mean, maximum, and minimum densities, respectively, for each combination of consecutive pairs of data points. The results are plotted in Fig. 5.15.

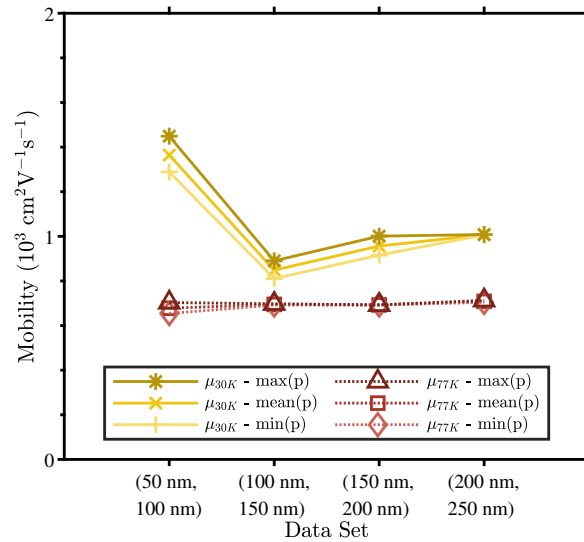


Figure 5.15: The diffusive vertical hole mobility calculated using the resistance scaling method for each combination of pairs of calculations with consecutive simulation sizes at temperatures of 30 K (yellow lines) and 77 K (red dotted lines). The mobility is calculated using three different values for the hole density: the maximum, the mean, and the minimum of the two calculations in the pair. Reprinted with permission from Glennon et al. (2023).

We found that for the 30 K data set both the average and the estimated error range of the mobility varied between pairs due to the density variation between calculations. This was a persistent issue for low temperature calculations which we posited is related to convergence issues with respect to the simulation parameters. These results demonstrated that while the SL appeared to be long enough to achieve a linear resistance with respect to device size,

the density variability may lead to sizable errors in the mobility calculation. These issues persisted for all pairs of simulation sizes excluding the mobility extracted from the 200 nm and 250 nm calculations. As temperature increases, so does the scattering, so we expected the consistency of the hole densities to improve for higher temperature calculations. To demonstrate this, we performed the same analysis at 77 K. The results are included in Fig. 5.15. We found that for all consecutive pairs of calculations the mean and error range for the intrinsic hole mobility were well converged. This demonstrates the validity of this method down to the 50 nm simulation size at 77 K.

In Fig. 5.16 we plotted the intrinsic vertical hole mobility calculated using Eq. (5.10) as a function of temperature with error bars representing the estimated error range.²

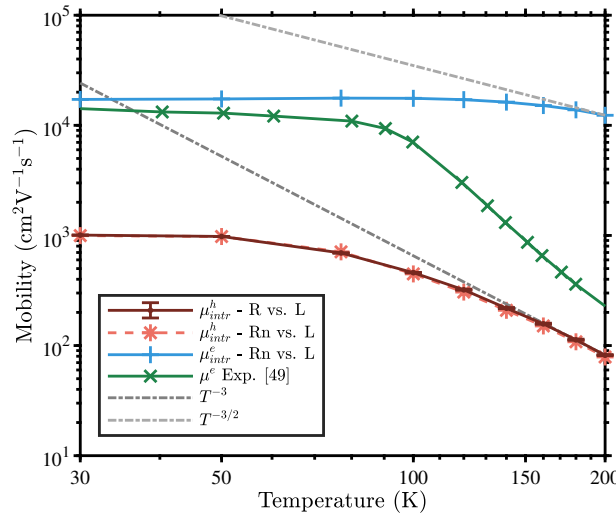


Figure 5.16: The diffusive vertical mobility as a function of temperature for a MWIR InAs/GaSb SL calculated using the resistance scaling method from quantum transport simulations by using Eq. (5.10) (dark red line with error bars) and Eq. (3.98) (light red dashed line with asterisks) for holes. Also plotted is the vertical mobility for electrons calculated using Eq. (5.10) (blue line with pluses). Finally, the experimentally obtained electron vertical mobility as a function of temperature (green line with x's) for a 4.3 μm LWIR SL as reported by Swartz & Myers (2014). Reprinted with permission from Glennon et al. (2023).

²We used the data from the 100 nm, 150 nm, and 200 nm simulations for mobility at 77 K and the 200 nm and 250 nm simulations for that below 77 K.

The small error bars throughout the temperature range demonstrate the consistency of the density in the simulations used to calculate the mobility, suggesting that the results are valid.

We found that the electron transport in this SL was more coherent in nature than the hole transport. Unlike the resistance in the hole calculations, the resistance in the electron calculations did not depend linearly on simulation size in the 100 - 400 nm range for an electric field strength of 100 V cm^{-1} . Thus, we increased the electric field strength to $2,000 \text{ V cm}^{-1}$ for our vertical electron mobility calculations. Fig. 5.17 presents the RA product for electrons as a function of simulation size.

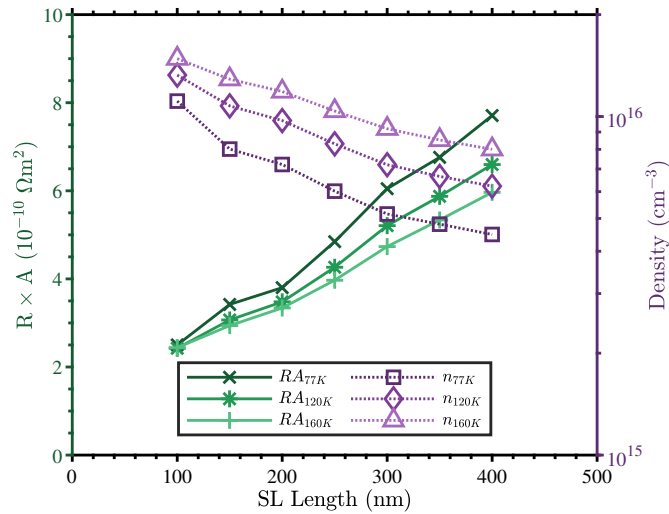


Figure 5.17: The resistance-area product (green lines) and electron density (purple dotted lines), respectively, calculated for majority electrons as a function of simulation size at temperatures of 77 K, 120 K, and 160 K. Linear regression on the resistance results in R^2 values of 0.990, 0.992, and 0.993, respectively. Reprinted with permission from Glennon et al. (2023).

The strong linearity suggests that the resistance scaling method may be valid at this electric field strength for electrons at temperatures of 77 K and above. However, we found that the calculated electron density decreased monotonically with increasing simulation size. If this affect is not accounted for, the calculated mobility can have substantial error. To

compensate for the inconsistent density, we used Eq. (3.98). In Fig. 5.18 we presented the nRA product as a function of simulation size for different temperatures.

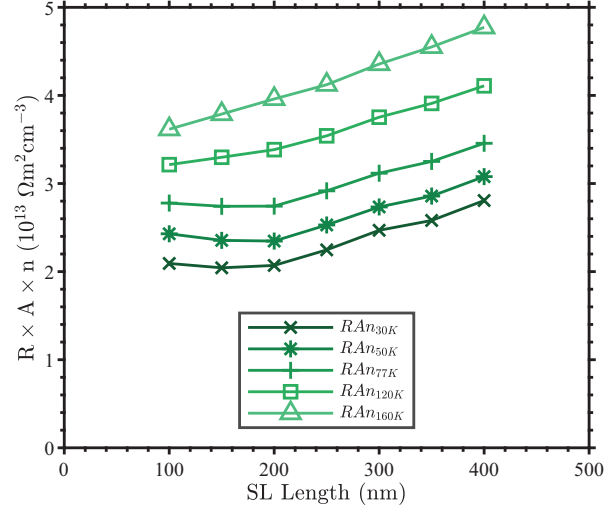


Figure 5.18: The resistance-area-density product calculated for majority electrons as a function of simulation size at several temperatures. Linear regression was performed on the calculations with lengths of 200nm and greater returning R^2 values of 0.992, 0.995, 0.997, 0.998, and 0.997, respectively, suggesting that valid mobility may be extracted using Eq. (3.98). Reprinted with permission from Glennon et al. (2023).

These results demonstrated that linearity was achieved for each temperature with calculation lengths of 200nm or larger. However, the nRA product deviates from linearity for smaller simulations. We found that the cause of this behavior was evident in the behavior of POP scattering. Given that the electron transport was largely ballistic, the existence of high LDOS at an energy level below the left reservoir Fermi level by the POP scattering energy was required for significant scattering to occur. For the 200nm simulations, in which linearity of resistance began, the Fermi levels of the left and right reservoirs were offset by 40meV which was larger than the POP scattering energy chosen for the scattering self-energy (30meV) resulting in enhanced scattering.

This enhanced scattering was sufficient to impose linear scaling behavior on the calculated resistance. To demonstrate, we included the spatially resolved spectral current as well

as the scattering rate associated with POP scattering for 200nm simulations of electrons and holes at 77 K in Fig. 5.19.

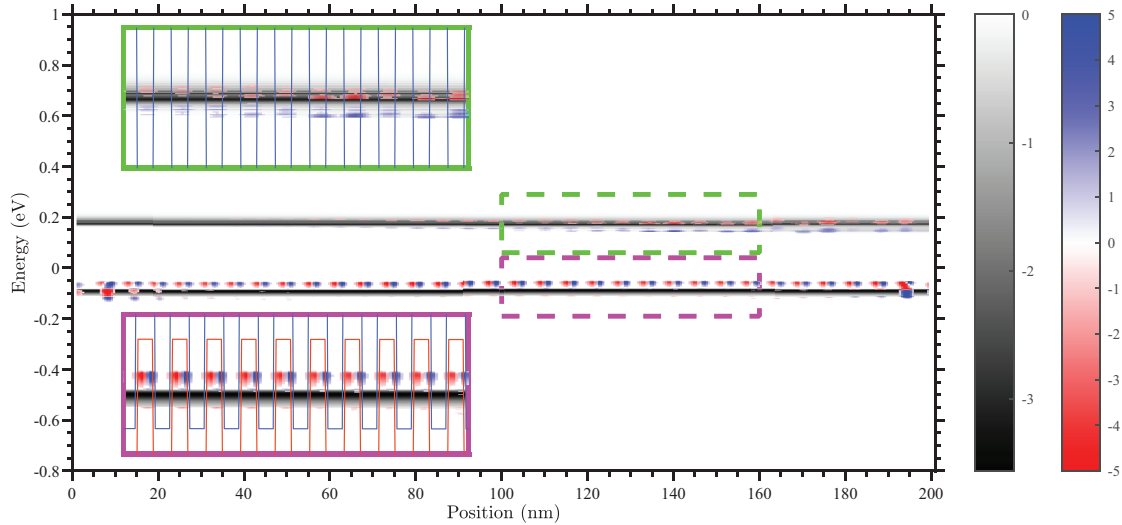


Figure 5.19: The electron (data at higher energy levels) and hole (data at lower energy levels) spatially resolved spectral currents (in 10^6 Acm^{-2} and 10^4 Acm^{-2} , respectively) and scattering rates (in $10^{26} \text{ s}^{-1}\text{cm}^{-3}$ and $10^{24} \text{ s}^{-1}\text{cm}^{-3}$, respectively) associated with POP scattering for a 200nm simulation at 77 K. POP scattering is size-dependent for electrons, but nearly size-independent for holes at this scale. Note that this figure is a composite plot of two separate calculations, one for electrons and one for holes, with electric field strengths of 100 V cm^{-1} and $2,000 \text{ V cm}^{-1}$, respectively. Thus, the SL band diagrams were only included in the two insets as they would conflict in the composite plot. (The spectral currents are displayed in a gray scale color map while the POP scattering rates are displayed in a blue/red color map.) Reprinted with permission from Glennon et al. (2023).

Electrons entering from the left reservoir were shown to have conducted via ballistic transport throughout most of the structure resulting in low scattering rates. However, they scattered into lower energy states near the right reservoir which was exemplified by high scattering rates. This was also visible in the spatially resolved spectral current for electrons where the spectral current was nearly constant with respect to energy from left to right across the structure while demonstrating current at lower energy near the right reservoir; see inset of Fig. 5.19. For shorter simulation sizes, fewer states were available for the elec-

trons to scatter into resulting in reduced POP scattering. It is worth noting that we found evidence that the requirement of an approximately 40 meV difference in contact Fermi levels to achieve linear resistance scaling may be independent of electric field strength and simulation size (see Supplemental Material of Glennon et al. (2023)). On the contrary, we compared the POP scattering rates with the spectral current for holes, and demonstrated that holes were scattering into and out of virtual states at energies above the hole miniband. Thus, POP scattering of holes was quasi-periodic away from the reservoirs. This demonstrated that POP scattering of holes far from the reservoirs was consistent for much smaller simulations. Similar plots for different simulation sizes were provided in the Supplemental Material of Glennon et al. (2023).

In Fig. 5.16, we included the diffusive vertical electron mobility calculated via Eq. (3.98) as a function of temperature using the nRA product data that had achieved strong linearity.³ These results were plotted alongside the experimental vertical electron mobility as a function of temperature reported by Swartz & Myers (2014) for a nearly $4.3\mu\text{m}$ SL layer. The calculated diffusive electron mobility was significantly higher than the apparent mobility calculated in Section 5.4.1 using the average velocity method which confirmed that electron transport was highly coherent in these simulations. This was consistent with the results of the analyses from Section 5.4.1 and Section 5.4.2. The low temperature electron mobility was of the same order of magnitude as the experimental data (see Fig. 5.16), but the high temperature experimental mobility was orders of magnitude lower. As we mentioned in Section 5.4.1, this mobility degradation was likely due to specific structural details of the experimental device that were not included in the simulations.

For completeness, we compared the diffusive vertical hole mobility calculated as a

³Specifically, we used the data from the calculations with lengths of 200 nm, 250 nm, 300 nm, 350 nm, and 400 nm.

function of temperature via Eq. (3.98)⁴ with that of Eq. (5.10) and included the results in Fig. 5.16. We found that the percent difference of the diffusive mobility calculated using both methods was less than 5% in magnitude. While this suggests that the assumptions implicit to Eq. (3.98) are reasonable for holes at these temperatures, we cannot be certain that the assumptions hold for electrons.

5.5 MOBILITY METHODS RESULTS COMPARISON

As demonstrated in Section 5.4.1, the average velocity method calculates the apparent mobility. On the other hand, the resistance scaling analysis method calculates the diffusive mobility. We related these two different components by using Eq. (5.11) to extract an expression for the conceptual ballistic mobility that represents the $R_c + R_B$ component of the total resistance in Eq. (5.10) which resulted in the following relation: (Luisier, 2011)

$$\mu_{ball} = \frac{L}{ne(R_C + R_0)}. \quad (5.11)$$

Using this equation, along with Matthiessens rule (Eq. (5.1)), we calculated an effective apparent mobility by combining this approximate ballistic mobility with the diffusive mobility calculated via Eq. (3.98). In Fig. 5.20, we presented the results of this new apparent mobility along with the apparent mobility calculated using the average velocity method.

⁴We used the data from the 100 nm, 150 nm, and 200 nm simulations for mobility at 77 K and the 200 nm and 250 nm simulations for that below 77 K.

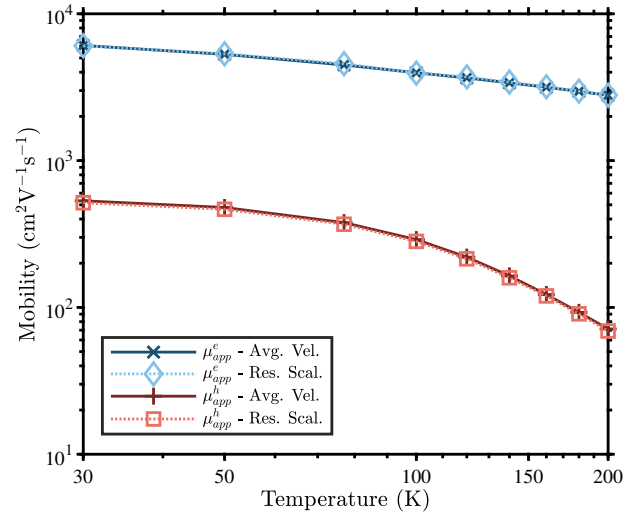


Figure 5.20: The electron (dark blue line with x's) and hole (dark blue line with pluses) apparent vertical mobility plotted as a function of temperature calculated using the average velocity method. Also, the apparent vertical mobility calculated by combining diffusive and ballistic components using Matthiessen's rule derived from resistance scaling analysis for electrons (light blue dotted line with diamonds) and holes (light red dotted line with squares). These results correspond with simulation sizes of 200nm. Reprinted with permission from Glennon et al. (2023).

We found that the resistance scaling method results and the average velocity method results were consistent with each other throughout the temperature range investigated for both electrons and holes. This confirms that the average velocity method calculates an apparent mobility which encompasses diffusive and ballistic effects.

Additionally, we compared the ballistic approximation method with the resistance scaling analysis as both methods attempt to extract the diffusive mobility. Fig. 5.21 presents the mobility calculated using both methods for electrons and holes.

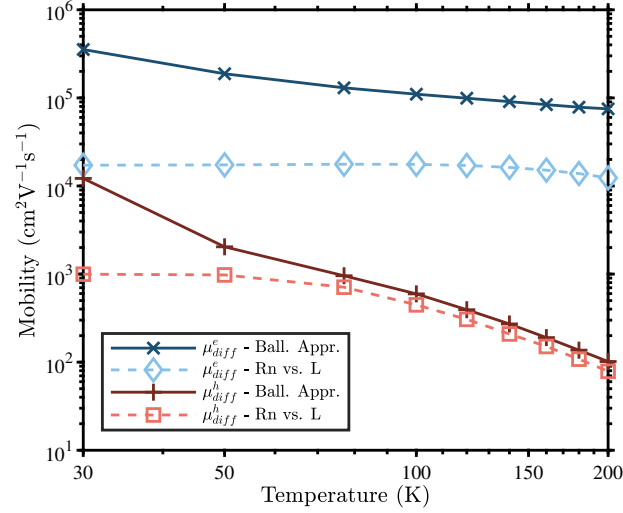


Figure 5.21: The diffusive vertical electron and hole mobility as a function of temperature calculated using both resistance scaling analysis (Eq. (3.98)) and the ballistic approximation method (Eq. (5.1)) from 200 nm simulations. Reprinted with permission from Glennon et al. (2023).

We found that the ballistic approximation method compares favorably to the resistance scaling method for holes at temperatures above 100 K, which demonstrates that the inherent approximations of the ballistic approximation method may be reasonable. However, at lower temperatures the results for holes were inconsistent. Those for electrons differ dramatically throughout the entire temperature range. This bolstered our determination that the ballistic approximation method is more ambiguous than the resistance scaling methodology, in which the validity of the method is determined via the linearity of the resistance.

5.6 CONCLUSION

In summary, the results of the analysis of mobility extraction methodologies from NEGF calculations from our previous work in Glennon et al. (2023) were presented. It was demonstrated that when trying to predict the mobility for a large T2SL-based device one should avoid using a method that calculates the apparent mobility, which includes effects related

to the ballistic resistance, like calculating the mobility from the average drift velocity (Section 5.4.1). Rather, it is important to use a method that extracts the diffusive mobility. These include the ballistic approximation (Section 5.4.2) and resistance scaling (Section 5.4.3) methodologies. Of these, it is demonstrated that resistance scaling requires fewer uncontrolled assumptions. Finally, we validated the use of the method described by Eq. 3.98 for the use of extracting the vertical hole mobility, that is utilized throughout Chapter 6 and Chapter 7 to predict the properties of advanced T2SL material systems.

CHAPTER 6

Effect of Disorder and Strain on the Vertical Hole Mobility in MWIR T2SL-based Curved Focal Plane Arrays

The bulk of the work presented in this chapter has been published in Glennon et al. (2024) and Glennon & Bellotti (2023), for the InAs/InAsSb and InAs/GaSb results, respectively. The details have been reproduced and repurposed to serve the overall narrative of this dissertation.

6.1 INTRODUCTION

Having validated the use of Eq 3.98 for predicting the vertical hole mobility for type-II superlattice (T2SL) structures, it is now possible to utilize this method for the prediction of mobility for advanced T2SL material systems. One such system is associated with an emerging device architecture for the improvement of imaging sensors: the curved focal-plane array (cFPA) (Rim et al., 2008). The motivation for this design comes from the desire to reduce the complexity of the optical system. Traditional flat FPA architectures require large optical systems to achieve field flattening while minimizing aberrations that effect image quality (Rogalski et al., 2016). However, utilizing curved FPA architectures can remove the need for field flattening leading to simpler optical designs. Recently, the development of a method for curving photographic sensors in visible-light cameras has resulted in a cFPA with improved resolution and nearly uniform illumination compared with professional camera systems with similar lenses, while reducing the size, weight, and cost of the optical system (Guenter et al., 2017). This method is applicable to infrared (IR) FPAs as well and can be expected to similarly improve device performance (O'Masta et al., 2022). However, it is important to understand the effect that curving has on the underlying material properties. Curving the FPA will introduce additional strain throughout

the material structure which can affect carrier transport. A recent study has investigated the impact that the curving of an FPA will have on the band gap of bulk InAsSb absorber layers (Kyrtos et al., 2021). A natural extension of this investigation would be to study the properties of additional IR materials, like T2SLs, under strained conditions.

In the following sections, the results of NEGF calculations of two different mid-wave (MWIR) superlattice (SL) structures (Ga-free and Ga-based) that we performed across two investigations (Glennon & Bellotti, 2023; Glennon et al., 2024) will be presented. These studies focused on the impact that structural disorder and external axisymmetric strain in the growth direction had on the vertical hole mobility, and elaborated on the implications these effects may have on device performance. The chapter is organized as follows: the T2SL material structures will be elaborated on in Section 6.2, the geometry of the theoretical cFPA will be described in Section 6.3, the effects that SL disorder and external strain have on the vertical hole mobility will be described in Section 6.4, and finally the subsequent impact on this may have on the QE of the cFPA device is elaborated on in Section 6.5.

6.2 SUPERLATTICE STRUCTURES

As discussed in Section 2.3, Ga-free and Ga-based T2SLs have been demonstrated as potential materials for use in IR sensors. We chose to investigate both materials for use in a theoretical MWIR cFPA. In Section 6.2.1 and Section 6.2.2, the specific Ga-free and Ga-based structures that we investigated, respectively, will be described.

6.2.1 InAs/InAsSb Structure

We chose a MWIR InAs/InAsSb SL with layer thicknesses of 15 and 4 monolayer (ML), respectively, lattice-matched to a GaSb substrate. We studied both a structure with ideal interfaces as well as graded. The composition of the ternary alloy differs between the two.

This is due to the fact the the graded band diagram results in a different degree of confinement for the charge carriers. While keeping the layer thicknesses the same between both structures, variation on the ternary alloy composition was necessary to achieve the same cutoff wavelength. For ideal interfaces, the ternary alloy was selected as $\text{InAs}_{0.65}\text{Sb}_{0.35}$, which resulted in a cutoff wavelength of approximately $5\mu\text{m}$. The electronic structure of this SL, as calculated using the 4×4 $k \cdot p$ model with Bloch boundary conditions, was provided in Fig. 6.1a.

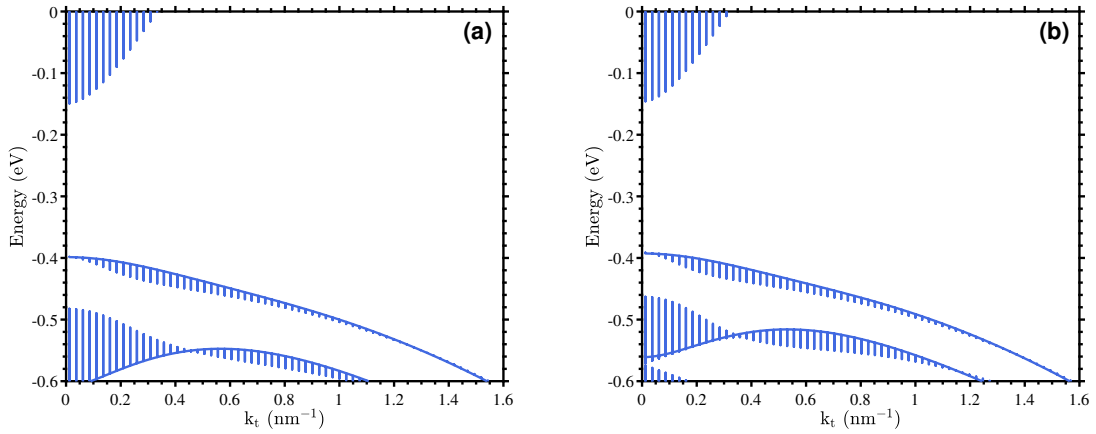


Figure 6.1: The energy band structure of the SL structure with (a) ideal and (b) graded interfaces calculated as a function of the transverse wave vector. It is modified with vertical lines representing the dispersion in the vertical wave vector.

The dispersion in the growth direction is plotted with branching vertical lines that represent the dispersion in the growth direction for the corresponding in-plane wave number k_t . Thus, the vertical lines provide an estimate for the miniband width. We found that the top hole miniband was narrow which suggests that the vertical hole mobility may be low even for the ideal case. (Ting et al., 2016)

To model a realistic SL structure (i.e. one with graded interfaces and disorder) we expanded upon the “compositional-disorder” model presented in Bellotti et al. (2021), but instead we incorporated the Muraki Antimony (Sb) segregation model (Muraki et al., 1992)

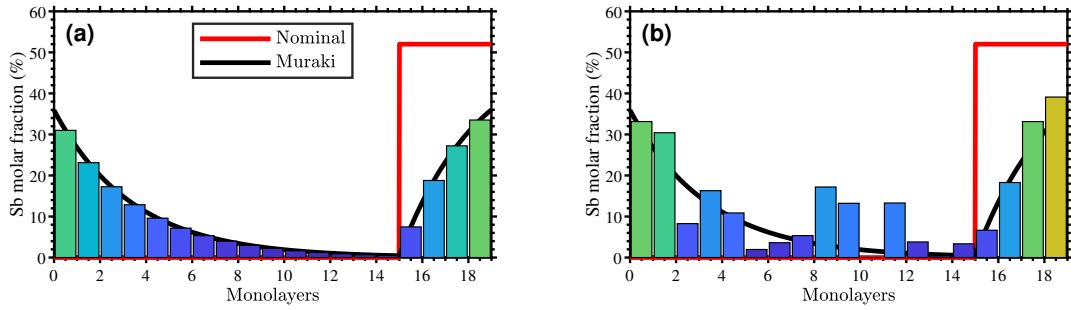


Figure 6.2: The Sb concentration profile of an MWIR InAs/InAsSb SL. The nominal (red line) and graded (black line) concentration profiles are plotted along with the actual profile represented by bar plot with one bar per spatial mesh node in the case of (a) no disorder and (b) disorder. Note, the nominal profile demonstrates the Sb concentration of the Muraki model SL if no Sb segregation occurred. This is a different ternary alloy composition than that of the ideal SL that was also investigated. Reprinted with permission from Glennon et al. (2024).

with the parameters presented in Kim et al. (2018), to model the Sb concentration profile for one SL period. Fig. 6.2a presents the Sb concentration profile for one SL period based on the Muraki model. It was demonstrated that a substantial concentration of Sb migrates from the ternary alloy layer to the binary layer, which is consistent with experimentally grown Ga-free SLs (Kim et al., 2018). The electronic structure of the graded SL is also included in Fig. 6.1b. The band structure of the graded structure is very similar to that of the ideal structure; however, it is worth noting that the dispersion on the growth direction at finite transverse wave vectors is slightly greater, suggesting better hole transport properties.

To include disorder, we selected a random number from a normal distribution of Sb concentration with a mean of zero and a chosen standard deviation. We investigated three different graded model structures with disorder selected from standard deviations of 0% (no disorder), 2% and 4% nominal Sb compositions, respectively, resulting in three different magnitudes of disorder. This value was added to the Sb concentration profile, as defined in Fig. 6.2a, at each node. Throughout the rest of this chapter, these three structures will be referred to as “no”, “low”, and “high” disorder SLs. Fig. 6.2b presents one example

of a high disorder Sb concentration profile for one SL period. We chose $\text{InAs}_{0.48}\text{Sb}_{0.52}$ as the “desired” ternary alloy composition of the disordered structures. The reason for the increase in the Sb composition compared with the ideal SL is that, as shown in Fig. 6.2, the actual Sb composition of the ternary layer is lower as Sb migrates into the binary layer during growth. Thus, there is a reduction in the band offsets between the peak and trough of the SL band structure for both the valence band (VB) and conduction band (CB). A higher Sb concentration is required to compensate for this effect to produce the same band gap. In Fig. 6.3, we computed the energy gaps of 100 random unit cells with compositional disorder, each of which is generated by the periodic repetition of the unique SL period. The resulting distribution of subsequent cutoff wavelengths was centered around approximately $5\mu\text{m}$ for both the low and high disorder cases for the $\text{InAs}_{0.48}\text{Sb}_{0.52}$ lattice.

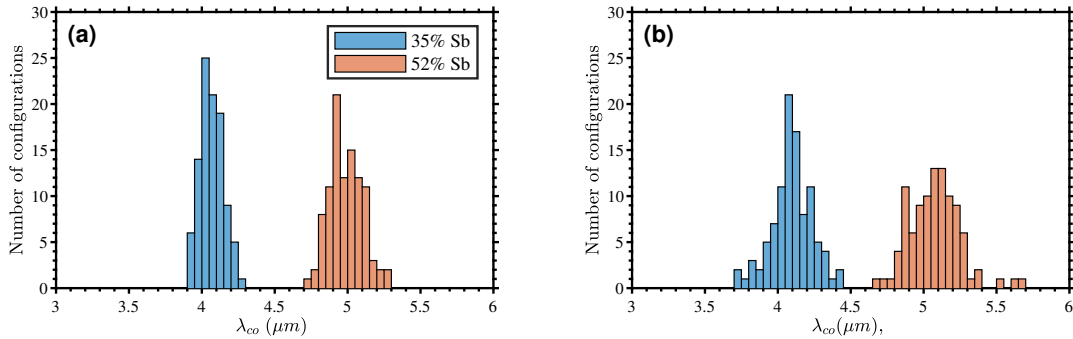


Figure 6.3: Histogram of the cutoff wavelengths calculated for (a) low and (b) high disorder SLs with ternary alloy layer compositions of $\text{InAs}_{0.65}\text{Sb}_{0.35}$ and $\text{InAs}_{0.48}\text{Sb}_{0.52}$. Reprinted with permission from Glennon et al. (2024).

We also found that a choice of $\text{InAs}_{0.65}\text{Sb}_{0.35}$, as in the ideal lattice, using the graded model with disorder resulted in larger band gaps, which is evidence of the reduced band structure offsets between the constituent “layers”. Thus, the final selection of structures included the ideal structure with no disorder and the graded structure with no, low, and high disorder. We simulated carrier transport using NEGF calculations on finite-sized SL

models terminated on each side by open boundary conditions, which act as semi-infinite contact regions. The details of the NEGF model are described in Chapter 3. To allow for unimpeded hole transport on both sides of the SL we chose the InAsSb layer for the contact material. In the case of the disordered SLs, this amounts to an ideal InAsSb layer that matches the “desired” Sb concentration selected for the Muraki model. Additionally, we selected an electric field strength of 100V/cm. Examples of the band diagrams for each of these structures, with a total simulation domain size of approximately 120 nm each, were presented in Fig. 6.4.

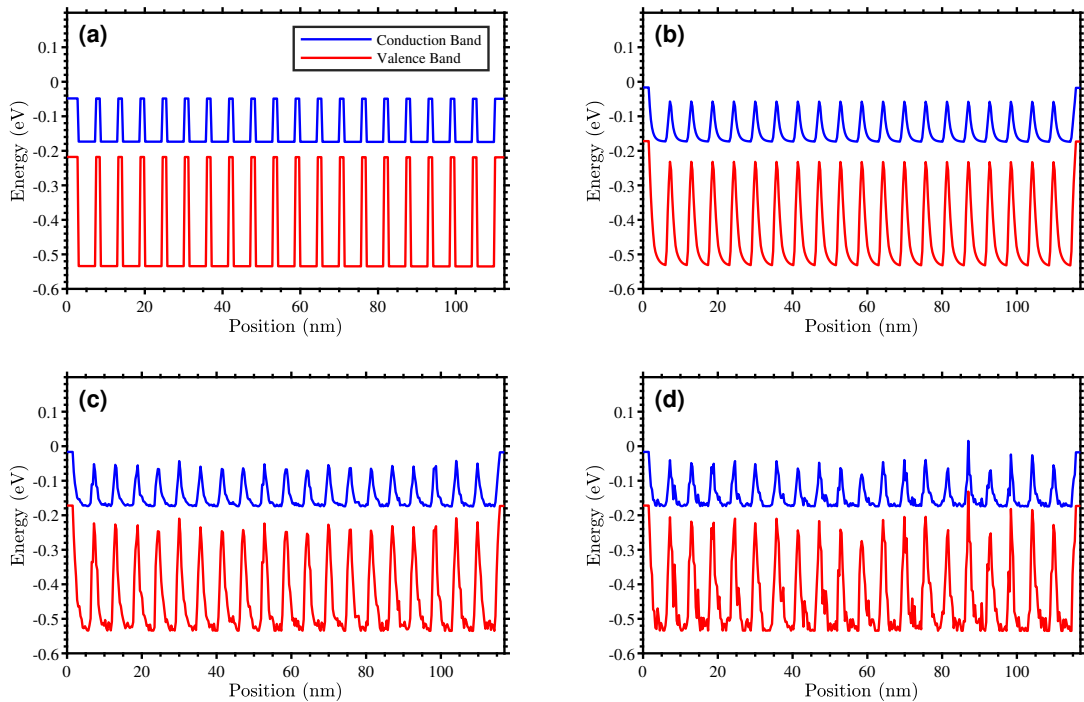


Figure 6.4: Band diagrams of the (a) ideal, (b) no disorder, (c) low disorder, and (d) high disorder ga-free SLs for the simulations with domain size of approximately 120 nm. Reprinted with permission from Glennon et al. (2024).

The increasing disorder is evident when comparing the no disorder (Fig. 6.4b), low disorder (Fig. 6.4c), and high disorder (Fig. 6.4d) structures.

6.2.2 InAs/GaSb Structure

We utilized a similar strategy for the Ga-based SL as in the Ga-free SL (section 6.2.1), including an ideal SL model as well as a modified version of the Muraki segregation model (Muraki et al., 1992) to introduce graded interfaces. To simplify this model, we treated the material as a $\text{GaSb}_{1-x}\text{InAs}_x$ quaternary alloy system where the band structure parameters are linearly interpolated between the binary alloys. Then, we took the mean of the segregation efficiencies of In and Sb at the GaSb-InAs (IF1) and InAs-GaSb (IF2) interfaces provided in Li et al. (2017) which were 0.625 and 0.565, respectively. Thus, we developed a simple model for the segregation of GaSb into InAs, and vice versa.

We chose two slightly different SL designs for the ideal and modified Muraki structures in order to achieve a consistent cutoff of $5\ \mu\text{m}$ between the two models. The ideal and modified Muraki structures were 8/13 ML and 10/13 ML InAs/GaSb, respectively. Fig. 6.5 presents the calculated SL band structure of the ideal and non-disordered modified-Muraki structures using Bloch boundary conditions.

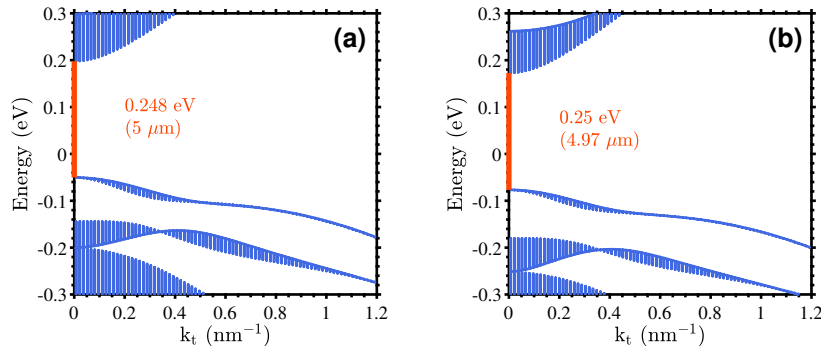


Figure 6.5: Calculated band structure of one SL period of the (a) ideal and modified-(b) Muraki structures without disorder. The cutoff wavelengths of each structure are nearly identical at $5\ \mu\text{m}$. Reprinted with permission from Glennon & Bellotti (2023).

It is demonstrated that the cutoff wavelengths were nearly the same for both Ga-based

structures, as well as being similar to those of the Ga-free structures (Fig. 6.1).

Additionally, this modified Muraki model allows for the straightforward inclusion of disorder which is consistent with the Ga-free SL, in which we randomly selected an alloy composition x from a normal distribution centered at 0% with the same standard deviation values as with section 6.2.1. Examples of one SL period of the modified-Muraki alloy composition profile, with and without disorder, are provided in Figs. 6.6b and 6.6a, respectively.

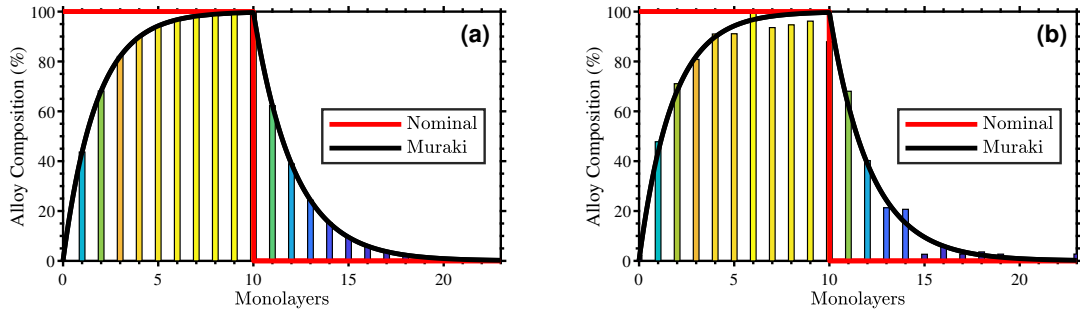


Figure 6.6: Examples of the $\text{InAs}_{1-x}\text{GaSb}_x$ alloy composition profile (colorbar) for one SL period of the modified-Muraki structure in the case of (a) no disorder and (b) disorder as a function of spatial node. The nominal and modified-Muraki alloy composition profiles are overlaid on top to demonstrate the impact that atomic incorporation and disorder have on the intended SL structure. Reprinted with permission from Glennon & Bellotti (2023).

The final selection of structures included the ideal structure with no disorder and the graded structure with no, low, and high disorder, which is commensurate with the investigation of the Ga-free SL. To calculate the mobility we analyzed NEGF simulations with sizes of approximately 120 nm and 240 nm that consist of repetitions of the band structure between two GaSb contact regions. The GaSb contacts blocked the conduction of electrons allowing for unimpeded transport of holes on both sides of the simulation. Examples of the band diagram for each of these, with a total simulation domain size of approximately 120 nm each, were presented in Fig. 6.7.

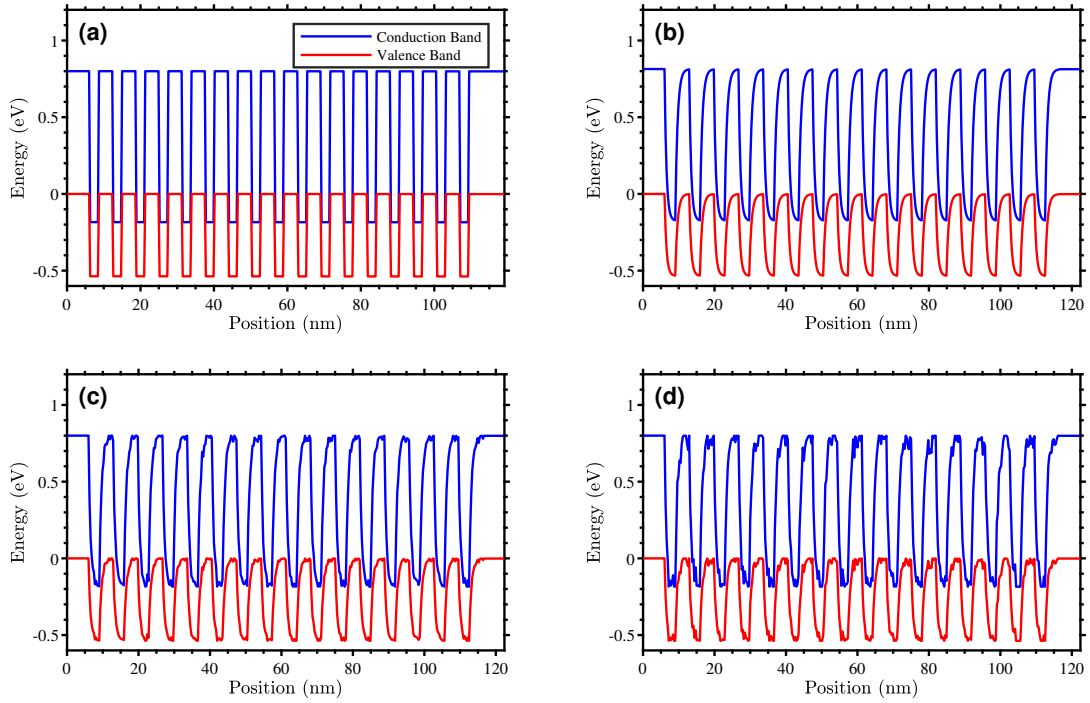


Figure 6.7: Band diagrams of the (a) ideal, (b) no disorder, (c) low disorder, and (d) high disorder Ga-based SLs for the simulations with domain size of approximately 120 nm. Partially reprinted with permission from Glennon & Bellotti (2023).

6.3 FPA DEVICE GEOMETRY

We used the ABAQUS/STANDARD (Smith, 2009) model described in Kyrtos et al. (2021) to perform a FEA simulation of the strain configuration induced in the curving of an FPA. The mechanical model in the manuscript was for a bulk $\text{InAs}_{0.91}\text{Sb}_{0.09}$ absorber (Kyrtos et al., 2021). While in our case we were modeling a SL, the microscopic scale of the SL structure is not possible to include in the macroscopic die displacement model, so we chose to model the SL as a bulk alloy with an average composition of $\text{InAs}_{0.89}\text{Sb}_{0.11}$. However, as mentioned in Kyrtos et al. (2021), the difference in the strain configuration calculated for $\text{InAs}_{0.82}\text{Sb}_{0.18}$ versus $\text{InAs}_{0.91}\text{Sb}_{0.09}$ was insignificant. Thus, we chose the strain configuration calculated for the $\text{InAs}_{0.91}\text{Sb}_{0.09}$ alloy. The die was modeled as a $45 \text{ mm} \times 50 \text{ mm}$

rectangular deformable part with a thickness of $100\mu\text{m}$. The displacement of the die surface was dictated directly in the simulation, forcing the initially flat die into a spherical segment with a prescribed ROC of 70 mm, which is representative of a curved-FPA.

Strain induced by the curving of the FPA was included in the band structure model via the principle of superposition of linear elasticity in which the curving induced strain was added to the strain induced in the SL due to lattice matching to GaSb. The strain in the active material had four non-zero components, namely $\vec{S} = \{\epsilon_{xx}, \epsilon_{yy}, \epsilon_{zz}, \gamma_{xy}\}$, which depended upon the physical x , y , and z coordinates of the die, with the x and y direction being transverse to the SL plane and z being in the growth direction. The strain components extracted from the FEA simulation are presented in Fig. 6.8.

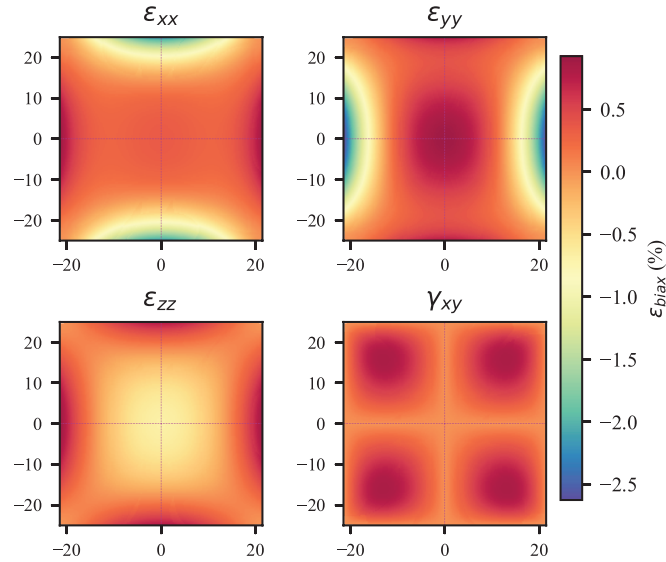


Figure 6.8: The components of the strain vector $\vec{S} = \{\epsilon_{xx}, \epsilon_{yy}, \epsilon_{zz}, \gamma_{xy}\}$ extracted from a FEA calculation of a $45\text{ mm} \times 50\text{ mm} \times 100\mu\text{m}$ InAsSb die curved to an ROC of 70 mm.

However, as mentioned in Chapter 3, the transport model used in this investigation was based on the axial approximation, with an axisymmetric strain, ϵ_{biax} , and a resultant strain

in the growth direction given by the following equation: (Kyrtos et al., 2021)

$$\epsilon_{zz} = -2 \frac{\nu \epsilon_{biax}}{(1 - \nu)}, \quad (6.1)$$

where ν is the Poisson's ratio. We transformed the strain \vec{S} extracted from the ABAQUS/-STANDARD model to a vector \vec{S}' subject to the condition $\epsilon_{biax} = \epsilon'_{xx} = \epsilon'_{yy}$, resulting in a position dependent strain ϵ_{biax} . Using this biaxial strain vector $\vec{S}_{biax} = \{\epsilon_{biax}, \epsilon_{biax}, -2\nu\epsilon_{biax}/(1 - \nu), 0\}$, we were able to map physical properties extracted from the NEGF calculations to the strain configurations across the FEA model. Thus, it was possible to predict physical properties as a function of the spatial coordinates of the die, facilitating predictions about device performance.

An important caveat that we pointed out is that the requirement of an axisymmetric strain state results in a residual strain $\vec{S}_{res} \equiv \vec{S}' - \vec{S}_{biax} = \{0, 0, 0, \gamma_{xy}'\}$ that was not accounted for by the model. Shear strains are not applicable to the axial approximation Hamiltonian used in this work, and would require substantially greater computational power to implement. Determining the significance of shear strain will require further investigation that is beyond the scope of the present work. Ultimately, it should be viewed as qualitative when mapping the material properties on the curved sensor where the uncertainty increases proportionately with the magnitude of the residual strain vector.

We plotted the projected axisymmetric strain (Eq. (6.1)) colormap for the curved-FPA based on the strain configuration $\{\epsilon_{xx}, \epsilon_{yy}, \epsilon_{zz}, \gamma_{xy}\}$ that was extracted from the FEA calculations (Fig. 6.8) in Fig. 6.9a.

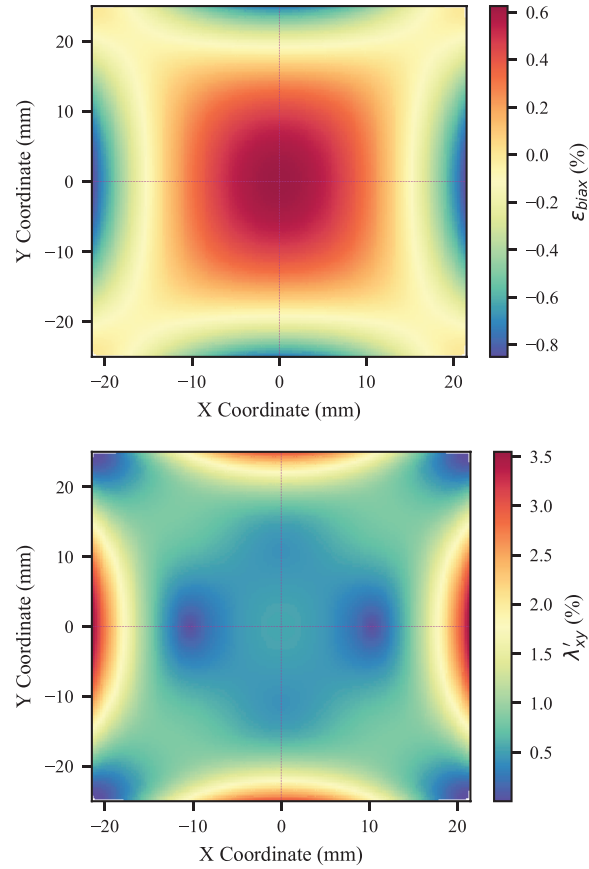


Figure 6.9: The (a) projected axisymmetric strain calculated from the strain configuration extracted from the FEA calculations of a curved-FPA die with a ROC of 70mm presented in Fig. 6.8. Also included is the (b) residual strain component from the transformed strain vector that is not included in the Hamiltonian. Reprinted with permission from Glennon et al. (2024).

In Fig. 6.9b we presented the residual strain component which was excluded from the mapping of the NEGF results to the cFPA coordinates.

6.4 MATERIAL EFFECTS ON HOLE MOBILITY

In this section, the results of the investigation on the effect of SL disorder and external strain on the vertical hole mobility in the Ga-free (section 6.2.1) and Ga-based (section 6.2.2) SLs are presented.

6.4.1 Effect of Disorder

The vertical hole mobility calculated for the ideal, no disorder, low disorder, and high disorder structures are presented in Fig. 6.10a and Fig. 6.10b, respectively.

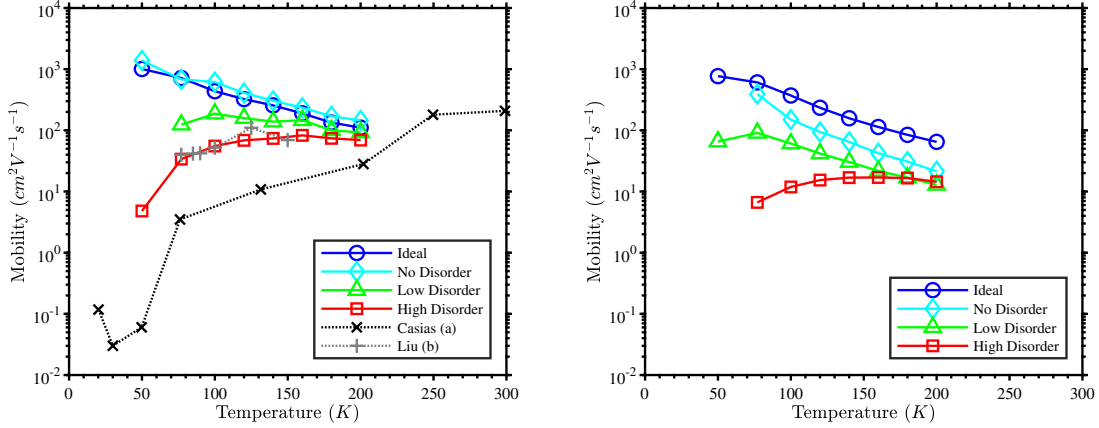


Figure 6.10: The vertical hole mobility calculated as a function of temperature for the ideal (blue line with circles), no disorder (cyan line with diamonds), low disorder (green line with triangles), and high disorder (red line with squares) structures for the (a) Ga-free and (b) Ga-based SLs. Also plotted are experimental results for vertical hole mobility reported in (a) Casias et al. (2020) (black dotted line with x's) and (b) Liu et al. (2022) (gray dotted line with +s) for two different MWIR InAs/InAsSb SLs. Ga-free plot ((a)) is reprinted with permission from Glennon et al. (2024).

Additionally, we include the experimental vertical hole mobility reported by Casias et al. (2020) and Liu et al. (2022) for two different MWIR InAs/InAsSb SLs in Fig. 6.10a. The high disorder simulated results for the Ga-free SL were reasonably close in comparison with the experimental data in Liu et al. (2022). This provided some validity for the selection of the magnitude of disorder. For both the Ga-free SL and the Ga-based SL, when observing the mobility for the no disorder structure and comparing it with that of the structures with increasing disorder, it is evident that an inversion of the temperature dependence at low temperature is instigated by the disorder. This behavior is consistent with the temperature trends observed in experimental data for T2SLs (Olson et al., 2017; Casias et al.,

2020) as well as in the theoretical results reported in Bellotti et al. (2021), suggesting that holes are propagating through the SL by hopping between localized states (Olson et al., 2017; Bertazzi et al., 2020). For the Ga-free structure we noted that the mobility for the no disorder structure is slightly higher than in the ideal structure throughout most of the temperature range. We posited that this is likely due to the graded interfaces that result in less hole confinement, which demonstrates the impact that Sb segregation alone has on the vertical hole mobility. However, for the Ga-based SLs, the ideal structure has the highest mobility. This is most likely a result of having increased the hole barrier layer from 8 ML to 10 ML for the graded structure in order to produce the same band gap. The increased barrier thickness can be expected to result in more localized hole states and lower hole mobility. Lastly, the Ga-based structure exhibited lower hole mobility for all structures, particularly the various graded structures. This is not necessarily an indication of Ga-free structures having better hole mobility than Ga-based structures in general. We chose the specific Ga-based structure to produce an MWIR band gap, but did not attempt to optimize the structure for hole transport. Also, there is no reason to believe that the magnitude of the disorder in Ga-based structures will be the same as that in Ga-free for a realistic sample of grown material. It would require more experimental data about the magnitude of disorder present in both Ga-free and Ga-based structures as well as a comprehensive study aimed at finding Ga-based and Ga-free SL structures optimized for hole transport to make a more definitive statement. In Chapter 7, one such optimization methodology for carrier transport in Ga-free SLs will be presented in Chapter 7.

The effect that the increasing disorder has on hole transport is evident in the relative magnitude, and spectral range, of the hole current spectrum. To demonstrate, we included the spectral current in the 120 nm simulations of the Ga-based ideal, no disorder, low disorder, and high disorder structures at 200 K in Fig. 6.11.

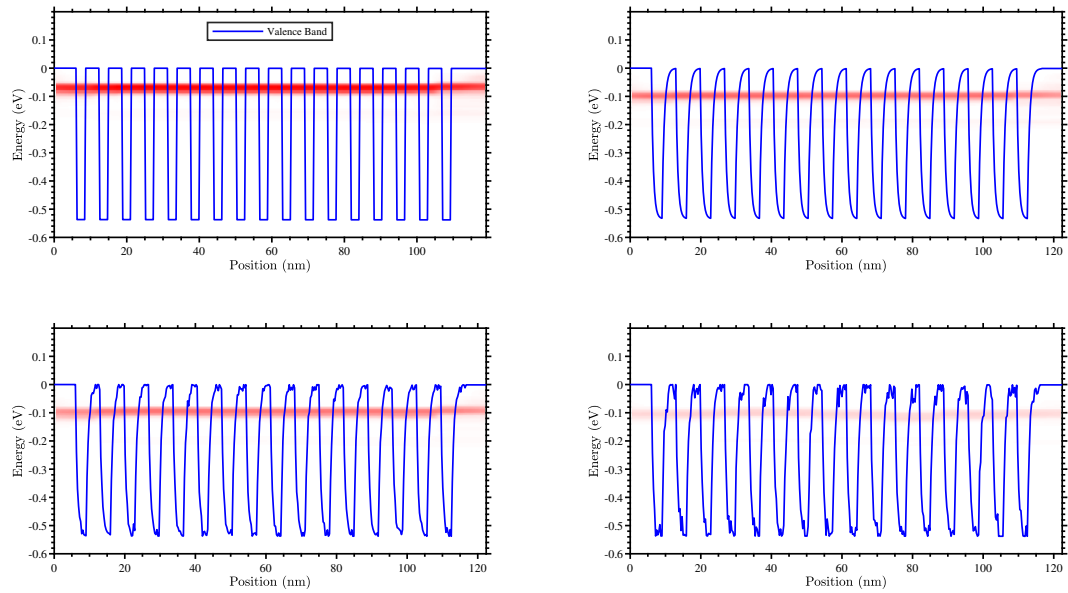


Figure 6.11: The hole current spectrum as a function of position for example structures of the (a) ideal, (b) no disorder, (c) low disorder, and (d) high disorder Ga-based SLs, normalized to the maximum value in the ideal structure, for the simulations with domain size of approximately 120 nm at 200 K. Reprinted with permission from Glennon & Bellotti (2023).

Not only does the magnitude of the hole current spectrum decrease with increasing SL disorder, but the spectral range becomes increasingly discontinuous along the growth direction due to the variation in the confinement across different hole wells. This discontinuous behavior is indicative of scattering in the simulation domain.

6.4.2 Effect of Strain

We investigated a set of axisymmetric strains between -1.2% and $+1.6\%$ calculating the vertical hole mobility as a function of temperature for each strain condition for the Ga-free SL which is presented in Fig. 6.12.

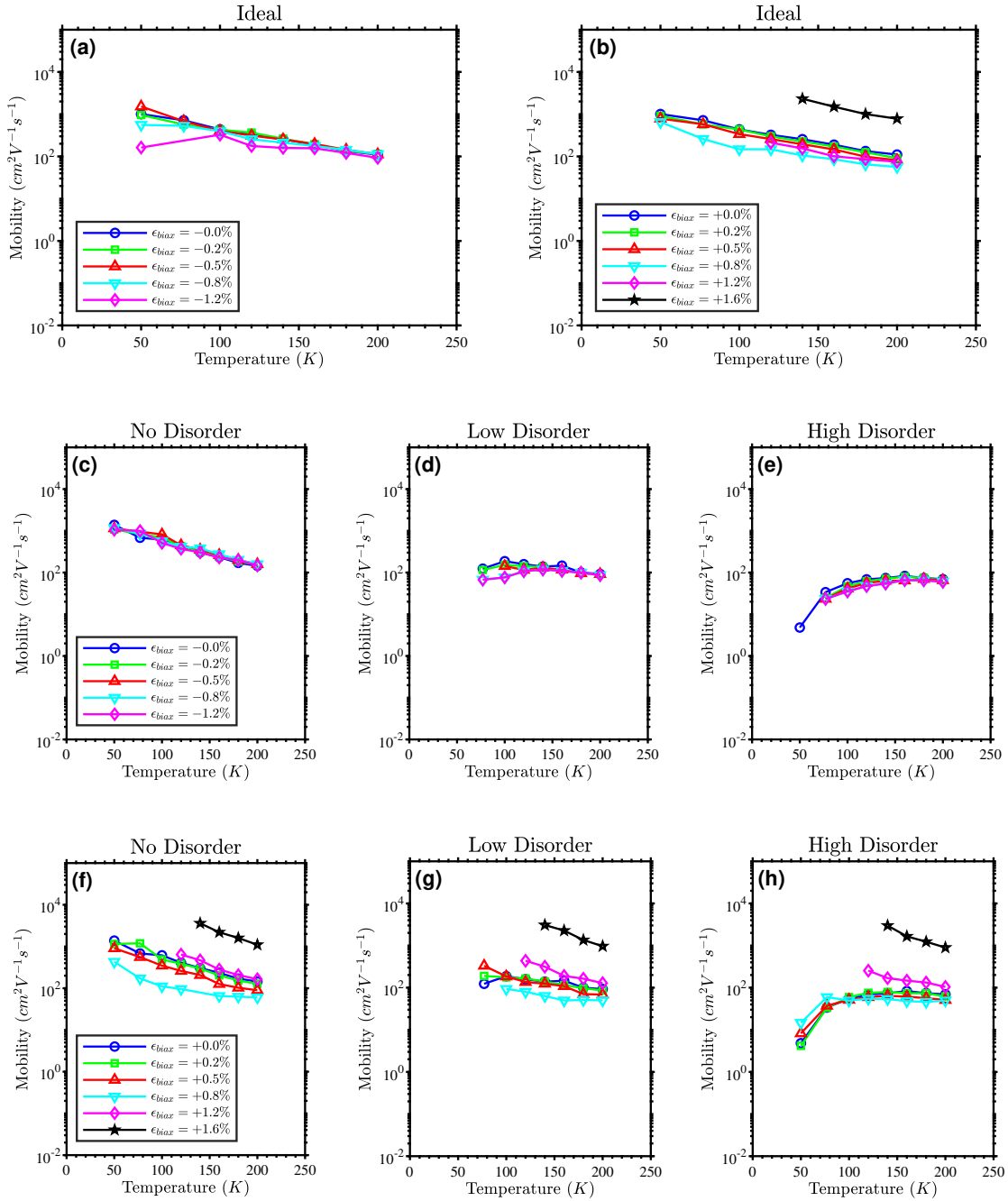


Figure 6.12: The vertical hole mobility calculated as a function of temperature for different magnitudes of negative (positive) axisymmetric strain for the Ga-free (a) (b) ideal, (c) (f) no disorder, (d) (g) low disorder, and (e) (h) high disorder SLs. Reprinted with permission from Glennon et al. (2024).

The disorder-induced inversion of the temperature dependence of the mobility emerged for all external strain values, except for the +1.2% and +1.6% axisymmetric strain cases. For negative axisymmetric strain, particularly at low temperature, the mobility decreased with increasing strain. The reason for this was observed in the calculated band structures with applied strain which are presented in Figs. 6.13c, 6.13b, and 6.13a for axisymmetric strains of 0.0%, -0.5% , and -1.2% , respectively.

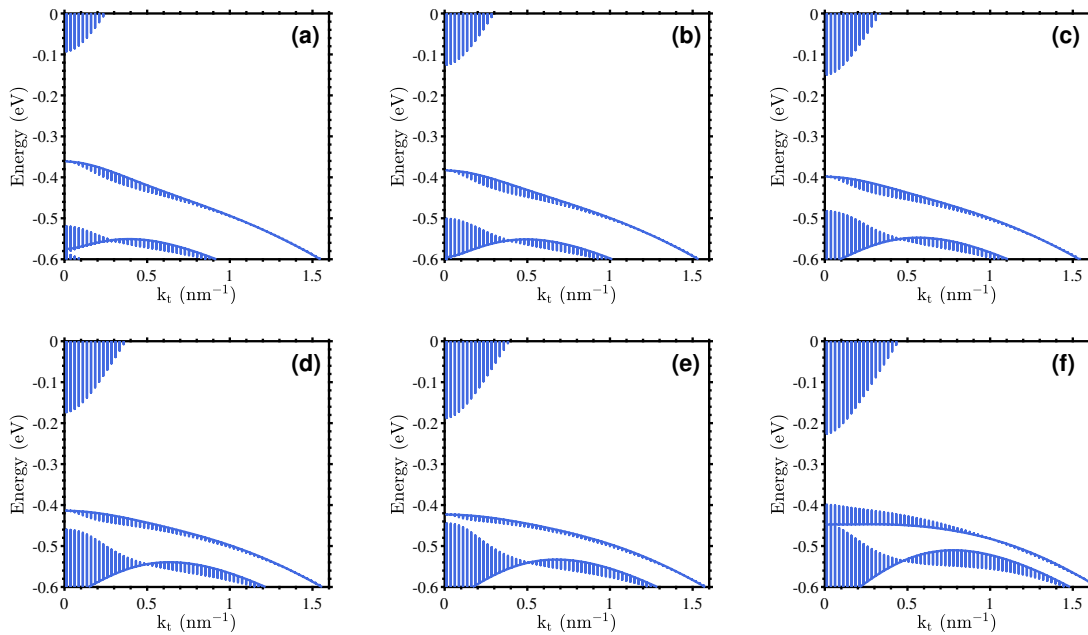


Figure 6.13: The energy band structure of the ideal Ga-free SL calculated as a function of the transverse wave vector for external axisymmetric strains of (a) -1.2% , (b) -0.5% , (c) 0.0% , (d) $+0.5\%$, (e) $+0.8\%$, and (f) $+1.6\%$. It is modified with vertical lines representing the dispersion in the vertical wave vector. Reprinted with permission from Glennon et al. (2024).

As negative strain was applied, the approximate HH miniband size became narrower, due to reduced dispersion in the growth direction, suggesting less favorable hole transport properties. Conversely, the positive axisymmetric case was more complex. For smaller magnitudes of strain, the mobility decreased. However, at strain values of $+1.6\%$ for the ideal and no disorder structures and $+1.2\%$ for the disordered structures, there was an increase

in the mobility over that of the unstrained case. For the +1.6% strain case, there was a substantial increase in the hole mobility. This behavior, while more complex than the negative strain case, can also be explained using the calculated band structure of the strained SL (see Fig. 6.13c, Fig. 6.13d, Fig. 6.13e, and Fig. 6.13f for axisymmetric strains of 0.0%, +0.5%, +0.8%, and +1.6%, respectively). For smaller positive axisymmetric strain, the energy offset between the HH and LH bands got smaller, and the heavy-hole (HH) and light-hole (LH) bands repelled each other. This caused the HH dispersion to increase in the growth direction. The large increase in hole mobility at +1.6% was attributed to an inversion of the HH and LH character near the gamma point due to the axisymmetric strain. The much lower effective mass of the LH band resulted in more favorable hole transport properties. We continued to probe this behavior calculating the vertical hole mobility for each SL type at 120 K with axisymmetric strains of +1.0%, and +1.4%. The results are given in Fig. 6.14a as a function of positive axisymmetric strain.

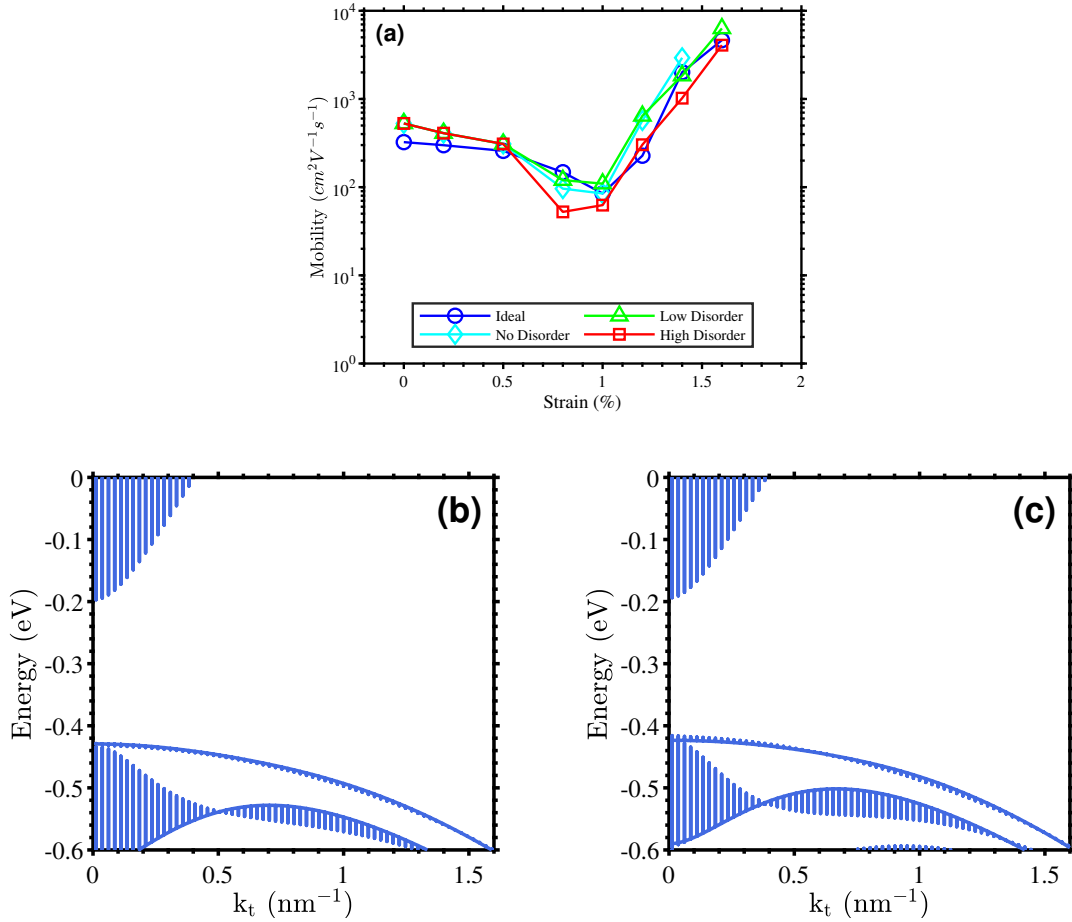


Figure 6.14: The (a) vertical hole mobility calculated as a function of positive axisymmetric strain for each SL structure. Also included are the band structures calculated for the (b) ideal and (c) no disorder SL in which the HH and LH separation is negligible. Reprinted with permission from Glennon et al. (2024).

There was a sharp increase in the mobility above a strain of +1.0%. Additionally, Fig. 6.14b and Fig. 6.14c include the calculated band structures of the ideal and no disorder SLs under +1.0% axisymmetric strain, respectively. We found that at this strain condition the separation between the HH and LH was nearly zero. These results align with our interpretation that the sharp increase in the hole mobility for high positive strains is related to the inversion of the HH and LH bands.

We found that the Ga-based SL structures exhibited similar behavior with respect to the

strain at different levels of disorder. Thus, we opted to forgo the comprehensive analysis performed in Fig. 6.12 for Ga-free SLs. The combined effects of strain and disorder on the QE exhibited throughout a cFPA for either the Ga-free SL or Ga-based SL absorber layers are analyzed and compared in the next section.

6.5 QE IN CURVED FOCAL PLANE ARRAY

To qualitatively probe the performance of the curved-FPA at 120 K, we approximated the QE of a backside illuminated nBn device from the calculated vertical hole mobility for each strain and SL structure. To compare the results between the Ga-free and Ga-based SLs, the minority carrier lifetime for holes and the absorption will have a substantial effect on the QE in conjunction with the mobility. Based on the discussion on minority carrier lifetimes and absorption for T2SLs provided in Section 2.3.2.3 and Section 2.3.2.1, respectively. For Ga-based minority carrier lifetime for holes, there have been several examples of MWIR structures exhibiting minority carrier lifetime values on the order of 100 ns (Donetsky et al., 2010; Belenky et al., 2011; Olson et al., 2012). However, the Ga-free SLs in the MWIR regime have exhibited a range of values (i.e. 0.4 μ s to 9 μ s) Olson et al. (2012); Höglund et al. (2013, 2015); Aytac et al. (2015). For the sake of simple comparison, we chose a lifetime of 1 μ s which is an entire order of magnitude greater than the Ga-based structure. As for absorption, we used the first peak values values of 1,500 cm^{-1} and 1,000 cm^{-1} exhibited in the absorption spectrum of the 8.4/13.7 ML InAs/GaSb structure presented in Livneh et al. (2012, 2014) and the 12.8/12.8 ML InAs/InAs_{0.82}Sb_{0.18} structure presented in Klipstein et al. (2014) (see Chapter 2). The minority carrier diffusion length was estimated from the minority carrier lifetime and mobility using the Einstein relation (Eqs. (4.10) and (4.11)). Then, we used Eq. (4.12) to estimate the QE for nBn devices with absorber layer thicknesses that maximize the QE at zero strain.

For the QE estimate we used a more comprehensive mobility data set for low and high magnitudes of disorder. For each magnitude of disorder and material system, we calculated the vertical hole mobility at 120K for 10 differently disordered structures for strain configurations of -1.2% , -0.8% , -0.5% , -0.2% , 0.0% , $+0.2\%$, $+0.5\%$, and $+0.8\%$. Then, we computed the mean values for each strain configuration which are used to train the GP model. Taking the mean of the results over different realizations of the disorder better represents the transport behavior of a structure with a given magnitude of random disorder. The vertical hole mobility, minority hole diffusion length, and QE calculated over different realizations of low and high disorder are presented in Fig. 6.15 for the Ga-free and Ga-based structures, along with the values calculated for the ideal and no disorder SL.

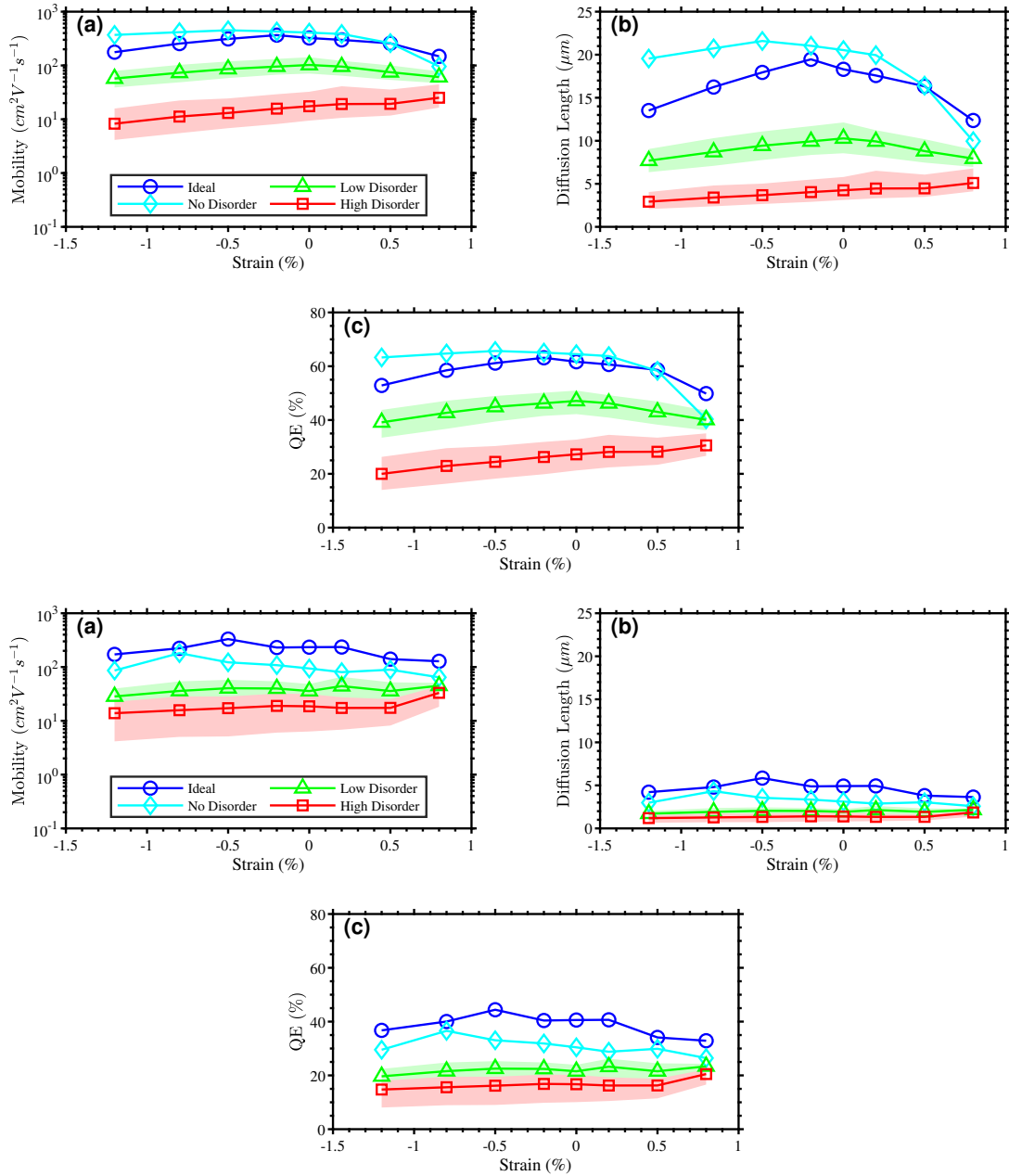


Figure 6.15: The (a) ((d)) vertical hole mobility, (b) ((e)) minority hole diffusion length, and (c) ((f)) subsequent QE calculated for a backside illuminated nBn device as a function of axisymmetric strain for the Ga-free ideal (blue line with circles), no disorder (cyan line with diamonds), low disorder (green line with triangles), and high disorder (red line with squares) SLs for the Ga-free (Ga-based) SL. The shaded areas indicate the minimum and maximum values obtained from the different disordered structures for each strain value. The ideal structures do not have disorder, so there is no shaded area. (a) ((d)), (b) ((e)), and (c) ((f)) adapted with permission from Glennon et al. (2024) (Glennon & Bellotti (2023)).

As expected, the disorder negatively impacted the vertical hole mobility throughout the range of axisymmetric strain. The range of values calculated for different realizations of the disorder, measured as a percentage of the average value, increases with increasing disorder. While the calculated hole mobility results for the Ga-free and Ga-based structures are not dramatically different for a given amount of disorder, the hole lifetimes differ dramatically, particularly for the ideal and no disorder structures. This is due to the order of magnitude difference in the minority carrier lifetimes between Ga-based and Ga-free structures. For the calculation of the QE, the absorber thicknesses for the ideal, no disorder, low disorder, and high disorder structures for the Ga-free SL were $15\ \mu\text{m}$, $16\ \mu\text{m}$, $10\ \mu\text{m}$, and $6\ \mu\text{m}$, respectively. In the case of the Ga-based SL, the absorber thicknesses were $5\ \mu\text{m}$, $4\ \mu\text{m}$, $3\ \mu\text{m}$, and $2\ \mu\text{m}$. The Ga-free SL exhibited higher QE's for each structure type compared with the Ga-based SL. In particular, QE values over 60% were demonstrated for the ideal and no disorder cases, representing a fundamental limit. In the case of Ga-based, the fundamental limit is suggested to be closer to 40%. However, this does not mean that the Ga-free SL is certain to be a better device, as it is possible that the Ga-based SLs may have less disorder. This could be the subject of future investigation.

These datasets were then used to train GP models, described in Glennon et al. (2023) and Glennon & Bellotti (2023), that predict the QE for arbitrary axisymmetric strains within the range of strains calculated using NEGF data. Finally, the GP predictions allowed us to map approximations of the QE for the two different device models as a function of the spatial coordinates of the die. Fig. 6.16a and Fig. 6.16b present the estimated QE for a curved-FPA with ideal, no disorder, low disorder, and high disorder structures for the Ga-free and Ga-based material systems, respectively.

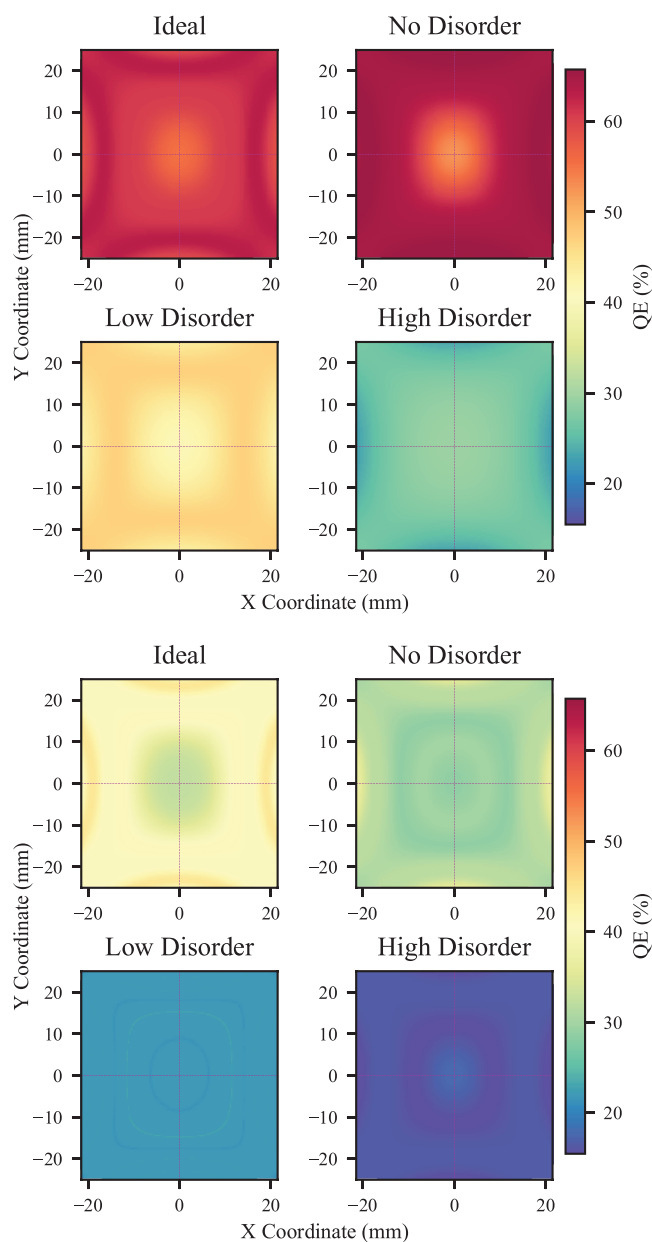


Figure 6.16: Approximate internal QE calculated as a function of spatial coordinates of the curved die at 120 K for the ideal, no disorder, low disorder, and high disorder SLs for a Ga-based nBn detector. (a) (b) adapted with permission from Glennon et al. (2024) (Glennon & Bellotti (2023)).

What is immediately apparent is that the impact on the QE from the strain is relatively small throughout the majority of the FPA in comparison to the impact of disorder for both

material systems. For all four SL types the majority of the FPA exhibits internal QE values within a range of approximately 1% nominal QE. However, throughout the high disorder device the internal QE values are between 23% to 42% (10.5% to 21%) nominal QE value lower than those demonstrated in the no disorder case for the Ga-free (Ga-based) SL. Thus, it can be expected that curving the FPA to an ROC of 70mm is unlikely to dramatically impact the QE with all other properties being equal. Alternatively, the performance can be improved significantly through optimizing the growth process to achieve SLs with reduced disorder. Additionally, as mentioned before, we found that the QE is better for each structure category in the Ga-free SL versus the Ga-based SL due to the order of magnitude higher minority carrier lifetime. However, it is worth pointing out that the high disorder results for the Ga-free SL are within the range between the no disorder and low disorder results of the Ga-based SL. Thus, it is possible that the Ga-based device could be superior given these results if it has substantially less disorder than the Ga-free structure.

Plots demonstrating the 2σ uncertainty associated with each device and material system in Fig. 6.16, providing the 95% confidence interval of our results, are presented in Fig. 6.17 and Fig. 6.18 for Ga-free and Ga-based structures, respectively.

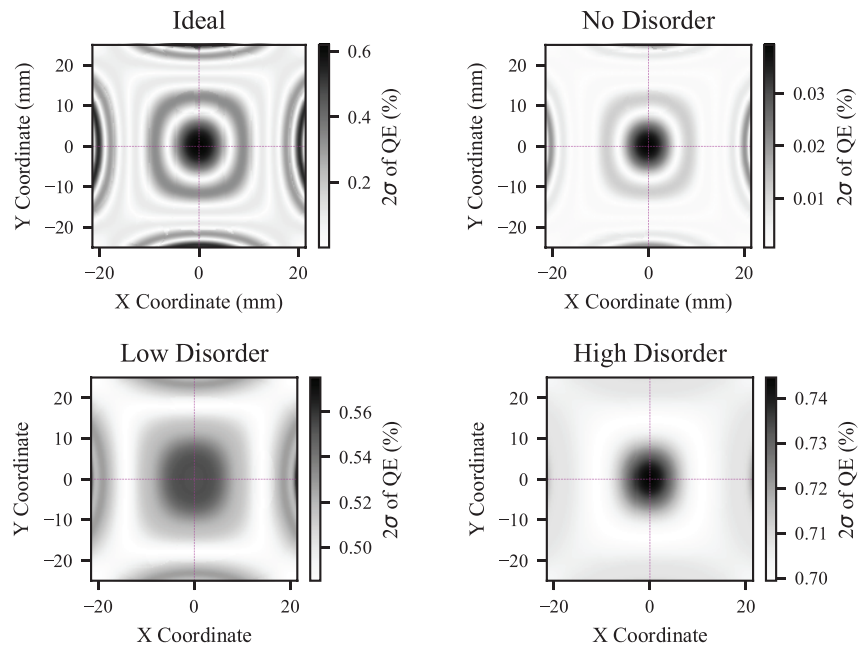


Figure 6.17: 2σ of approximated QE calculated as a function of spatial coordinates of the curved die at 120K for the ideal, no disorder, low disorder, and high disorder SLs. Reprinted with permission from Glennon et al. (2024).

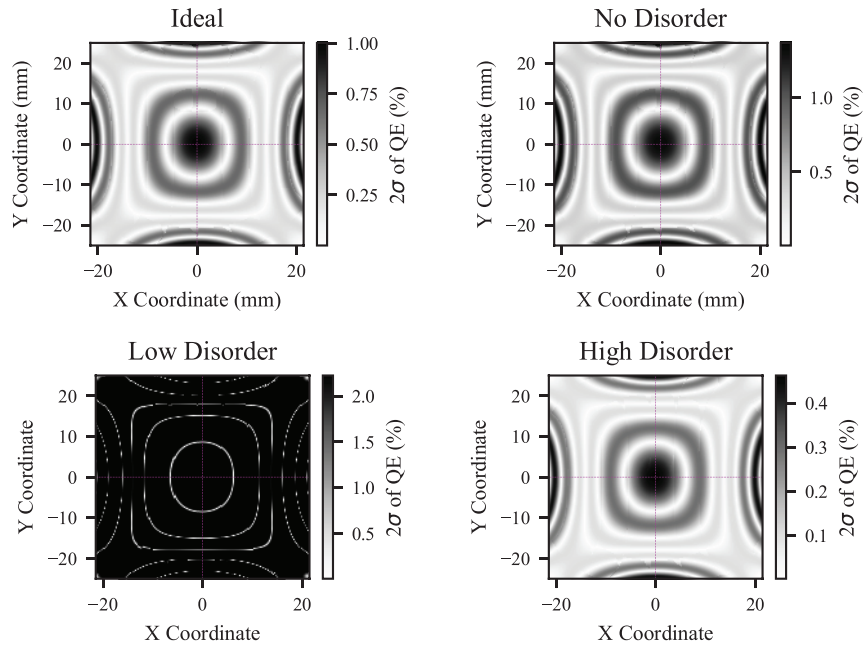


Figure 6.18: 2σ of approximated QE calculated as a function of spatial coordinates of the curved die at 120K for the ideal, no disorder, low disorder, and high disorder SLs. Reprinted with permission from Glennon & Bellotti (2023).

It was demonstrated that the uncertainty was larger for increasing amount of disorder, which one would expect. This may be a consequence of small sample size for the disordered structures.

The results of the two studies also suggested that it may be possible to further improve the performance of curved-FPAs with T2SL absorber layers by inducing a higher magnitude of positive axisymmetric strain. This is demonstrated in Fig. 6.19 which depicts the quantum efficiency as a function of temperature using Eq. (4.12) for axisymmetric strains of 0.0%, +0.8%, and +1.6% for the Ga-free SL. As with Fig. 6.15, we chose the diffusion lengths that maximize the QE for each dataset at 140 K.

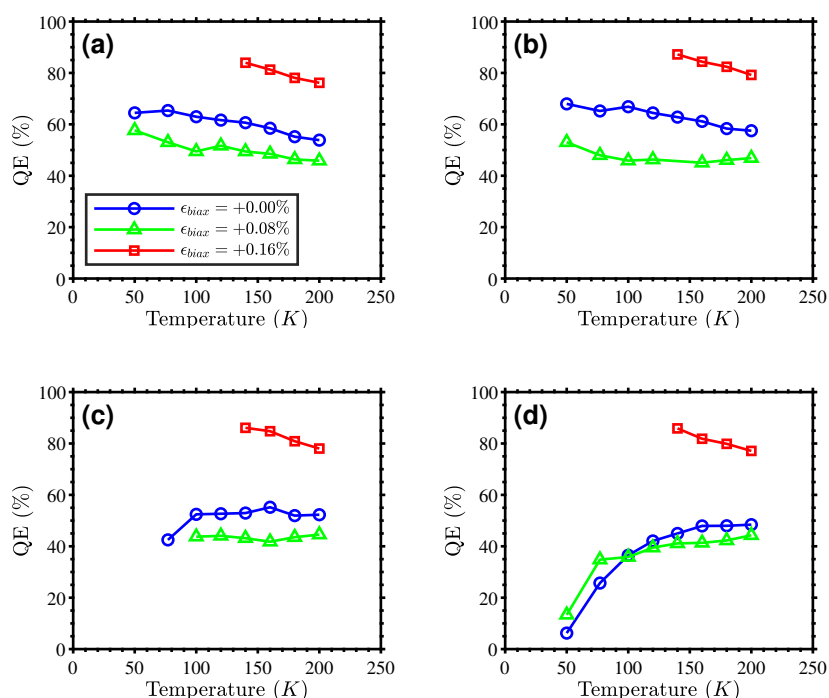


Figure 6.19: The internal QE estimated as a function of temperature for the Ga-free (a) ideal, (b) no disorder, (c) low disorder, and (d) high disorder SLs under +0.0% (blue line with circles), +0.8% (green line with triangles), and +1.6% (red line with squares) axisymmetric strain. Adapted with permission from Glennon et al. (2024).

I should note that the mobility data set is from Fig. 6.12 in which both the selected low and high disorder structures appear to result in high mobility relative to the mean values of Fig. 6.15. There is an improvement in the QE to approximately 90% for all SLs structures at 140 K and +1.6% axisymmetric strain. The increase in QE for the +1.6% case is a result of the considerable increase in vertical hole mobility. The die we are investigating, with an ROC of 70 mm, exhibits a maximum projected axisymmetric strain of just over +0.6%. Fig. 6.19 suggests that if greater tensile strain can be mechanically tolerated, then this effect may be used to overcome the degradation in QE due to SL disorder and improved device performance could be realized. It is important to note that the BG calculated for the Ga-free structure under an external strain of +1.6% is $7.2\mu\text{m}$. This suggests that an unstrained

T2SL with an initially larger BG should be selected first in order to achieve a MWIR band gap under the influence of positive strain. This is outside the scope of the present work, but is a potential avenue for future investigation.

6.6 CONCLUSION

In summary, we investigated the internal QE predicted for MWIR Ga-free and Ga-based T2SL-based cFPAs via the hole mobility extraction methodology validated in Chapter 5. In doing so we demonstrated a framework for studying the transport properties of externally strained T2SLs based on a combination of FEA modeling, NEGF calculations, and machine learning. The effects of atomic migration and SL disorder were demonstrated in the case of two example structures of the Ga-free and Ga-based T2SL material systems in which it was demonstrated that an inversion of the temperature dependence occurred for higher disorder. The Ga-free SL exhibited higher QE for the ideal, no disorder, low disorder, and high disorder structures due to the much longer minority carrier lifetime. This suggests that Ga-free SLs have an advantage over Ga-based SLs for the same degree of disorder. Future investigation could focus on a comparison of the disorder for experimentally grown SLs to make a more definitive determination. Additionally, it was demonstrated that disorder has a much larger effect on the estimated QE compared to the strain present in a curved die with an ROC of 70 mm indicating that the curving procedure may have only a marginal effect on the QE. As a secondary observation, it was shown that it may be possible to enhance the QE of a T2SL based cFPA sensor by implementing large positive axisymmetric strain. However, it is important to note that this will cause a decrease in the BG. Ultimately, this procedure can be used more generally to investigate the transport properties of externally strained materials and predict the impact on device performance.

CHAPTER 7

Type-II Superlattice Optimization for Enhanced Hole Transport in the LWIR Regime

The bulk of the work presented in this chapter has been submitted to JAP for publication (?). The details have been reproduced and repurposed to serve the overall narrative of this dissertation.

7.1 INTRODUCTION

While relatively long minority carrier lifetimes have been demonstrated in Ga-free type-II superlattices (T2SLs) (Steenbergen et al., 2011; Höglund et al., 2013), the mobility of holes, an important parameter affecting carrier collection, is relatively poor in these structures, particularly in the LWIR regime (Olson et al., 2017). While electron mobility tends to be several orders of magnitude higher than holes in T2SLs (Swartz & Myers, 2014; Taghipour et al., 2017; Casias et al., 2020), electron-based devices suffer from high surface leakage induced dark current (Sidor, 2017; Marozas et al., 2018; Ting et al., 2022b). Thus, a demonstration of a long-wave (LWIR) Ga-free SL structure with enhanced hole mobility would present a candidate infrared material that exhibits many of the advantages of T2SLs without the issue of poor carrier collection.

The electronic properties of T2SLs are not only dependent on the chemical composition of the individual layers, but also the specific structural geometry of the superlattice (SL). For Ga-free SLs, the layer thicknesses of the two different SL layers, the antimony (Sb) composition of each layer, and the substrate lattice constant all represent parameters effecting the electronic properties. Arbitrary substrate lattice constants between those of InAs and InSb can be achieved using virtual substrates (Belenky et al., 2020). There are several practical limitations on which structures can be realistically grown with high qual-

ity, such as the critical thickness of the individual layers (Lackner, 2011) and limitations on the resolution of current SL growth methods. However, arbitrary Sb compositions and lattice constants result in an effectively infinite parameter space.

The experimental realization of potential SL structures requires significant time and resources. Conversely, the simulation of structures through $k \cdot p$ band structure calculations and carrier transport simulations can be used to predict optimized structures at a far lower cost. Additionally, Gaussian processes (GPs), a machine-learning algorithm for performing non-parameteric Bayesian regression on a dataset while providing a reliable estimate of the uncertainty, can be used to reduce the number of simulations required to make predictions about optimized structures. This chapter presents the results of a investigation probing the parameter space of Ga-free T2SLs grown on either GaSb or a hypothetical 6.2 Å substrate to find structures optimized for enhanced hole transport properties within the LWIR regime. Carrier transport was studied for several exemplary structures for both ideal and disordered SLs.

7.2 SL STRUCTURE OPTIMIZATION

To describe the complex band structure of Ga-free SLs we chose the four-band $k \cdot p$ Hamiltonian within the axial approximation (Eq. 3.18). We chose the parameters listed in Ref. Qiao et al. (2012) to describe the band properties of bulk InAs and InSb. The low temperature (12 K) bandgap bowing parameter in the case of unstrained SLs was taken from Ref. (Webster et al., 2015). Strain was incorporated in the Hamiltonian as demonstrated in Eq. 3.19.

To make predictions about optimized structures, we calculated the band gap and hole conductivity effective mass of a comprehensive set of different SL structures for a given substrate. The conductivity effective mass was calculated at a temperature of 150 K, as

described in Ting et al. (2016). Then, we used the PYTHON SCIKIT-LEARN package (Pedregosa et al., 2011) to implement Gaussian processes (GP) including radial basis function and white noise kernels. The parameters used as input for the GP model consisted of each layer thickness, t_1 and t_2 , and the Sb composition of each layer, Sb_1 and Sb_2 . Different sets of GP models were used for each substrate lattice constant c . Two different GP models were fitted in which the input variables were paired with the calculated band gap and conductivity effective mass. The two GP models were then trained according to the two different datasets, respectively. Finally, we used this model, probing the parameter space for structures with band gaps in the LWIR regime and selected structures with the lowest conductivity effective masses. Finally, we calculated the band structures of these selections to confirm that the GP predicted band gap and conductivity effective mass for each structure were accurate. From this set of results, we chose a few exemplary structures to analyze.

We chose to investigate the parameter space of Ga-free SLs latticed matched to either GaSb or a virtual substrate with a 6.2 \AA lattice constant in the case of ideal interfaces. We selected two different substrate lattice constants to exemplify using the lattice constant as another parameter that can be tuned to optimize SL properties. Additionally, there have been examples of InAs/InAsSb SLs grown on 6.2 \AA virtual substrates in the literature (Liu et al., 2022). For the GP training dataset we chose the set of SL structures with odd numbered values of layer thicknesses, t_1 and t_2 , between 5 and 21 monolayer (ML), inclusive. For each unique combination of t_1 and t_2 , we ran band structure calculations for structures with all combinations of Sb layer compositions, Sb_1 and Sb_2 , in the list 0.0, 0.1, , 1.0 restricted to the condition that Sb_1 always be lower than Sb_2 , to avoid duplicated structures. In all, we calculated the band gap and conductivity effective mass for 4,455 unique structures for each lattice constant. Then, we trained two GP models, one for each output, accord-

ing to each data set. Using the GP models, we predicted the band gap and conductivity effective mass for structures with any combination of layer thicknesses between 5 – 21 ML and any combination of integer percentage value Sb compositions, selecting for structures with BGs near 0.1 meV. We restricted our selection to those matching two criteria to limit our search to SL structures that may be possible to grow. The first condition was that each layer thickness be below the Matthews-Blakeslee critical thickness (Matthews & Blakeslee, 1974), as described in Lackner (2011). The second condition was that the net strain in the entire SL period be no greater than $\pm 0.4\%$. This limit for the net strain was chosen as it aligns with the highest values exhibited by the experimental T2SL structures described in Rehm et al. (2013).

After executing the GP model on all possible SL structures with integer layer thicknesses and Sb composition we executed confirmation band structure calculations of the structures that exhibited a band gap close to 100 meV and fulfilled the two strain related requirements. Ultimately, we chose the structures 14/5 ML InAs/InAs_{0.43}Sb_{0.57} and 21/12 ML InAs/InAs_{0.61}Sb_{0.39} on a GaSb substrate, which correspond with the lowest and highest conductivity hole effective masses (0.73 versus 1.28), as well as 16/7 ML InAs_{0.66}Sb_{0.34}/InAs_{0.48}Sb_{0.52} on a 6.2 Å substrate which had the lowest conductivity hole effective mass (0.52). Throughout this work, each of these SL structures will be referred to as structure one, structure two, and structure three, respectively. The calculated band structures are presented in Fig. 7.1a, Fig. 7.1b, and Fig. 7.1c for structures one, two, and three, respectively. Structure one and three exhibit more dispersion in the growth direction which is indicative of higher transport properties. Also, structure three has more valence states that are close to the band edge that could be relevant for transport.

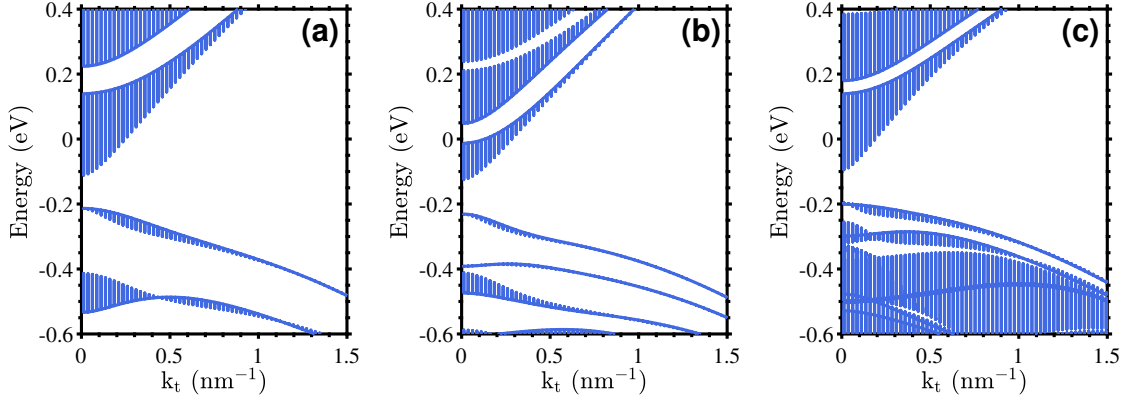


Figure 7.1: The band structures calculated for the (a) 14/5 ML InAs/InAs_{0.43}Sb_{0.57} structure and the (b) 21/12 ML InAs/InAs_{0.61}Sb_{0.39} structure on a GaSb substrate and the (c) 16/7 ML InAs_{0.66}Sb_{0.34}/InAs_{0.48}Sb_{0.52} structure on a 6.2 Å substrate. The vertical lines represent the dispersion with respect to the vertical wave vector.

7.3 MOBILITY FOR OPTIMIZED STRUCTURES WITH IDEAL INTERFACES

For all three structures with ideal interfaces we performed several NEGF simulations with sizes between 100 nm and 250 nm, selecting those for which linear resistance behavior was achieved, and fit the slope to Eq. 3.98 to calculate the vertical hole mobility. When coherent transport is significant, the nature of the contact material has a larger effect on carrier transport. We tailored the contacts so that the valence band edges were approximately 30 meV above the valence miniband edge for consistency. For structures one, two, and three, the contact materials are InAs_{0.62}Sb_{0.38}, InAs_{0.64}Sb_{0.36}, and InAs_{0.56}Sb_{0.44}, respectively. Band diagrams of the 50nm simulations for structures one, two and three are presented in Fig. 7.2a, Fig. 7.2b, and Fig. 7.2c, respectively. What is immediately apparent when comparing the two structures grown on GaSb is that structure one, with the lower effective mass, has narrower hole barrier layers (InAs) than structure two. Furthermore, structure three, with the lowest hole effective mass, has only slightly thicker, but lower energy, barriers than structure one. Fig. 7.3 presents the vertical hole mobility as a function

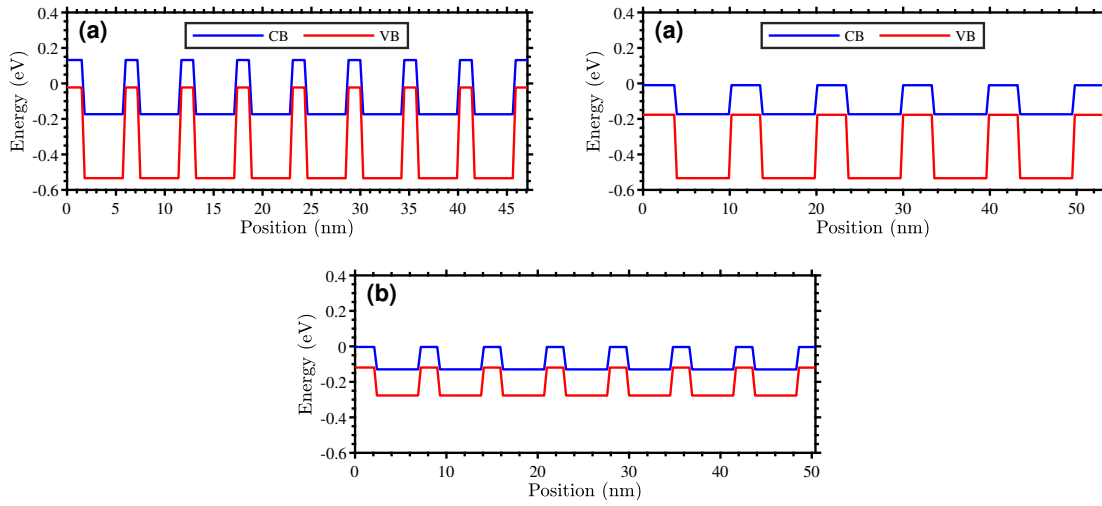


Figure 7.2: Examples of the band diagrams for the (a) InAs/InAs_{0.43}Sb_{0.57} and the (b) InAs/InAs_{0.61}Sb_{0.39} on a GaSb substrate and (c) InAs_{0.66}Sb_{0.34}/InAs_{0.48}Sb_{0.52} on a 6.2 Å substrate structures.

of temperature for all three selected SL structures with ideal interfaces. The relative magnitude of each mobility calculated for all structures correspond inversely with the relative magnitude of the conductivity effective mass. However, near 150 K the mobility for structure one is nearly the same as that of structure two, which is unexpected. There is some qualitative evidence of a difference in temperature dependence of the mobility when comparing the conductivity hole effective masses at 100 K, 150 K, and 200 K for structures one (0.83, 0.73, and 0.76) and two (1.21, 1.28, and 1.59). We see that the conductivity effective mass increases at 100 K with respect to that at 150 K for structure one while it decreases for structure two. However, this is not enough to explain the nearly identical mobility value at 150 K. One possible explanation is that while linear resistance seems to have been achieved for structure one at each calculated mobility it is possible that the nature of the contacts is still impacting the results. Furthermore, the conductivity effective mass, which assumes a constant relaxation time, is unable to capture the full physics of carrier transport with scattering in complex nanostructures like SLs. However, qualitatively the relative magnitudes

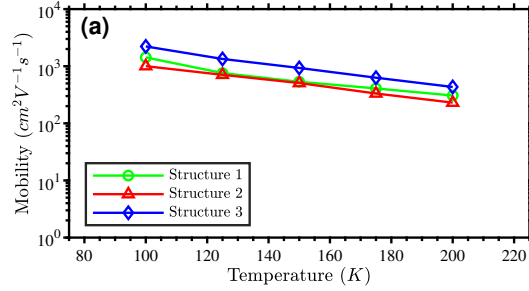


Figure 7.3: The vertical hole mobility calculated as a function of temperature for the 34/6 ML $\text{InAs}_{0.97}\text{Sb}_{0.03}$ / $\text{InAs}_{0.52}\text{Sb}_{0.48}$ structure (green line with circles) and $\text{InAs}/\text{InAs}_{0.61}\text{Sb}_{0.39}$ structure (red line with triangles) both on a GaSb lattice and the 5/3 ML $\text{InAs}_{0.66}\text{Sb}_{0.34}/\text{InAs}_{0.48}\text{Sb}_{0.52}$ structure (blue line with diamonds) on a 6.2 Å substrate for ideal interfaces.

of the mobility match those of the conductivity effective mass for each structure. Thus, the much more computationally efficient conductivity effective mass calculation may be used to aid in the optimization of SL structures for carrier transport before resorting to the far more computationally demanding NEGF formalism. However, the method requires care as it is more qualitative in nature and can not be used with certainty to rank structures in terms of carrier mobility.

7.4 EFFECTS DISORDERED INTERFACES ON OPTIMIZED STRUCTURES

In the case of disorder, we randomly selected interfaces in which to shift one ML in the growth direction. This is referred to as positional disorder, as described in Bellotti et al. (2021). An example of an ideal SL structure compared with a disordered one is presented in Fig. 7.4, where the effect of disorder on the band diagram is clearly represented. Positional disorder presents a more realistic depiction of experimentally grown structures that inherently include disorder. To this end, we generated four, six, and ten randomly disordered samples per structure with a thickness of approximately 50 nm for structures one, two, and three, respectively. In order to calculate the mobility using Eq. 3.98, we generated mod-

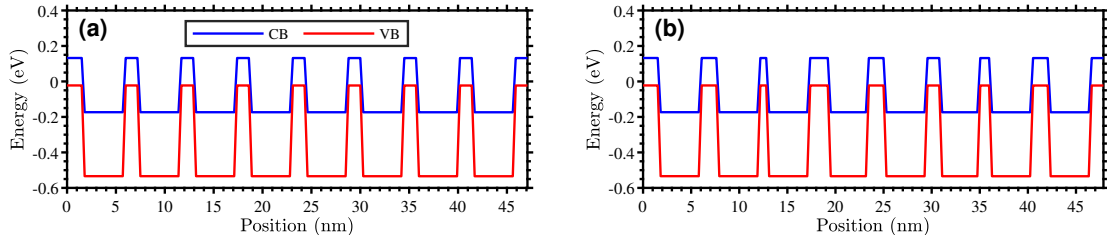


Figure 7.4: Example band diagrams of an InAs/InAs_{0.43}Sb_{0.57} SL structure with (a) ideal and (b) disordered interfaces, on a GaSb substrate.

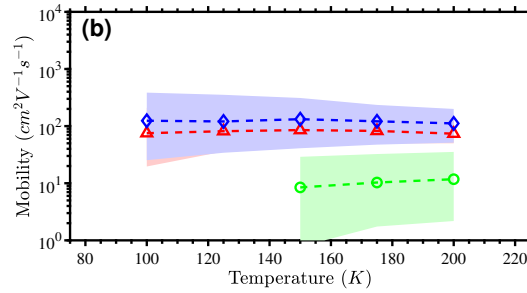


Figure 7.5: The vertical hole mobility calculated as a function of temperature for the 34/6 ML InAs_{0.97}Sb_{0.03}/InAs_{0.52}Sb_{0.48} structure (green line with circles) and InAs/InAs_{0.61}Sb_{0.39} structure (red line with triangles) both on a GaSb lattice and the 5/3 ML InAs_{0.66}Sb_{0.34}/InAs_{0.48}Sb_{0.52} structure (blue line with diamonds) on a 6.2 Å substrate for positional disordered interfaces. The range of mobility for each structure is included as a shaded area around the mean data.

els in which we have one, two, and three of each of these disordered units repeated end-to-end. Given that each differently disordered structure produces different results, we calculated the mobility of each one individually and calculate the mean of the results. The mean mobility as a function of temperature is included in Fig. 7.5. What is most striking is that structure one has the lowest mean mobility by close to an order of magnitude. Structure three still exhibits the highest mobility out of the three structures. This can be explained by the relative density of interfaces in the material. Structure one has the thinnest SL layers, and thus the highest density of interfaces. Having the same probability of disorder at each interface, structure one has the highest density of disorder. Furthermore, 1 ML of

disorder on either side of hole wells that are 5 ML thick (structure one) will cause greater shifts in the local density of states (LDOS) than in 12 ML hole wells (structure two). This shifting of the LDOS can cause a misalignment of LDOS between hole wells, which can impede the transport of carriers across a SL Bellotti et al. (2021). Structure three has the most resilience to the disorder. While having thin hole wells (7 ML) like structure one, the energy barrier of these wells is much lower due to the Sb composition of the two layers on the 6.2 Å substrate. Furthermore, structure three had the lowest conductivity effective mass of all three structures, suggesting inherently stronger coupling between wells. The conductivity effective mass of the ideal structures alone are unlikely to reliably predict the relative carrier transport efficiency in disordered SLs in general.

To find a better method for predicting the relative carrier transport efficiency for different SL structures without resorting to NEGF we generated 25 different randomly disordered 50 nm lattices per structure. However, we calculate the band structure of the non-interacting Hamiltonian with periodic boundary conditions, thus generating a quasi-random periodic structure. From the band structure, we calculate the conductivity effective mass for holes at 150 K, as before. Taking the mean of these effective masses, we find 21, 200, 127, and 8 for structures one, two, and three, respectively. The relative values were qualitatively commensurate with the calculated mean vertical hole mobility for each structure. Therefore, we had demonstrated that the conductivity effective mass calculated for quasi-random periodic structures can be used to predict relative carrier mobility for the selected disordered structures. The hole effective masses calculated for the disordered structures differ by several orders of magnitude while those of ideal structures were far closer. It is likely that the greater the difference in effective mass the more accurately one can predict the relative hole mobility. A final note of import is that in calculating the mean band gap for the disordered structures, we found that they corresponded with cutoffs of 23.4 μm , 12.4 μm , and 13.6 μm ,

respectively. Unsurprisingly, the cutoff for structure one was the most impacted by the disorder in the lattice. This shift in the cutoff due to disorder must be taken into consideration when attempting to find optimal SLs for sensors in a specific spectral band.

7.5 CONCLUSION

In summary, we used GP regression to optimize Ga-free SL structures for hole transport grown on GaSb and 6.2 Å substrates based on band structure analysis. Restricting the search to structures that fulfil several strain requirements for experimental feasibility, we selected three structures: the structures with the highest and lowest effective masses on GaSb and the structure with the lowest effective mass on a 6.2 Å substrate. NEGF is used to calculate the vertical hole mobility for each structure confirming an inverse relationship between the calculated hole effective mass and the mobility at most temperatures, while the results at 100 K were less straightforward. This is likely due to the complexities of carrier transport in SLs which cannot be perfectly captured by an effective mass. Next, we calculate the mean vertical hole mobility as a function of temperature for each structure using NEGF simulations of five differently disordered samples per selected structure. It is discovered that structure one has a significantly lower hole mobility than the other two, and structure three is the most resilient to disorder. We find that this can be predicted qualitatively from the conductivity hole effective masses calculated via the band structures of quasi-randomly disordered periodic samples. In this case, the effective masses differed by several orders of magnitude between structures, making predictions about the hole mobility more reliable. Thus, a methodology for finding realistic SL structures optimized for carrier transport is presented.

CHAPTER 8

Conclusion

As discussed in Chapter 2, type-II superlattices (T2SLs) are a potential alternative to the state-of-the-art HgCdTe infrared (IR) material system, due to several theoretical advantages. Chief among these advantages are significantly reduced cost due to the larger industrial base for III-V materials (Bajaj et al., 2007) as well as higher yield (Rogalski, 2003). However, the promise of superior performance due to suppressed Auger scattering has not yet been realized (Rogalski et al., 2019). This is typically attributed to inferior properties associated with the quantum efficiency (QE), like the absorption coefficient, the lifetime, and the mobility (see Chapter 2). Therefore, the field would greatly benefit from the development of methodologies to investigate these properties further. Using this method, one could not only predict the performance of standard T2SL structures used in advanced device architectures, but also discover new potential T2SL structures with enhanced properties.

Chapter 5 presented a comprehensive investigation into several vertical mobility extraction methodologies from non-equilibrium Green's functions (NEGF). It was demonstrated that for structures on the order of several hundreds of nanometers the ballistic resistance can be relevant for both electrons and holes. Therefore, using the average velocity of carriers calculated in the channel resulting in an apparent mobility that increased with increasing device size. This demonstrates the weakness of this method for predicting the mobility in a larger sample of T2SL material. Additionally, while in principle running NEGF simulations with and without scattering and comparing the results with a Matthiessen's relationship should account for the ballistic resistance, it was demonstrated that this method can be unreliable. Finally, it was shown that using the dependence of the resistance with device size can account for the ballistic resistance and result in the extraction of a diffusive mobility. Electrons were shown to present significant problems due to the highly coherent

nature of the carrier transport present in these calculations and higher electric fields may be required to compensate. Holes on the other hand were shown to result in a device size independent diffusive mobility. This method was used in subsequent chapters to simulate the properties of several T2SL structures.

The results of two studies (one with a Ga-free SL absorber and the other with a Ga-based SL absorber) simulating the QE across a mid-wave (MWIR) nBn-based curved focal-plane array (cFPA) were presented in Chapter 6. The chosen T2SL structures were of standard design grown on a GaSb substrate. The effects of both superlattice (SL) disorder and the external strain, which is induced in the material due to the mechanical curving procedure, on the vertical hole mobility were studied. The inversion of temperature dependence that has been exhibited in the experimental hole mobility for T2SLs (see Chapter 2) was shown to emerge with increasing SL disorder. Additionally, strain had a relatively minor impact on the hole mobility except for large strain magnitudes. In predicting the QE across the surface of the cFPA it was shown that the reduction in the QE due to the strain was negligible in comparison with the reduction in QE due to disorder. Thus, the cFPA design is likely to exhibit similar properties to a flat FPA of a similar material. However, it would benefit from the optical advantages of cFPAs. Lastly, it was revealed that a high magnitude of positive strain results in a sharp increase in the vertical hole mobility which is likely related to an inversion of the light-hole (LH) and heavy-hole (HH) minibands. This result presents a potential strategy for developing devices with enhanced hole mobility by inducing high magnitudes of positive strain in the absorber layer.

Finally, Chapter 7 presented a methodology that was developed for searching for optimized structures for carrier transport in T2SLs. Specifically, this study focused on optimizing long-wave (LWIR) Ga-free SLs grown on GaSb and 6.2 Å substrates. Band structure calculations were performed for collections of 4,455 different SL structures spanning the

parameter space of layer composition and thickness for each substrate. A Gaussian process (GP) regression model was trained to this data set and used to search for structures with the lowest hole conductivity effective masses with cutoff wavelengths of about $12\mu\text{m}$. One structure with the highest (GaSb substrate) and two structures with the lowest (GaSb and 6.2 \AA substrates) hole conductivity effective mass were selected. It was demonstrated that the conductivity effective mass was qualitatively indicative of the relative magnitude of the disorder. The 6.2 \AA substrate structure has the highest mobility. Additionally, these structures were simulated with positional disorder, demonstrating that the structure with the lowest effective mass on GaSb had the lowest mobility. Thus, simple band structure calculations of an ideal SL is not enough to predict realistic carrier transport efficiency. However, band structure calculations of quasi-randomly disordered multi-period samples of each structure were shown to produce effective mass values that could qualitatively predict the relative magnitude of the disordered mobility for each structure. Thus, it was shown to be possible to use band structure analysis on periodic multi-period disordered structures to predict the carrier transport efficiency in more realistic growth conditions. The 6.2 \AA substrate structure had the best results in both ideal and disordered cases, presenting a candidate structure for enhanced hole transport.

Hence, this work has contributed significantly to the field of T2SL simulation. It includes, to the author's knowledge, the first comprehensive analysis of the extraction of mobility from quantum transport simulations for application to IR photodetectors (PDs). Then, this method was demonstrated for use in predicting the hole mobility for MWIR Ga-free and Ga-based SLs with disorder demonstrating favorable comparison to experimental results. Finally, a methodology for optimizing T2SL structures for enhanced carrier transport was demonstrated that could be used to prototype T2SL structures with better performance in future studies.

APPENDIX A

Ballistic Mobility and Resistance

The work presented in this appendix has been published in Glennon et al. (2023). The details have been reproduced to serve the overall narrative of this dissertation.

A.1 3D BULK BALLISTIC MOBILITY

We solved for the ballistic mobility of a 3D bulk device (Eq. (5.2)) by following the methods of Lundstrom and colleagues for the calculation of the conductance and ballistic mobility for 2D bulk devices Lundstrom & Jeong (2013); Lundstrom & Sun (2016). We started with the expression for the conductance in the Landauer formalism Lundstrom & Jeong (2013):

$$G = \frac{2q^2}{h} \int \mathcal{T}(E)M(E) \left(-\frac{\partial f_0}{\partial E} \right) dE, \quad (\text{A.1})$$

where the partial derivative of the Fermi function, f_0 , comes from the Taylor expansion of the difference of the Fermi levels between contacts, \mathcal{T} is the transmission function at energy, E , M is the number of conducting channels between contacts, q is the elementary charge, and h is Plank's constant. Next, using the standard expression for the 3D conductance Lundstrom & Jeong (2013) $\sigma_{\text{app}} = \frac{L}{A}G$ in combination with Eq. (A.1) we found:

$$\sigma_{\text{app}} = \frac{2q^2}{h} \int (\mathcal{T}(E)L) \left(\frac{M(E)}{A} \right) \left(-\frac{\partial f_0}{\partial E} \right) dE, \quad (\text{A.2})$$

As pointed out by Lundstrom and Sun, this conductivity should be thought of as an ‘‘apparent conductivity’’ in the case of ballistic transport, as the definition of conductivity is generally applied in the diffusive limit (Lundstrom & Sun, 2016). Similarly, the apparent mobility, μ , was extracted based on the relationship between mobility and conductivity in

the diffusive limit: $\sigma_{app} = nq\mu_{app}$ where n is the carrier density in the device. Combining this expression with Eq. (A.2) we derived an expression for the apparent mobility for a 3D bulk device:

$$\mu_{app} = \frac{2q/h}{n} \int (\mathcal{T}(E)L) \left(\frac{M(E)}{A} \right) \left(-\frac{\partial f_0}{\partial E} \right) dE, \quad (\text{A.3})$$

Using the expression for the number of conducting modes in a 3D device given in Lundstrom & Jeong (2013) and the fact that the transmission function is equal to unity for ballistic transport, Eq. (A.3) was rewritten to represent the ballistic mobility as follows:

$$\mu_{ball} = \frac{2q/h}{n} L \left(\frac{m^*}{2\pi\hbar^2} \right) (K_B T) \frac{\partial}{\partial \eta_F} \int \frac{d\varepsilon}{e^{(\varepsilon - \eta_F)} + 1} d\varepsilon, \quad (\text{A.4})$$

where m^* is the effective mass, K_B is the Boltzmann constant, T is the temperature, \hbar the reduced Plank's constant, and with substituted variables $\varepsilon = \frac{E - E_c}{K_B T}$ and $\eta_F = \frac{E_F - E_c}{K_B T}$ where E_c and E_F are the conduction band and Fermi energies, respectively. Using the rules for Fermi integrals as given by Lundstrom & Jeong (2013), we can simplified Eq. (A.4) to the following:

$$\mu_{ball} = \frac{2q/h}{n} L \left(\frac{m^*}{2\pi\hbar^2} \right) (K_B T) \mathcal{F}_0(\eta), \quad (\text{A.5})$$

where \mathcal{F}_0 is the Fermi-Direct integral of order zero. To derive the final expression for the apparent mobility, we first derived an expression for the carrier density. We started with the equation for carrier density in 3D bulk materials (Lundstrom & Jeong, 2013):

$$n = \int D_{3D} f_0(E_F) dE, \quad (\text{A.6})$$

where D_{3D} is the 3D density of states. Inserting the expression for the 3D density of states

given in Lundstrom & Jeong (2013) we found:

$$n = \frac{\sqrt{2(m^*K_B T)^3}}{\pi^2 \hbar^3} \int \frac{d\varepsilon^{1/2}}{e^{(\varepsilon - \eta_F)} + 1} d\varepsilon. \quad (\text{A.7})$$

Using the definition for the Fermi integral of one-half order, $F_{1/2}$, we arrived at our final expression for carrier density:

$$n = \frac{\sqrt{2(m^*K_B T)^3}}{\pi^2 \hbar^3} \frac{\sqrt{\pi}}{2} \mathcal{F}_{1/2}(\eta_F). \quad (\text{A.8})$$

We inserted Eq. (A.8) into Eq. (A.5) to derive our final expression for ballistic mobility:

$$\mu_{ball} = \frac{Lv_T}{2(K_B T/q)} \frac{\mathcal{F}_0(\eta_F)}{\mathcal{F}_{1/2}(\eta_F)}, \quad (\text{A.9})$$

We inserted the unidirectional thermal velocity, $v_T = \sqrt{\frac{2k_B T}{\pi m^*}}$, into Eq. (A.9).

A.2 3D BULK BALLISTIC RESISTANCE

We solved for the ballistic resistance of a 3D bulk material in a similar manner as Eq. (A.9) in Abstract A by starting with the reciprocal of the expression for conductivity in the Landauer formalism (A.1):

$$R = 1/G = \frac{h}{2q^2} \left(\int \mathcal{T}(E) M(E) \left(-\frac{\partial f_0}{\partial E} \right) dE \right)^{-1}. \quad (\text{A.10})$$

Using the definition of the Fermi integral, the expression for the number of conducting channels in a 3D device (Lundstrom & Jeong, 2013), and the fact that the transmission

function is equal to unity for ballistic transport, Eq. (A.10) was transformed as follows:

$$R_{ball} = 1/G = \frac{h}{2q^2} \frac{2\pi\hbar^2}{m^*K_B T} \left(\frac{\partial}{\partial \eta_F} \int \frac{\epsilon}{e^{\epsilon - \eta_F}} d\epsilon \right)^{-1}. \quad (\text{A.11})$$

We used the rules for Fermi integrals provided in Lundstrom & Jeong (2013) to simplify the expression:

$$R_{ball} = \frac{h}{2q^2} \frac{2\pi\hbar^2}{m^*K_B T} \frac{1}{\mathcal{F}_0(\eta_F)}. \quad (\text{A.12})$$

Finally, we substituted in the expression for the carrier density (Eq. (A.8)) to derive the final form of the expression for ballistic resistance as given in Section 5.2:

$$R_{ball} = \frac{\sqrt{2\pi m^* K_B T}}{nq^2} \frac{\mathcal{F}_{1/2}(\eta_F)}{\mathcal{F}_0(\eta_F)}. \quad (\text{A.13})$$

BIBLIOGRAPHY

- Aalok, A. (2021). Professional plots. https://www.mathworks.com/matlabcentral/fileexchange/100766-professional_plots. [Online; accessed October 31, 2022].
- Aeberhard, U. (2008). *A Microscopic Theory of Quantum Well Photovoltaics*. Ph.D. thesis, Eidgenössische Technische Hochschule Zürich.
- Aifer, E. H., Tischler, J. G., Warner, J. H., Vurgaftman, I., Bewley, W. W., Meyer, J. R., Kim, J. C., Whitman, L. J., Canedy, C. L., & Jackson, E. M. (2006). W-structured type-ii superlattice long-wave infrared photodiodes with high quantum efficiency. *Applied Physics Letters*, 89(5), 053519.
- Aifer, E. H., Tischler, J. G., Warner, J. H., Vurgaftman, I., Kim, J. C., Meyer, J. R., Bennett, B. R., Whitman, L. J., Jackson, E. M., & Lorentzen, J. R. (2005). W-structured type-II superlattice-based long- and very long wavelength infrared photodiodes. In M. Razeghi, & G. J. Brown (Eds.) *Quantum Sensing and Nanophotonic Devices II*, vol. 5732, (pp. 259 – 272). International Society for Optics and Photonics, SPIE. <https://doi.org/10.1117/12.597134>.
- Aifer, E. H., Warner, J. H., Canedy, C. L., Vurgaftman, I., Jackson, E. M., Tischler, J. G., Meyer, J. R., Powell, S. P., Olver, K., & Tennant, W. E. (2010). Shallow-etch mesa isolation of graded-bandgap “w”-structured type-ii superlattice photodiodes. *Journal of Electronic Materials*, 39(7), 1070–1079.
- Akel, K., Hostut, M., Tansel, T., & Ergun, Y. (2018). Large hh-lh splitting energy for inas/alsb/gasb based n-structure photodetectors. *Journal of Applied Physics*, 123(2), 025703.
- Aldegunde, M., Martinez, A., & Asenov, A. (2011). Non-equilibrium greens function analysis of cross section and channel length dependence of phonon scattering and its impact on the performance of si nanowire field effect transistors. *Journal of Applied Physics*, 110(9), 094518.
- Alshahrani, D. O., Kesaria, M., Anyebe, E. A., Srivastava, V., & Huffaker, D. L. (2022). Emerging type-ii superlattices of inas/inassb and inas/gasb for mid-wavelength infrared photodetectors. *Advanced Photonics Research*, 3(2), 2100094.
- Ancona, M. G., & Svizhenko, A. (2008). Density-gradient theory of tunneling: Physics and verification in one dimension. *Journal of Applied Physics*, 104(7), 073726.
- Arnold, D. N., David, G., Jerison, D., Mayboroda, S., & Filoche, M. (2016). Effective confining potential of quantum states in disordered media. *Physical Review Letters*, 116, 056602.

- Arora, V. K. (2012). Ballistic transport in nanoscale devices. In *Proceedings of the 19th International Conference Mixed Design of Integrated Circuits and Systems - MIXDES 2012*, (pp. 17–24).
- Arounassalame, V., Bouschet, M., Alchaar, R., Ferreira, R., Carosella, F., Ramiandrasoa, A., Perez, J., Péré-Laperne, N., Christol, P., & Ribet-Mohamed, I. (2022). Anisotropic transport investigation through different etching depths in InAs/InAsSb T2SL barrier mid-wave infrared detector. *Infrared Physics & Technology*, *126*, 104315.
- Aytac, Y., Olson, B. V., Kim, J. K., Shaner, E. A., Hawkins, S. D., Klem, J. F., Flatté, M. E., & Boggess, T. F. (2015). Temperature dependent carrier lifetime measurements of InAs/InAsSb T2SLs. In M. Razeghi, E. Tournié, & G. J. Brown (Eds.) *Quantum Sensing and Nanophotonic Devices XII*, vol. 9370, (p. 93700J). International Society for Optics and Photonics, SPIE. <https://doi.org/10.1117/12.2077753>.
- Bajaj, J., Sullivan, G., Lee, D., Aifer, E., & Razeghi, M. (2007). Comparison of type-II superlattice and HgCdTe infrared detector technologies. In B. F. Andresen, G. F. Fulop, & P. R. Norton (Eds.) *Infrared Technology and Applications XXXIII*, vol. 6542, (p. 65420B). International Society for Optics and Photonics, SPIE. <https://doi.org/10.1117/12.723849>.
- Belenky, G., Kipshidze, G., Donetsky, D., Svensson, S. P., Sarney, W. L., Hier, H., Shteren-gas, L., Wang, D., & Lin, Y. (2011). Effects of carrier concentration and phonon energy on carrier lifetime in type-2 SLS and properties of InAs_{1-X}Sb_X alloys. In B. F. Andresen, G. F. Fulop, & P. R. Norton (Eds.) *Infrared Technology and Applications XXXVII*, vol. 8012, (p. 80120W). International Society for Optics and Photonics, SPIE. <https://doi.org/10.1117/12.883625>.
- Belenky, G., Suchalkin, S., Svensson, S. P., Donetsky, D., Ermolaev, M., & Kipshidze, G. (2020). Perspective on advances in InAsSb type II superlattices grown on virtual substrates. *Applied Physics Letters*, *117*(25), 250501.
- Beletic, J. W., Blank, R., Gulbransen, D., Lee, D., Loose, M., Piquette, E. C., Sprafke, T., Tennant, W. E., Zandian, M., & Zino, J. (2008). Teledyne Imaging Sensors: infrared imaging technologies for astronomy and civil space. In D. A. Dorn, & A. D. Holland (Eds.) *High Energy, Optical, and Infrared Detectors for Astronomy III*, vol. 7021, (p. 70210H). International Society for Optics and Photonics, SPIE. <https://doi.org/10.1117/12.790382>.
- Bellotti, E., Bertazzi, F., Tibaldi, A., Schuster, J., Bajaj, J., & Reed, M. (2021). Disorder-induced degradation of vertical carrier transport in strain-balanced antimony-based superlattices. *Physical Review Applied*, *16*, 054028.

- Bertazzi, F., Tibaldi, A., Goano, M., Montoya, J. A. G., & Bellotti, E. (2020). Nonequilibrium green's function modeling of type-ii superlattice detectors and its connection to semiclassical approaches. *Physical Review Applied*, *14*, 014083.
- Bianconi, S., & Mohseni, H. (2020). Recent advances in infrared imagers: toward thermodynamic and quantum limits of photon sensitivity. *Reports on Progress in Physics*, *83*(4), 044101.
- Bishop, G., Plis, E., Rodriguez, J. B., Sharma, Y. D., Kim, H. S., Dawson, L. R., & Krishna, S. (2008). nBn detectors based on InAs/GaSb type-II strain layer superlattice. *Journal of Vacuum Science & Technology B*, *26*(3), 1145–1148.
- Cambri, D. (2017). *Modeling the electronic structure of type-II superlattice photodetector*. Master's thesis, Politecnico di Torino.
- Canedy, C., Aifer, E., Warner, J., Vurgaftman, I., Jackson, E., Tischler, J., Powell, S., Olver, K., Meyer, J., & Tennant, W. (2009). Controlling dark current in type-ii superlattice photodiodes. *Infrared Physics & Technology*, *52*(6), 326–334. Proceedings of the International Conference on Quantum Structure Infrared Photodetectors (QSIP) 2009.
- Casias, L. K., Morath, C. P., Steenbergen, E. H., Umana-Membreno, G. A., Webster, P. T., Logan, J. V., Kim, J. K., Balakrishnan, G., Faraone, L., & Krishna, S. (2020). Vertical carrier transport in strain-balanced inas/inassb type-ii superlattice material. *Applied Physics Letters*, *116*(18), 182109.
- Chen, J., Wang, J., Li, X., Chen, J., Yu, F., He, J., Wang, J., Zhao, Z., Li, G., Chen, X., & Lu, W. (2022). Recent progress in improving the performance of infrared photodetectors via optical field manipulations. *Sensors*, *22*(2).
- Chevallier, R., Haddadi, A., & Razeghi, M. (2017). Toward realization of small-size dual-band long-wavelength infrared photodetectors based on inas/gasb/alsb type-ii superlattices. *Solid State Electronics*, *136*, 51–54. Selected Papers from ISDRS 2016.
- Choi, K., Sun, J., & Olver, K. (2015). Resonator-qwip fpa development. In *Infrared Technology and Applications XLI*, vol. 9451, (pp. 687–698). SPIE.
- Chuang, S. L. (2012). *Physics of photonic devices*. John Wiley & Sons.
- Compagnone, F., Manenti, M., Di Carlo, A., & Lugli, P. (2002). Hot electrons and hot phonons in quantum cascade lasers. *Physica B: Condensed Matter*, *314*(1-4), 336–340.
- de Falco, C., Gatti, E., Lacaita, A. L., & Sacco, R. (2005). Quantum-corrected drift-diffusion models for transport in semiconductor devices. *Journal of Computational Physics*, *204*(2), 533–561.

- Delaunay, P.-Y., Nguyen, B. M., Hoffman, D., Huang, E. K.-W., & Razeghi, M. (2009). Background limited performance of long wavelength infrared focal plane arrays fabricated from m-structure inasgasb superlattices. *IEEE Journal of Quantum Electronics*, *45*(2), 157–162.
- Delmas, M., Rossignol, R., Rodriguez, J., & Christol, P. (2017). Design of inas/gasb superlattice infrared barrier detectors. *Superlattices and Microstructures*, *104*, 402–414.
- Donetsky, D., Belenky, G., Svensson, S., & Suchalkin, S. (2010). Minority carrier lifetime in type-2 inasgasb strained-layer superlattices and bulk hgcdte materials. *Applied Physics Letters*, *97*(5), 052108.
- Du, Y.-N., Xu, Y., & Song, G.-F. (2020). Theoretical analysis on the energy band properties of n- and m-structure type-ii superlattices. *Superlattices and Microstructures*, *145*, 106590.
- Esseni, D., & Driussi, F. (2011). A quantitative error analysis of the mobility extraction according to the matthiessen rule in advanced mos transistors. *IEEE Transactions on Electron Devices*, *58*(8), 2415–2422.
- Filоче, M., Piccardo, M., Wu, Y.-R., Li, C.-K., Weisbuch, C., & Mayboroda, S. (2017). Localization landscape theory of disorder in semiconductors. i. theory and modeling. *Physical Review B*, *95*, 144204.
- Foreman, B. A. (1997). Elimination of spurious solutions from eight-band $\mathbf{k} \cdot \mathbf{p}$ theory. *Physical Review B*, *56*, R12748–R12751.
- Frey, M., Esposito, A., & Schenk, A. (2011). Computational comparison of conductivity and mobility models for silicon nanowire devices. *Journal of Applied Physics*, *109*(8), 083707.
- Glennon, J., & Bellotti, E. (2023). Quantum transport simulation of a mid-wave infrared Ga-based type-II superlattice for curved focal-plane arrays. In P. Wijewarnasuriya, A. I. D'Souza, & A. K. Sood (Eds.) *Infrared Sensors, Devices, and Applications XIII*, vol. 12687, (p. 126870F). International Society for Optics and Photonics, SPIE. <https://doi.org/10.1117/12.2682192>.
- Glennon, J., Bertazzi, F., Tibaldi, A., & Bellotti, E. (2023). Extraction of mobility from quantum transport calculations of type-ii superlattices. *Physical Review Applied*, *19*, 044045.
- Glennon, J., Kyrtos, A., O'Masta, M. R., Nguyen, B.-M., & Bellotti, E. (2024). A machine-learning-accelerated quantum transport study on the effects of superlattice disorder and strain in a mid-wave infrared curved sensor. Under review at *Physical Review Applied*.

- Gnani, E., Gnudi, A., Reggiani, S., & Baccarani, G. (2010). Effective mobility in nanowire fetts under quasi-ballistic conditions. *IEEE Transactions on Electron Devices*, 57(1), 336–344.
- Grein, C. H., Young, P. M., Ehrenreich, H., & McGill, T. C. (1993). Auger lifetimes in ideal ingasb/inas superlattices. *Journal of Electronic Materials*, 22(8), 1093–1096.
- Gu, J. J., Wu, H., Liu, Y., Neal, A. T., Gordon, R. G., & Ye, P. D. (2012). Size-dependent-transport study of In_{0.53}Ga_{0.47}As gate-all-around nanowire mosfets: Impact of quantum confinement and volume inversion. *IEEE Electron Device Letters*, 33(7), 967–969.
- Guarnay, S., Triozon, F., Martinie, S., Niquet, Y.-M., & Bournel, A. (2014). Monte carlo study of effective mobility in short channel fdsoi mosfets. In *2014 International Conference on Simulation of Semiconductor Processes and Devices (SISPAD)*, (pp. 105–108).
- Guenter, B., Joshi, N., Stoakley, R., Keefe, A., Geary, K., Freeman, R., Hundley, J., Patterson, P., Hammon, D., Herrera, G., Sherman, E., Nowak, A., Schubert, R., Brewer, P., Yang, L., Mott, R., & McKnight, G. (2017). Highly curved image sensors: a practical approach for improved optical performance. *Optics Express*, 25(12), 13010–13023.
- Gui, Y., Li, B., Zheng, G., Chang, Y., Wang, S., He, L., & Chu, J. (1998). Evaluation of densities and mobilities for heavy and light holes in p-type Hg_{1-x}Cd_xTe molecular beam epitaxy films from magnetic-field-dependent Hall data. *Journal of Applied Physics*, 84(8), 4327–4331.
- Gunapala, S., Rafol, S., Ting, D., Soibel, A., Khoshakhlagh, A., Keo, S., Pepper, B., Fisher, A., Luong, E., Hill, C., Choi, K.-K., D'Souza, A., Masterjohn, C., Babu, S., & Ghuman, P. (2019). Infrared digital focal plane arrays for earth remote sensing applications. In *2019 IEEE Photonics Conference (IPC)*, (pp. 1–2).
- Haddadi, A., Chen, G., Chevallier, R., Hoang, A. M., & Razeghi, M. (2014). Inas/inas_{1-x}s_x type-ii superlattices for high performance long wavelength infrared detection. *Applied Physics Letters*, 105(12), 121104.
- Haran, T. L., James, J. C., Lane, S. E., & Cincotta, T. E. (2019). Quantum efficiency and spatial noise tradeoffs for iiii focal plane arrays. *Infrared Physics & Technology*, 97, 309–318.
- Hess, K. (2012). *Monte Carlo device simulation: full band and beyond*, vol. 144. Springer Science & Business Media.
- Höglund, L., Ting, D. Z., Khoshakhlagh, A., Soibel, A., Hill, C. J., Fisher, A., Keo, S., & Gunapala, S. D. (2013). Influence of radiative and non-radiative recombination on the minority carrier lifetime in midwave infrared InAs/InAsSb superlattices. *APL*, 103(22), 221908.

- Höglund, L., Ting, D. Z., Soibel, A., Fisher, A., Khoshakhlagh, A., Hill, C. J., Baker, L., Keo, S., Mumolo, J., & Gunapala, S. D. (2015). Influence of carrier concentration on the minority carrier lifetime in mid-wavelength infrared InAs/InAsSb superlattices. *Infrared Physics & Technology*, *70*, 62–65. Proceedings of International Conference on Quantum Structures Infrared Photodetectors, 2014.
- Hostut, M., Alyoruk, M., Tansel, T., Kilic, A., Turan, R., Aydinli, A., & Ergun, Y. (2015). N-structure based on inas/alsb/gasb superlattice photodetectors. *Superlattices and Microstructures*, *79*, 116–122.
- Hostut, M., & Ergun, Y. (2021). Quantum efficiency contributions for type-ii inas/gasb sl photodetectors. *Physica E: Low-dimensional Systems and Nanostructures*, *130*, 114721.
- Huet, K., Querlioz, D., Chaisantikulwat, W., Saint-Martin, J., Bournel, A., Mouis, M., & Dollfus, P. (2008). Monte carlo study of apparent magnetoresistance mobility in nanometer scale metal oxide semiconductor field effect transistors. *Journal of Applied Physics*, *104*(4), 044504.
- Huet, K., Saint-Martin, J., Bournel, A., Galdin-Retailleau, S., Dollfus, P., Ghibaudo, G., & Mouis, M. (2007). Monte carlo study of apparent mobility reduction in nano-mosfets. In *ESSDERC 2007 - 37th European Solid State Device Research Conference*, (pp. 382–385).
- Khoshakhlagh, A., Myers, S., Kim, H., Plis, E., Gautam, N., Lee, S. J., Noh, S. K., Dawson, L. R., & Krishna, S. (2010). Long-wave inas/gasb superlattice detectors based on nbn and pin designs. *IEEE Journal of Quantum Electronics*, *46*(6), 959–964.
- Kim, H., Meng, Y., Klem, J. F., Hawkins, S. D., Kim, J. K., & Zuo, J.-M. (2018). Sb-induced strain fluctuations in a strained layer superlattice of inas/inassb. *Journal of Applied Physics*, *123*(16), 161521.
- Kinch, M. A. (2007). *Fundamentals of infrared detector materials*, vol. 76. SPIE press.
- Klipstein, P. C. (2022). Perspective on iiv barrier detectors. *Applied Physics Letters*, *120*(6), 060502.
- Klipstein, P. C., Livneh, Y., Glozman, A., Grossman, S., Klin, O., Snapi, N., & Weiss, E. (2014). Modeling inas/gasb and inas/inassb superlattice infrared detectors. *Journal of Electronic Materials*, *43*(8), 2984–2990.
- Kopytko, M., & Rogalski, A. (2022). Performance evaluation of type-ii superlattice devices relative to hgcdte photodiodes. *IEEE Transactions on Electron Devices*, *69*(6), 2992–3002.

- Kyrtos, A., Glennon, J., Glasmann, A., O'Masta, M. R., Nguyen, B.-M., & Bellotti, E. (2021). Machine-learning-assisted first-principles calculations of strained $\text{InAs}_{1-x}\text{Sb}_x$ alloys for curved focal-plane arrays. *Physical Review Applied*, *15*, 064008.
- Lackner, D. (2011). *InAsSb/InAs Strain Balanced Superlattices for Photodetector Applications*. Ph.D. thesis, Simon Fraser University, British Columbia.
- Laikhtman, B., & Miller, D. (1993). Theory of current-voltage instabilities in superlattices. *Physical Review B*, *48*, 5395–5412.
- Lake, R. K., & Pandey, R. R. (2006). Non-equilibrium green functions in electronic device modeling. *arXiv preprint cond-mat/0607219*.
- Lang, X.-L., & Xia, J.-B. (2013). Electronic structure and optical properties of InAs/GaSb superlattice. *Journal of Applied Physics*, *113*(4), 043715.
- Li, S. S. (1976). Investigation of electronic transport, recombination and optical properties in $\text{InAs}_{1-x}\text{P}_x$ alloy systems. Final Report, Dec. 1973 - Apr. 1976 Florida Univ., Gainesville. Engineering and Industrial Experiment Station.
- Li, X., Zhang, Y., Jiang, D., Guo, F., Wang, D., & Zhao, L. (2017). Atomic intermixing and segregation at the interface of InAs/GaSb type ii superlattices. *Superlattices and Microstructures*, *104*, 390–396.
- Li, Y., Xiao, W., Wu, L., Xie, X., Lu, P., & Wang, S. (2019). Dark current characteristic of p-i-n and nbn mwir InAs/GaSb superlattice infrared detectors. In *2019 IEEE 4th Optoelectronics Global Conference (OGC)*, (pp. 70–75).
- Lin, J., Wu, Y., del Alamo, J. A., & Antoniadis, D. A. (2016). Analysis of resistance and mobility in InGaAs quantum-well mosfets from ballistic to diffusive regimes. *IEEE Transactions on Electron Devices*, *63*(4), 1464–1470.
- Liu, G., & Chuang, S.-L. (2002). Modeling of Sb -based type-ii quantum cascade lasers. *Physical Review B*, *65*(16), 165220.
- Liu, J., Donetski, D., Kucharczyk, K., Zhao, J., Kipshidze, G., Belenky, G., & Svensson, S. P. (2022). Short-period InAsSb -based strained layer superlattices for high quantum efficiency long-wave infrared detectors. *Applied Physics Letters*, *120*(14), 141101.
- Liu, L., Saripalli, V., Narayanan, V., & Datta, S. (2011). Experimental investigation of scalability and transport in $\text{In}_{0.7}\text{Ga}_{0.3}\text{As}$ multi-gate quantum well fet (μqfet). In *69th Device Research Conference*, (pp. 17–18).
- Livneh, Y., Klipstein, P. C., Klin, O., Snapi, N., Grossman, S., Glozman, A., & Weiss, E. (2012). $\mathbf{k} \cdot \mathbf{p}$ model for the energy dispersions and absorption spectra of InAs/GaSb type-ii superlattices. *Physical Review B*, *86*, 235311.

- Livneh, Y., Klipstein, P. C., Klin, O., Snapi, N., Grossman, S., Glozman, A., & Weiss, E. (2014). Erratum: $k \cdot p$ model for the energy dispersions and absorption spectra of InAs/GaSb type-II superlattices [phys. rev. b 86, 235311 (2012)]. *Physical Review B*, *90*, 039903.
- Luisier, M. (2011). Phonon-limited and effective low-field mobility in n- and p-type [100]-, [110]-, and [111]-oriented Si nanowire transistors. *Applied Physics Letters*, *98*(3), 032111.
- Lundstrom, M., & Jeong, C. (2013). *Near-Equilibrium Transport*. WORLD SCIENTIFIC.
- Lundstrom, M., & Sun, X. (2016). Some useful relations for analyzing nanoscale mosfets operating in the linear region. <https://arxiv.org/abs/1603.03132>.
- Łusakowski, J., Knap, W., Meziani, Y., Cesso, J. P., El Fatimy, A., Tauk, R., Dyakonova, N., Ghibaudo, G., Boeuf, F., & Skotnicki, T. (2005). Influence of ballistic and pocket effects on electron mobility in Si mosfets. In *Proceedings of 35th European Solid-State Device Research Conference, 2005. ESSDERC 2005.*, (pp. 561–564).
- Łusakowski, J., Martínez, M. J. M., Rengel, R., González, T., Tauk, R., Meziani, Y. M., Knap, W., Boeuf, F., & Skotnicki, T. (2007). Quasiballistic transport in nanometer Si metal-oxide-semiconductor field-effect transistors: Experimental and Monte Carlo analysis. *JAP*, *101*(11), 114511.
- Maimon, S., & Wicks, G. W. (2006). nBn detector, an infrared detector with reduced dark current and higher operating temperature. *Applied Physics Letters*, *89*(15), 151109.
- Majumdar, A., & Antoniadis, D. A. (2014). Analysis of carrier transport in short-channel mosfets. *IEEE Transactions on Electron Devices*, *61*(2), 351–358.
- Manyk, T., Michalczewski, K., Murawski, K., Martyniuk, P., & Rutkowski, J. (2019). InAs/InAsB strain-balanced superlattices for longwave infrared detectors. *Sensors*, *19*(8).
- Marozas, B. T., Hughes, W. D., Du, X., Sidor, D. E., Savich, G. R., & Wicks, G. W. (2018). Surface dark current mechanisms in III-V infrared photodetectors. *Optical Materials Express*, *8*(6), 1419–1424.
- Martyniuk, P., Kopytko, M., & Rogalski, A. (2014). Barrier infrared detectors. *Opto-Electronics Review*, *22*(2), 127–146.
- Martyniuk, P., Wrobel, J., Plis, E., Madejczyk, P., Gawron, W., Kowalewski, A., Krishna, S., & Rogalski, A. (2013). Modeling of midwavelength infrared InAs/GaSb type II superlattice detectors. *Optical Engineering*, *52*(6), 061307.
- Matthews, J., & Blakeslee, A. (1974). Defects in epitaxial multilayers: I. misfit dislocations. *Journal of Crystal Growth*, *27*, 118–125.

- Meyer, J. R., Hoffman, C. A., Bartoli, F. J., & RamMohan, L. R. (1995). Typeii quantumwell lasers for the midwavelength infrared. *Applied Physics Letters*, 67(6), 757–759.
- Montoya, J. A. G. (2023). *Full-band NEGF modeling of optoelectronic devices*. Ph.D. thesis, Politecnico di Torino.
- Muraki, K., Fukatsu, S., Shiraki, Y., & Ito, R. (1992). Surface segregation of in atoms during molecular beam epitaxy and its influence on the energy levels in ingosbournas/gaas quantum wells. *Applied Physics Letters*, 61(5), 557–559.
- Nakwaski, W. (1995). Effective masses of electrons and heavy holes in gaas, inas, alas and their ternary compounds. *Physica B*, 210(1), 1–25.
- Nguyen, B.-M. (2010). *Theoretical Design and Material Growth of Type-II Antimonide-based Superlattices for Infrared Detection and Imaging*. Ph.D. thesis, Northwestern University.
- Nguyen, B.-M., Bogdanov, S., Pour, S. A., & Razeghi, M. (2009). Minority electron unipolar photodetectors based on type ii inas/gasb/alsb superlattices for very long wavelength infrared detection. *Applied Physics Letters*, 95(18), 183502.
- Nguyen, B.-M., Hoffman, D., Delaunay, P.-Y., Huang, E. K.-W., Razeghi, M., & Pellegrino, J. (2008). Band edge tunability of m-structure for heterojunction design in sb based type ii superlattice photodiodes. *Applied Physics Letters*, 93(16), 163502.
- Nguyen, B.-M., Hoffman, D., Delaunay, P.-Y., & Razeghi, M. (2007a). Dark current suppression in type ii inas/gasb superlattice long wavelength infrared photodiodes with m-structure barrier. *Applied Physics Letters*, 91(16), 163511.
- Nguyen, B.-M., Hoffman, D., Wei, Y., Delaunay, P.-Y., Hood, A., & Razeghi, M. (2007b). Very high quantum efficiency in type-ii inas/gasb superlattice photodiode with cutoff of 12m. *Applied Physics Letters*, 90(23), 231108.
- Nguyen, B.-M., Razeghi, M., Nathan, V., & Brown, G. J. (2007c). Type-II M structure photodiodes: an alternative material design for mid-wave to long wavelength infrared regimes. In M. Razeghi, & G. J. Brown (Eds.) *Quantum Sensing and Nanophotonic Devices IV*, vol. 6479, (p. 64790S). International Society for Optics and Photonics, SPIE. <https://doi.org/10.1117/12.711588>.
- Nguyen, V.-H., Niquet, Y.-M., Triozon, F., Duchemin, I., Nier, O., & Rideau, D. (2014). Quantum modeling of the carrier mobility in fdsoi devices. *IEEE Transactions on Electron Devices*, 61(9), 3096–3102.
- Nguyen, V.-H., Triozon, F., Bonnet, F. D. R., & Niquet, Y.-M. (2013). Performances of strained nanowire devices: Ballistic versus scattering-limited currents. *IEEE Transactions on Electron Devices*, 60(5), 1506–1513.

- Niquet, Y.-M., Nguyen, V.-H., Triozon, F., Duchemin, I., Nier, O., & Rideau, D. (2014). Quantum calculations of the carrier mobility: Methodology, matthiessen's rule, and comparison with semi-classical approaches. *Journal of Applied Physics*, *115*(5), 054512.
- Olson, B. V., Kim, J. K., Kadlec, E. A., Klem, J. F., Hawkins, S. D., Coon, W. T., Fortune, T. R., Tauke-Pedretti, A., Cavaliere, M. A., & Shaner, E. A. (2016). Optical and electrical properties of narrow-bandgap infrared w-structure superlattices incorporating alas/alsb/ alas barrier layers. *Applied Physics Letters*, *108*(25), 252104.
- Olson, B. V., Klem, J. F., Kadlec, E. A., Kim, J. K., Goldflam, M. D., Hawkins, S. D., Tauke-Pedretti, A., Coon, W. T., Fortune, T. R., Shaner, E. A., & Flatté, M. E. (2017). Vertical hole transport and carrier localization in InAs/inas_{1-x}sb_x type-ii superlattice heterojunction bipolar transistors. *Physical Review Applied*, *7*, 024016.
- Olson, B. V., Murray, L. M., Prineas, J. P., Flatté, M. E., Olesberg, J. T., & Boggess, T. F. (2013). All-optical measurement of vertical charge carrier transport in mid-wave infrared inas/gasb type-ii superlattices. *Applied Physics Letters*, *102*(20), 202101.
- Olson, B. V., Shaner, E. A., Kim, J. K., Klem, J. F., Hawkins, S. D., Murray, L. M., Prineas, J. P., Flatté, M. E., & Boggess, T. F. (2012). Time-resolved optical measurements of minority carrier recombination in a mid-wave infrared InAsSb alloy and InAs/InAsSb superlattice. *Applied Physics Letters*, *101*(9), 092109.
- O'Masta, M. R., Nguyen, B.-M., Gurga, A., Sasse, T., Hempe, B., Neuhaus, C., Clough, E. C., Hundley, J., Patterson, P. R., Jenkins, J., Chen, M., Jacques, G., Linton, S., Perez, F., Ysseldyk, C. V., Wang, E., Tang, Y., Niwa, K., Schaedler, T., Kyrtos, A., Glennon, J., Glasmann, A., Bellotti, E., & McKnight, G. (2022). Curving of large-format infrared sensors. In B. F. Andresen, G. F. Fulop, & L. Zheng (Eds.) *Infrared Technology and Applications XLVIII*, vol. 12107, (p. 121071S). International Society for Optics and Photonics, SPIE. <https://doi.org/10.1117/12.2618122>.
- OpenAI (2023). Chatbot interaction through generative pre-trained transformer 4. Software accessible at <https://chat.openai.com>.
- Osborn, G. C. (1984). Inassb strainedlayer superlattices for long wavelength detector applications. *Journal of Vacuum Science & Technology B*, *2*(2), 176–178.
- Pala, M. G., Buran, C., Poli, S., & Mouis, M. (2009). Full quantum treatment of surface roughness effects in silicon nanowire and double gate fets. *Journal of Computational Electronics*, *8*(3), 374.
- Pedregosa, F., Varoquaux, G., Gramfort, A., Michel, V., Thirion, B., Grisel, O., Blondel, M., Prettenhofer, P., Weiss, R., Dubourg, V., Vanderplas, J., Passos, A., Cournapeau, D., Brucher, M., Perrot, M., & Duchesnay, E. (2011). Scikit-learn: Machine learning in Python. <http://www.jmlr.org/papers/volume12/pedregosa11a/pedregosa11a.pdf>.

- Piprek, J. (2017). *Handbook of Optoelectronic Device Modeling and Simulation: Fundamentals, Materials, Nanostructures, LEDs, and Amplifiers, Vol. 1*. CRC Press.
- Poli, S., & Pala, M. G. (2009). Channel-length dependence of low-field mobility in silicon-nanowire fets. *IEEE Electron Device Letters*, 30(11), 1212–1214.
- Poli, S., Pala, M. G., & Poiroux, T. (2009). Full quantum treatment of remote coulomb scattering in silicon nanowire fets. *IEEE Transactions on Electron Devices*, 56(6), 1191–1198.
- Polizzi, E., & Datta, S. (2003). Multidimensional nanoscale device modeling: the finite element method applied to the non-equilibrium green's function formalism. In *2003 Third IEEE Conference on Nanotechnology, 2003. IEEE-NANO 2003.*, vol. 1, (pp. 40–43). IEEE.
- Qiao, P.-F., Mou, S., & Chuang, S. L. (2012). Electronic band structures and optical properties of type-ii superlattice photodetectors with interfacial effect. *Optics Express*, 20(3), 2319–2334.
- Razeghi, M., & Nguyen, B.-M. (2014). Advances in mid-infrared detection and imaging: a key issues review. *Reports on Progress in Physics*, 77(8), 082401.
- Rehm, R., Masur, M., Schmitz, J., Daumer, V., Niemasz, J., Vandervelde, T., DeMeo, D., Luppold, W., Wauro, M., Wörl, A., Rutz, F., Scheibner, R., Ziegler, J., & Walther, M. (2013). Inas/gasb superlattice infrared detectors. *Infrared Physics & Technology*, 59, 6–11. Proceedings of the International Conference on Quantum Structure Infrared Photodetector (QSIP) 2012.
- Rehm, R., Walther, M., Schmitz, J., Rutz, F., FleiSSner, J., Scheibner, R., & Ziegler, J. (2009). Inas/gasb superlattices for advanced infrared focal plane arrays. *Infrared Physics & Technology*, 52(6), 344–347. Proceedings of the International Conference on Quantum Structure Infrared Photodetectors (QSIP) 2009.
- Rhyner, R., & Luisier, M. (2013). Phonon-limited low-field mobility in silicon: Quantum transport vs. linearized boltzmann transport equation. *Journal of Applied Physics*, 114(22), 223708.
- Rim, S.-B., Catrysse, P. B., Dinyari, R., Huang, K., & Peumans, P. (2008). The optical advantages of curved focal plane arrays. *Optics Express*, 16(7), 4965–4971.
- Riyadi, M. A., & Arora, V. K. (2011). The channel mobility degradation in a nanoscale metaloxidesemiconductor field effect transistor due to injection from the ballistic contacts. *Journal of Applied Physics*, 109(5), 056103.

- Rode, D. (1975). Chapter 1 low-field electron transport. vol. 10 of *Semiconductors and Semimetals*, (pp. 1–89). Elsevier. <https://www.sciencedirect.com/science/article/pii/S0080878408603312>.
- Rogalski, A. (2003). Infrared detectors: status and trends. *Progress in Quantum Electronics*, 27(2), 59–210.
- Rogalski, A. (2011). Recent progress in infrared detector technologies. *Infrared Physics & Technology*, 54(3), 136–154. Proceedings of the International Conference on Quantum Structure Infrared Photodetector (QSIP) 2010.
- Rogalski, A., Kopytko, M., Hu, W., & Martyniuk, P. (2023). Infrared hot photodetectors: Status and outlook. *Sensors*, 23(17).
- Rogalski, A., Martyniuk, P., & Kopytko, M. (2016). Challenges of small-pixel infrared detectors: a review. *Reports on Progress in Physics*, 79(4), 046501.
- Rogalski, A., Martyniuk, P., & Kopytko, M. (2017). Inas/gasb type-ii superlattice infrared detectors: Future prospect. *Applied Physics Review*, 4(3), 031304.
- Rogalski, A., Martyniuk, P., & Kopytko, M. (2019). Type-ii superlattice photodetectors versus hgcdte photodiodes. *Progress in Quantum Electronics*, 68, 100228.
- Salihoglu, O., Muti, A., Kutluer, K., Tansel, T., Turan, R., Ergun, Y., & Aydinli, A. (2012). n structure for type-ii superlattice photodetectors. *Applied Physics Letters*, 101(7), 073505.
- Salihoglu, O., Muti, A., Turan, R., Ergun, Y., & Aydinli, A. (2014). Low dark current N structure superlattice MWIR photodetectors. In B. F. Andresen, G. F. Fulop, C. M. Hanson, & P. R. Norton (Eds.) *Infrared Technology and Applications XL*, vol. 9070, (p. 907012). International Society for Optics and Photonics, SPIE. <https://doi.org/10.1117/12.2050316>.
- Shur, M. (2002). Low ballistic mobility in submicron hemts. *IEEE Electron Device Letters*, 23(9), 511–513.
- Sidor, D. E. (2017). *Surface Conduction in III-V Semiconductor Infrared Detector Materials*. Ph.D. thesis, University of Rochester, New York.
- Singh, A., Mukherjee, S., & Muralidharan, B. (2022). Comprehensive quantum transport analysis of m-superlattice structures for barrier infrared detectors. *Journal of Applied Physics*, 131(9), 094303.
- Smith, C., Abram, R., & Burt, M. (1985). Theory of auger recombination in a quantum well heterostructure. *Superlattices and Microstructures*, 1(2), 119–123.

- Smith, D. L., & Mailhiot, C. (1987). Proposal for strained type ii superlattice infrared detectors. *Journal of Applied Physics*, *62*(6), 2545–2548.
- Smith, M. (2009). *ABAQUS/Standard User's Manual, Version 6.9*. United States.
- Soibel, A., Ting, D. Z., Fisher, A. M., Khoshakhlagh, A., Pepper, B., & Gunapala, S. D. (2020). Temperature dependence of diffusion length and mobility in mid-wavelength InAs/InAsSb superlattice infrared detectors. *Applied Physics Letters*, *117*(23), 231103.
- Steenbergen, E. H., Connelly, B. C., Metcalfe, G. D., Shen, H., Wraback, M., Lubyshev, D., Qiu, Y., Fastenau, J. M., Liu, A. W. K., Elhamri, S., Cellek, O. O., & Zhang, Y.-H. (2011). Significantly improved minority carrier lifetime observed in a long-wavelength infrared iii-v type-ii superlattice comprised of inas/inassb. *Applied Physics Letters*, *99*(25), 251110.
- Stefanucci, G., & Van Leeuwen, R. (2013). *Nonequilibrium many-body theory of quantum systems: a modern introduction*. Cambridge University Press.
- Steiger, S. (2009). *Modelling Nano-LEDs*. Ph.D. thesis, Eidgenössische Technische Hochschule Zürich.
- Swartz, C. H., & Myers, T. H. (2014). Method for the simultaneous determination of vertical and horizontal mobilities in superlattices. *Physical Review B*, *89*, 075305.
- Taghipour, Z., Kazemi, A., Myers, S., Wijewarnasuriya, P., Mathews, S., Steenbergen, E. H., Morath, C., Cowan, V. M., Ariyawansa, G., Scheihing, J., & Krishna, S. (2017). Extraction of minority carrier diffusion length of MWIR Type-II superlattice nBp detector. In P. D. LeVan, A. K. Sood, P. Wijewarnasuriya, & A. I. D'Souza (Eds.) *Infrared Sensors, Devices, and Applications VII*, vol. 10404, (p. 1040406). International Society for Optics and Photonics, SPIE. <https://doi.org/10.1117/12.2274591>.
- Tan, B., Cheng, S., Liu, B., Zhou, W., Liu, Y., Zhang, C., Cao, S., Ding, Y., Yang, Z., & Huang, L. (2021). Effective suppression of surface leakage currents in t2sl photodetectors with deep and vertical mesa sidewalls via tma and h2 plasma combined pretreatment. *Infrared Physics & Technology*, *116*, 103724.
- Tibaldi, A., Bertazzi, F., Goano, M., Michalzik, R., & Debernardi, P. (2019). Venus: A vertical-cavity surface-emitting laser electro-opto-thermal numerical simulator. *IEEE Journal of Selective Topics in Quantum Electronics*, *25*(6), 1–12.
- Tibaldi, A., Gonzalez Montoya, J. A., Vallone, M., Goano, M., Bellotti, E., & Bertazzi, F. (2021). Modeling infrared superlattice photodetectors: From nonequilibrium green's functions to quantum-corrected drift diffusion. *Physical Review Applied*, *16*, 044024.

- Ting, D. Z., Fisher, A. M., Pepper, B. J., Hill, C. J., Keo, S. A., Khoshakhlagh, A., Soibel, A., Rafol, S. B., Maruyama, Y., Gunapala, S. D., & Pagano, T. S. (2022a). Progress in InAs/InAsSb superlattice barrier infrared detectors. In B. F. Andresen, G. F. Fulop, & L. Zheng (Eds.) *Infrared Technology and Applications XLVIII*, vol. 12107, (p. 1210700). International Society for Optics and Photonics, SPIE. <https://doi.org/10.1117/12.2618867>.
- Ting, D. Z., Fisher, A. M., Pepper, B. J., Hill, C. J., Keo, S. A., Khoshakhlagh, A., Soibel, A., Rafol, S. B., Maruyama, Y., Gunapala, S. D., & Pagano, T. S. (2022b). Progress in InAs/InAsSb superlattice barrier infrared detectors. In B. F. Andresen, G. F. Fulop, & L. Zheng (Eds.) *Infrared Technology and Applications XLVIII*, vol. 12107, (p. 1210700). International Society for Optics and Photonics, SPIE. <https://doi.org/10.1117/12.2618867>.
- Ting, D. Z., Rafol, S. B., Khoshakhlagh, A., Soibel, A., Keo, S. A., Fisher, A. M., Pepper, B. J., Hill, C. J., & Gunapala, S. D. (2020). Inas/inassb type-ii strained-layer superlattice infrared photodetectors. *Micromachines*, *11*(11).
- Ting, D. Z., Soibel, A., & Gunapala, S. D. (2016). Hole effective masses and subband splitting in type-ii superlattice infrared detectors. *Applied Physics Letters*, *108*(18), 183504.
- Ting, D. Z., Soibel, A., & Gunapala, S. D. (2017). Type-ii superlattice hole effective masses. *Infrared Physics & Technology*, *84*, 102–106. Quantum Structure Infrared Photodetector 2016 (QSIP2016).
- Ting, D. Z.-Y., Hill, C. J., Soibel, A., Keo, S. A., Mumolo, J. M., Nguyen, J., & Gunapala, S. D. (2009). A high-performance long wavelength superlattice complementary barrier infrared detector. *Applied Physics Letters*, *95*(2), 023508.
- Tsai, T.-Y., Michalczewski, K., Martyniuk, P., Wu, C.-H., & Wu, Y.-R. (2020). Application of localization landscape theory and the k_{up} model for direct modeling of carrier transport in a type ii superlattice inas/inassb photoconductor system. *Journal of Applied Physics*, *127*(3), 033104.
- Tsu, R., & Esaki, L. (1991). Stark quantization in superlattices. *Physical Review B*, *43*, 5204–5206.
- Umana-Membreno, G. A., Klein, B., Kala, H., Antoszewski, J., Gautam, N., Kutty, M. N., Plis, E., Krishna, S., & Faraone, L. (2012). Vertical minority carrier electron transport in p-type inas/gasb type-ii superlattices. *Applied Physics Letters*, *101*(25), 253515.
- Veprek, R. G. (2009). *Computational modeling of semiconductor nanostructures for optoelectronics*. Ph.D. thesis, ETH Zurich.

- Veprek, R. G., Steiger, S., & Witzigmann, B. (2007). Ellipticity and the spurious solution problem of $\mathbf{k}\cdot\mathbf{p}$ envelope equations. *Physical Review B*, *76*, 165320.
- Vurgaftman, I., Meyer, J. R., & Ram-Mohan, L. R. (2001). Band parameters for iiiiv compound semiconductors and their alloys. *Journal of Applied Physics*, *89*(11), 5815–5875.
- Wacker, A., & Jauho, A.-P. (1998). Quantum transport: The link between standard approaches in superlattices. *Physical Review Letters*, *80*, 369–372.
- Wang, J., & Lundstrom, M. (2003). Ballistic transport in high electron mobility transistors. *IEEE Transactions on Electron Devices*, *50*(7), 1604–1609.
- Wang, R., Liu, H., Huang, R., Zhuge, J., Zhang, L., Kim, D.-W., Zhang, X., Park, D., & Wang, Y. (2008). Experimental investigations on carrier transport in si nanowire transistors: Ballistic efficiency and apparent mobility. *IEEE Transactions on Electron Devices*, *55*(11), 2960–2967.
- Webster, P. T., Riordan, N. A., Liu, S., Steenbergen, E. H., Synowicki, R. A., Zhang, Y.-H., & Johnson, S. R. (2015). Measurement of InAsSb bandgap energy and InAs/InAsSb band edge positions using spectroscopic ellipsometry and photoluminescence spectroscopy. *Journal of Applied Physics*, *118*(24). 245706.
- Witzigmann, B., Witzig, A., & Fichtner, W. (2000). A multidimensional laser simulator for edge-emitters including quantum carrier capture. *IEEE Transactions on Electron Devices*, *47*(10), 1926–1934.
- Wu, H., Jiang, Y., Li, J., Ma, X., Song, J., Yu, H., Fu, D., Xu, Y., Zhu, H., & Song, G. (2016). Performance analysis of an n-structure type-ii superlattice photodetector for long wavelength infrared applications. *Journal of Alloys and Compounds*, *684*, 663–668.
- Youngdale, E. R., Meyer, J. R., Hoffman, C. A., Bartoli, F. J., Grein, C. H., Young, P. M., Ehrenreich, H., Miles, R. H., & Chow, D. H. (1994). Auger lifetime enhancement in inas-gal-xinxsb superlattices. *Applied Physics Letters*, *64*(23), 3160–3162.
- Zeng, L., He, Y., Povolotskyi, M., Liu, X., Klimeck, G., & Kubis, T. (2013). Low rank approximation method for efficient green's function calculation of dissipative quantum transport. *Journal of Applied Physics*, *113*(21).
- Zhou, X., Bertazzi, F., Goano, M., Ghione, G., & Bellotti, E. (2014). Deriving $\mathbf{k}\cdot\mathbf{p}$ parameters from full-brillouin-zone descriptions: A finite-element envelope function model for quantum-confined wurtzite nanostructures. *Journal of Applied Physics*, *116*(3).
- Zilli, M., Esseni, D., Palestri, P., & Selmi, L. (2007). On the apparent mobility in nanometric n-mosfets. *IEEE Electron Device Letters*, *28*(11), 1036–1039.

CURRICULUM VITAE

